首都大学東京　博士（理学）学位論文（課程博士）

論 文 名　光機能性薄膜の作製と分子センサーへの応用（英文）

著　者　藤田　隆史

審査担当者

主　査

委　員

委　員

委　員

上記の論文を合格と判定する

平成　　年　　月　　日

首都大学東京大学院理工学研究科教授会

研究科長

DISSERTATION FOR A DEGREE OF DOCTOR OF PHILOSOPHY IN SCIENCE TOKYO METROPOLITAN UNIVERSITY

TITLE : Fabrication of optical functional thin film for an application as a molecular sensor

AUTHOR : Takashi Fujita

EXAMINED BY

Examiner in chief

Examiner

Examiner

Examiner

QUALIFIED BY THE GRADUATE SCHOOL
OF SCIENCE AND ENGINEERING
TOKYO METROPOLITAN UNIVERSITY

Dean

Date

学位論文要旨（理学博士）

論文著者名　藤田　隆史

論文題名

Fabrication of optical functional thin film
for an application as a molecular sensor

（邦題）：光機能性薄膜の作製と分子センサーへの応用（英文）

Optical functional thin films can cause various surface effects by their photo excitation. These surface effects are divided into two types. One is surface reaction with adsorbate. The other is unique career movement such as surface plasmon (SP) excitation, charge separation and so on. These effects lead to various applicatons such as photocatalyst, solar cell, optical sensors and so on. Therefore, fabrication of optical functional thin films gives us not only scientific interest but also various practical uses. In this thesis, the author fabricated two optical functional thin films (titania thin film and two dimensional array (2D-array) of gold nanoparticle) for application of optical molecular sensor with surface assisted laser desorption/ionization (SALDI-MS) and surface enhanced Raman scattering (SERS) measurements.

Photocatalytic effect on titania surface causes interesting reaction such as degradation of organic molecules and site-selective redox reaction and so on. However, these reactions are very complex. Therefore, simple observation methods for revealing these reaction products in whole are required. In order to observe these reaction products, the author focused on SALDI-MS because SALDI-MS spectra can reflect surface properties of SALDI-MS ionization substrates according to our previous studies. In this thesis, the author fabricated titania thin film, and then applied the thin film to SALDI-MS substrates for monitoring degradation of organic molecules with oligosaccharides.

SERS is an attractive technique for ultra-trace analysis of analyte due to its huge enhancement effect caused by SP resonance on a metal nanostructured surface. However, it is difficult to control the enhancement effect because the efficiency of SP resonance strongly depends on a surface morphology of the SERS active substrate.

From this reason, conventional SERS measurement has not applied for practical optical molecular sensor due to its low-reproducibility. Therefore, in order to solve this problem, uniform surface morphology of nanostructure is required as a SERS active substrate. To create a uniform surface roughness of a nanostructured surface, the author focused on a highly-ordered 2D-array of metal nanoparticles (2DMA) with a constant inter-particle distance by using same metal nanoparticle because fabricated SERS active substrates are expected to have same enhancement effect at any position of the substrate. Highly-ordered 2DMAs requires elimination of aggregations because aggregations cause not only a random efficiency of SP excitation but also a decrease of enhancement effect. Generally, in order to prevent nanoparticles from aggregating, surface modifier are used because the modifier plays a role as a spacer between nanoparticles. However, the surface modifier changes its optical property and generates background signals which interfere with the detection of target molecules. From these reasons, it is expected that the 2DMA composed by metal nanoparticles without any surface modifier has a large potential for a molecular sensor, but fabrication methods of the 2DMA still have not been proposed.

On the other hand, our group succeeded in fabrication of highly-ordered 2DMA without any surface modifier by using the novel technique, which is called sandwich (SW) method. The SW method is a very simple technique which is only by sandwiching the gold nanoparticle (AuNP) solution between two flat plates and drying naturally. However, the 2DMA at this stage could not work for SERS analysis. The reason was that an area of the 2DMA was too small to obtain many SERS spectra from one substrate and to estimate the quantitative performance. In this thesis, the fabrication condition of the SW-method has been optimized in order to expand the area of the 2DMA and a fabrication mechanism in the SW-method has been studied. Then the 2DMA has been applied to SERS measurement in order to develop a molecular sensor with a high reproducibility and an ultra-high sensitivity.

Chapter 1 deals with general introduction. Importance of optical functional thin films was discussed. Proposed mechanisms of photocatalytic effect and SERS enhancement effect and purpose of this thesis are discussed.

In chapter 2, SALDI-MS measurements of oligosaccharides on the titania substrate, which were prepared by using oil/water interface trapping method, were discussed. A lot of fragment ions of oligosaccharides were observed. They had periodical molecular weight which is correspond to oligosaccharide units only by our substrate. It is suggested that the unique fragmentation process on the titania SALDI-MS substrate relates to photocatalytic reaction.

In chapter 3, fundamentals of localized SP (LSP), calculation of optical properties of AuNPs and inter-particle coupling effect are discussed in order to understand a relationship between LSP excitation and electromagnetic enhancement in SERS. Optimum diameter of AuNP was estimated for the SERS measurement. To be from 60 nm to 100 nm are suitable because they have high efficiencies of SP excitation.

In chapter 4, common fabrication methods of two-dimensional metal nanostructure and the reason why attention was paid to the 2DMA as quantitative SERS active substrates are discussed. And, the theory for interactions between colloids in solution is discussed. As a result, a guideline for fabricating the highly-ordered 2DMA composed by AuNPs without any surface modifier was obtained.

In chapter 5, SW method and characterization of the 2DMA fabricated by SW method using scanning electron microscope are discussed. And, experimental conditions of the SW method were optimized. As a result, the area of the 2DMA composed by AuNPs without any surface modifier was expanded compared with that at early stage of this method. Moreover, the 2DMA had a higher packing rate compared with those fabricated by conventional methods.

In chapter 6, a uniformity of the 2DMA of the SW-method and a mechanism of arrangement in the SW-method are discussed by using SEM analysis with Fourier Transform analysis, Vis absorption spectroscopy and optical microscope. These analyses showed that the 2DMA had a high uniformity and a hexagonal periodicity with inter-particle distance of 4nm in the arrangement. From these results, it is considered that the 2DMA have a high uniformity and a constant inter-particle distance (4.5nm) which has a large potential to generate a giant enhancement effect. Moreover, the assembly mechanism of SW method was investigated by observations of assembly process with an optical microscope. As a result, it was found that the SW method had three important processes; 1. Supplying AuNPs toward the contact line. 2. Maintaining dispersive nature just before formation of the 2DMA. 3. Smooth movement of the contact line toward inside

In chapter 7, SW-substrates were applied as SERS active substrates, and their analytical performances such as sensitivity and reproducibility were evaluated. Raman measurements revealed that SW substrates gave us an enhancement in Raman signals of CV by 5 to 6 orders of magnitude. Therefore, SW substrates had high SERS enhancement effect. Next in order to evaluate a reproducibility of SERS signals detected on the SW substrate, spot-to-spot SERS signals from the SW-substrate were measured. The SW substrate enabled a high reproducible detection of SERS signals. It is considered that the SW-substrate had uniform EM fields.

In conclusion, the author fabricated two optical functional thin films. One is titania thin film. SALDI-MS measurement of oligosaccharides on the titania thin film showed specific fragment pattern which indicates photocatalytic degradation. Second is highly-ordered 2DMA of AuNPs. The 2DMA had a higher uniformity than those of conventional methods and a hexagonal periodicity with an inter-particle distance of 4 nm in the arrangement. And, in SERS measurement, the 2DMA showed a remarkably high spot-to-spot reproducibility and a high sensitivity. Therefore, the 2DMA had a large potential for molecular sensor with high reproducibility and ultra-high sensitivity.

Contents

Chapter 1

General introduction

1-1 Optical functional thin film

Molecular sensor with high analytical performances such as quantitative ability, qualitative ability, label-free analysis, ultra-high sensitivity and so on is one of key technologies to make scientists' dreams come true. It is expected that development of this sensor leads to various applications such as medical diagnosis, biology and identification of environmental pollutant. In this stage, there are a lot of reports for development of such molecular sensors.

As one of such molecular sensors, optical functional thin films have attracted attention because these films can be easily combined with conventional spectroscopic analysis and provide us with new analytical performance via various surface effects by their photo excitation. These surface effects are divided into two types. One is surface reaction with adsorbate including photocatalytic reaction, photoisomerization and so on. The other is unique career movement such as surface plasmon (SP) excitation, charge separation and so on. The author considered that effective utilizations of these surface effects lead to development of new molecular sensors with high analytical performance.

In this thesis, the author focused on two surface effects, photocatalytic effects

and surface enhanced Raman scattering, and attempted effective utilizations of these surface effect as molecular sensors by fabricating their optical functional thin films. In this chapter, these two surface effects were discussed.

1-2 Photocatalytic effect

1-2-1 Titania

Titania is white, inexpensive, non-toxic (except for nanoparticles) and chemically stable material. From these properties, titania has been used as pigment. On the other hand, photocatalytic effect of titania was discovered by A. Fujishima in 1972. Since the discovery of photocatalytic effect of titania, titania has been studied extensively for its applications which are described in.1-2-3

Titania has three major crystal structures which include rutile, anatase and brookite. Especially, titania in anatase form is a major photocatalyst. Titania has wide band gap (3.0-3.2eV) which can absorb ultraviolet light. Photo excited titania generates electron-hole (e-h) pairs which cause photocatalytic effect.

1-2-2 Rough mechanism of photocatalytic effect

Behavior of electron-hole pairs in photo excited titania is shown below.

(a) Photo excitation of photocatalyst

1. Generation of e-h pairs (conduction band electrons and valence band holes).

(b) Reduction process

2. Conduction band electrons at titania surface reduce adsorbate molecules.

3. Conduction band electrons are trapped in titania surface.

4. Trapped electrons reduce adsorbate molecules.

(c) Oxidation process

5. Valence band holes at titania surface oxygenate adsorbate molecules.

6. Valence band holes are trapped in titania surface.

7. Trapped valence band oxygenate adsorbate molecules.

(d) Recombination process of e-h pairs

8. Recombination of e-h pairs with trapped e-h pairs occurs. This process does not contribute photocatalytic reaction.

Trapped e-h pairs are described in Fig. 1-1. Due to the generation of e-h pairs, photocatalytic effects take place at the surface of titania. In fact the photocatalytic effect is very complex because various active species such as hydroxyl radicals which produced by reaction between holes and moisture present on the surface are produced.

1-3 Surface enhanced Raman Scattering (SERS)

1-3-1 Raman scattering

Raman scattering was discovered by C.V. Raman and K. S. Krishnam in 1928 and is a type of an inelastic light scattering [1]. In this scattering process, an incident photon gains or loses its energy to interact quantized vibrational and rotational modes of an analyte molecule. In Raman spectra, these modes appear as sharp peaks and their positions depend on their transition energy, which are specific to molecular structure, along x-axis of Raman shift (cm^{-1}). Therefore, Raman measurement is recognized as a powerful tool for identification of analyte molecules. Analytical features of Raman scattering spectroscopy are shown below.

1. Construction of the measurement system is easy, because quartz or glass can be used as sample cell and optical devices.
2. The measurement in aqueous solution is possible, because Raman scattering cross sections of water molecules are much weaker than IR's one and its signal don't disturb sample's signal.
3. Measurement in a microscopic region is possible by focusing of an excitation laser.
4. One measurement gives us much information of Raman shift in large wavenumber region.

However, a general Raman spectroscopy, except for resonant Raman scattering, has a low-sensitivity compared with other spectroscopic analysis such as absorption spectroscopy, fluorescence measurement and so on. For example, typical Raman scattering cross-sections of various sample molecules are ~10^{-30} cm^2/molecule. In contrast, those of typical infrared absorption and fluorescence are ~10^{-20} and ~10^{-16} cm^2/molecule, respectively (table 1-1). Therefore, it is recognized that Raman measurement is limited to expand various applications such as molecular sensor due to this low-sensitivity.

Cross section of	Value of cross section (cm^2)
Ultraviolet absorption	10^{-18}
Infrared absorption	10^{-20}
Fluorescence emission	10^{-16}
Rayleigh scattering	10^{-26}
Raman scattering	10^{-30}
Resonance Raman scattering	10^{-24}

Table 1-1. Typical values of cross sections for various spectroscopic measurement

1-2-2 History of surface enhanced Raman scattering

Fleischmann, Hendra and McQuillan reported intense vibration spectra of pyridine adsorbed on Oxidation-Reduction-cycled silver electrode in 1974 [2]. They explained that this result is caused by an increase of number of adsorbed molecules based on an increase of surface area. However, this explanation could not satisfy other researchers in fact. In 1977, both independent groups of Jeanmaire and Van Duyne [3] and, Albrecht and Creighton [4] further examined factors which affect the huge intensity of the Raman bands of adsorbed molecules such as surface features, potential of the electrode, concentration of pyridine, and electrolyte composition of the solution, and then they concluded that the intense vibration spectra of pyridine on the Oxidation-Reduction-cycled silver electrode is caused by an enhancement of efficiency of Raman scattering itself. This effect is known as surface enhanced Raman scattering (SERS). Within a few years, intense Raman scattered signals based on SERS were verified for many molecules which are adsorbed on roughened surfaces of novel metal [5]. To this day, many researchers have been paying much attention to the huge enhancement of Raman signals based on SERS effect for various applications, and then a lot of studies for SERS have been reported. These studies have revealed that SERS has major three advantages.

1. Sensitivity is extremely high. (Comonly, intensity of Raman scattered light is enhanced to 10^3 times from 10^6 times.)
2. Spatial selectivity is high, because only molecules which adsorbed on the metal surface show SERS effect.
3. Because fluorescence of adsorbed molecules is quenched, Raman scattered light can be detected without interference of large fluorescence.

1-2-3 Proposed mechanisms of SERS enhancement effect

In many papers, origin of SERS enhancement effect has been explained by two mechanisms of electromagnetic enhancement [6] and charge transfer enhancement [7-8].

Enhanced electromagnetic field generates when incident light couples with surface plasmon (SP) phenomenon. The SP excitation is explained below. When a specific metal surface with nano-scale roughness, such as metal nano-particles and surface-roughened thin metal films, is irradiated with a specific wavelength laser, almost of the laser energy is absorbed resonantly. And then great number of excited electrons in the metal is generated and is localized on the metal surface. Therefore, these excited electrons are densified very much and induces enormous enhanced

electromagnetic field in nano-space on the surface. Calculations have shown that the electromagnetic field is greatly enhanced at dislocations or sharp discontinuities on a metal surface [9, 10]. Therefore, molecules which are adsorbed on the nano-scaled surface are exposed much larger electromagnetic field than that of irradiated light. The strength of the electromagnetic field decays exponentially from the surface but the stronger electromagnetic field induces stronger Raman scattered light within several nano-meters of the surface. Especially, in the case of metal nanoparticles, when two or more particles approach each other with gap of several nanometers, the shorter gap distance produces larger enhanced electromagnetic field in “hot site” between the particles, which reaches to more than 10^{10} times [11]. However, when this gap distance is zero, the enhancement factor of electromagnetic field significantly reduces.

In the charge-transfer enhancement mechanism, analyte molecules are bound to the metal surface to form charge transfer complexes. The incident light excites electrons in the metal and the excited electrons play a role of carrier of energy transfer to the analyte through generated new adsorption state between metal surface and sample molecules. In other words, this process is similar to that in resonant Raman scattering.

It is generally recognized that the electromagnetic enhancement factor is much larger than the charge transfer enhancement factor. Main steps of SERS mechanism

based on the theory of the electromagnetic enhancement effect are as follows [12]:

(1) An analyte molecule adsorbs on a nanostructured metal surface so that incident light couples with surface plasmon.

(2) Energy from the surface plasmon transfers to the adsorbed analyte and the Raman process occurs on the molecule, as shown in Fig. 1-1 (a).

(3) Energy transfers back to the plasmon, as shown in Fig. 1-1 (b).

1-2-4 SERS active substrates

As described above, activity of SERS effect requires nano-structured metal

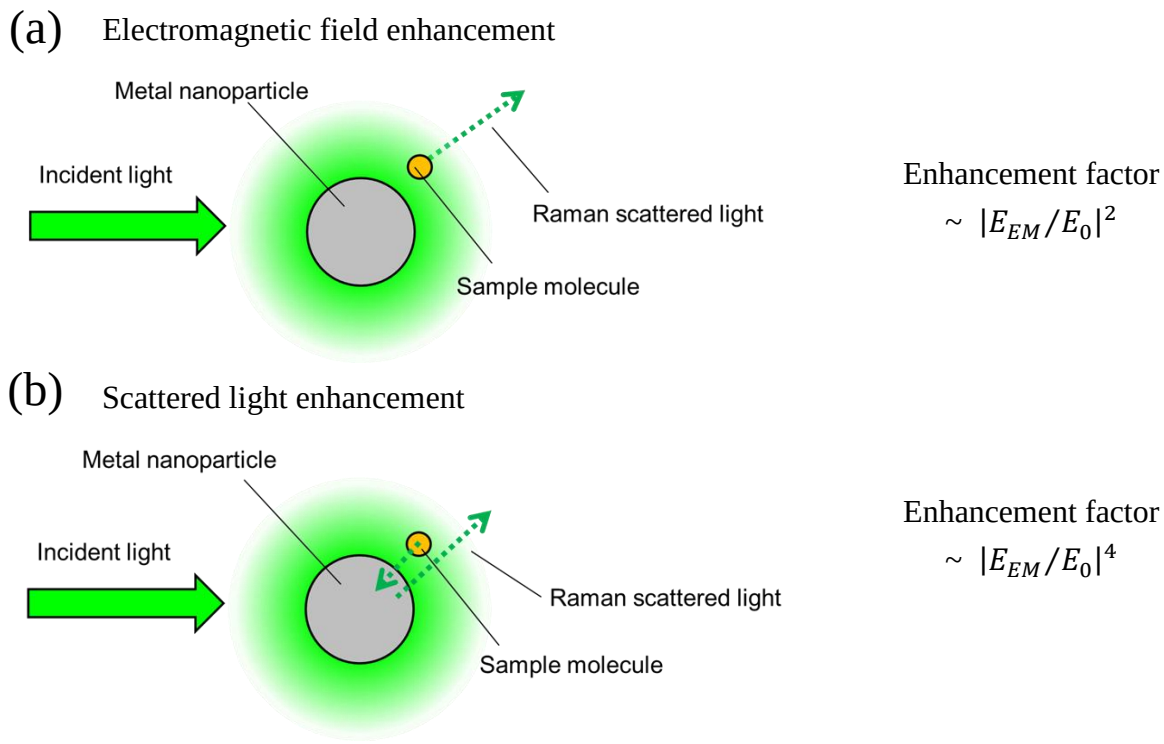

Fig. 1-1. Schematic illustration of SERS mechanism based on electromagnetic enhancement

surface. A substrate of metal with nano-sized surface roughness is called a SERS active substrate. Designing of a SERS active substrate is essential for high performance SERS measurement, because intensity and reproducibility in SERS measurement mainly depend on the surface structure of SERS active substrate such as morphology, uniformity and so on. Especially, inexpensive high-throughput fabrication of SERS active substrates with high reproducibility and large enhancement effect is a prerequisite for sensor applications.

General types of SERS-active substrates exhibiting enhancement effect are assembly of colloidal metal nanoparticles in the 10-150 nm size range, vapor-deposited films and electrodes of these metals [13]. As well as these substrates, many groups have been developing new techniques for making nanoparticles [14-23], nanoshells [24-27], nanosphere formed by nanosphere lithography [28-31], nanogaps [32-33], nanowire [34-35], and nanoholes [36-37]. For the most part of these substrates, gold or silver have been used as a material of SP excitation for making SERS substrates, although other materials such as aluminum [38], indium [39], copper [40], and gallium [41] can also support SP resonances in the UV-VIS-NIR range. Efficiencies of SP excitation typical metal are shown in Fig. 1-2 [42]. The reason why gold and silver are used mainly for SERS substrates is as follows; gold is a high chemical stability with higher efficiency of

SP excitation than that of various metals except silver. On the other hand, silver has the highest efficiency of SP excitation in various metals, although silver has a low chemical stability.

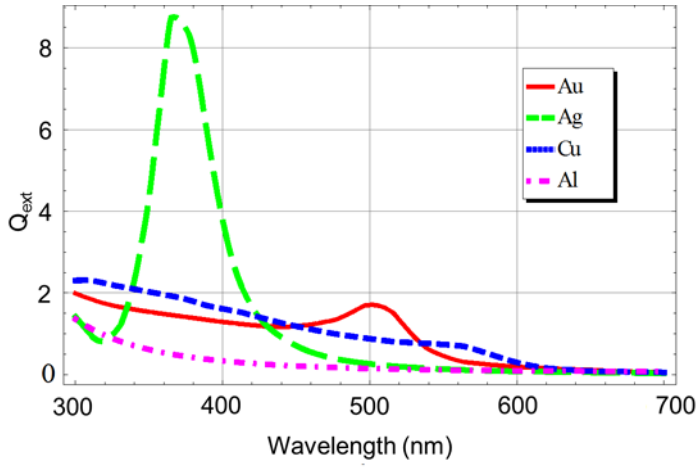

Fig. 1-2. Extinction coefficient as a function of wavelength for a metal nanoparticle (diameter: 60nm) in air. These spectra were calculated by using Mie theory by reference to [42].

1-2-5 Quantitative analysis using SERS

SERS almost has not been applied for practical uses as molecular sensors, although there are a lot of studies. The major reason is that conventional SERS has too poor quantitative performance to apply for various practical uses. This poor quantitative performance is caused by non-uniform surfaces of conventional SERS active substrates, because a magnitude of electromagnetic enhancement effect on the surface of SERS active substrate strongly depends on its morphology. Therefore, in order to apply SERS

active substrates to a quantitative analysis, control of the enhancement effect is required. In other words, uniform surface roughness of nanostructure is required. Vapor-deposited films and electrodes of these metals have too random surface roughness to control their surface roughness. Therefore, the author focused on metal nanoparticles with same shape and size. When metal nanoparticles are used as a SERS active substrate, optical properties of single metal particle have to be well controlled, that is, metal nanoparticles must not become aggregations. In the case of assembly of particles, inter-particle distance between metal nanoparticles is a very important factor because very short distance below several nano-meters generates “hot site” with a huge enhancement effect at the nano-space between metal nanoparticels. For quantitative analysis, a number of the “hot site” in measurement area should be controlled, as shown in Fig. 1-3. However, fabrication of such uniform surface roughness of nanostructure including “hot sites” is very difficult, because metal nanoparticles are easily to aggregate due to their strong attractive force based on van der Waals force.

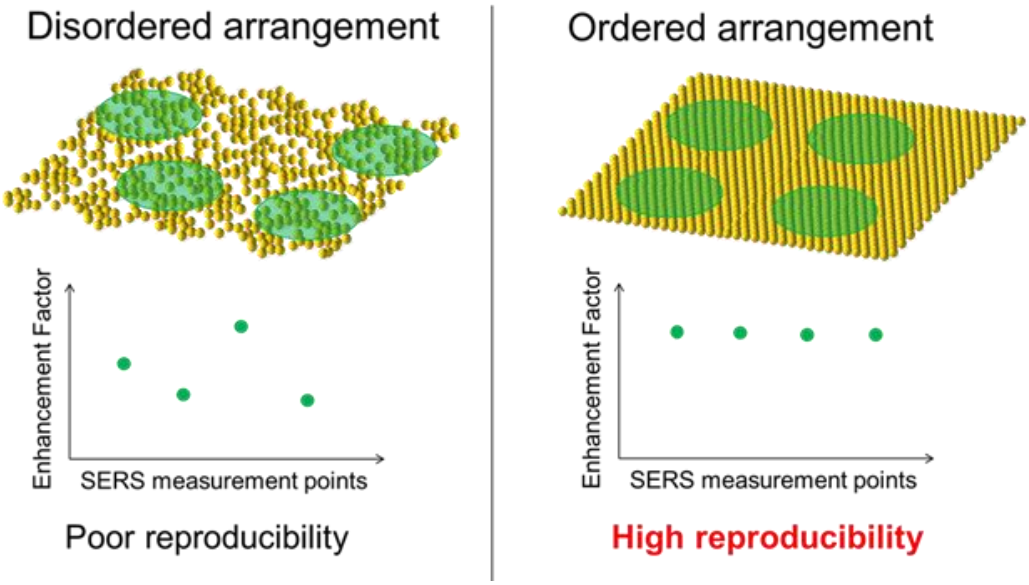

Fig. 1-3. Schematic illustration of relationship between arrangement of metal nanoparticles and reproducibility.

1-3 Purpose

In this thesis, the author aims for fabrication of two types of optical functional thin films for development of molecular sensors with high analytical performance.

Firstly, the author aims for improvement of analytical performance of surface assisted laser desorption/ionization mass spectrometry (SALDI-MS) described in Chapter 2 by using titania thin films which cause photocatalytic reactions. Commonly, mass spectrometry combined with soft ionization methods such as matrix assisted LDI-MS (MALDI-MS) and SALDI-MS provide us with molecular-weight of analyte

molecule. However, only information of molecular-weight is not enough to identify molecular structures which have many structural isomers such as sugar chains and so on. In order to identify their molecular structures, the author considered that a selective fragmentation in MS measurement is effective because site selective fragmented ions have structural information of analyte molecules. Therefore, the author paid attention to photocatalytic degradations of adsorbate molecules. In this thesis, the author fabricates titania thin films as SALDI-MS substrate and investigates relationship between titania SALDI spectra pattern and photocatalytic effect.

Secondly, the author aims for fabricating a SERS active substrate which enables to analyze quantitatively. The author considered that a nanostructured surface of the SERS active substrate should be composed by same metal nanoparticles in order to generate uniform electromagnetic enhancement field on all region of the substrate. Therefore, the author focused on highly-ordered two-dimensional metal nanoparticle array (2DMA).

However, conventional 2DMA substrates fabricated by several methods have two major drawbacks in terms of SERS sensor. One 2DMAs substrate needs surface modifiers which are usually used to prevent metal nanoparticles from aggregating due to its steric repulsion. In this case, these surface modifiers give us negative effects and are

described in chapter 3. Another one without using any surface modifiers has low uniformity in the fabricated 2DMA. These problems are discussed in Chapter 3 in detail.

On the other hand, our group succeeded in fabrication of highly-ordered 2DMA without any surface modifier by using the novel technique, which is called sandwich (SW) method. However, the 2DMA could not work for SERS analysis. The reason was that an area of the 2DMA was too small (<mm^2) to obtain many SERS spectra from one substrate and to estimate the quantitative performance, although its SERS enhancement is enough large. In this thesis, the author optimized the fabrication condition of the SW method in order to expand the area of the 2DMA, and chased a fabrication mechanism in the SW-method, simultaneously. And, the author applied the 2DMA to SERS measurement with high reproducibility.

In chapter 2, SALDI-MS measurements of oligosaccharides on the titania substrate, which were prepared by using oil/water interface trapping method, were discussed. And then the relationship between titania SALDI-MS spectra pattern and photocatalytic effect was discussed.

In chapter 3, fundamentals of localized SP (LSP), calculation of optical

properties of gold nanoparticles (AuNPs) and inter-particle coupling effect are discussed in order to understand a relationship between LSP and electromagnetic enhancement in SERS.

In chapter 4, common fabrication methods of two-dimensional metal nanostructure and the reason why the author paid attention to 2DMAs as quantitative SERS active substrates are discussed. And, the theory for interactions between colloids in solution is discussed.

In chapter 5, the fabrication method (SW-method) of 2DMAs without any surface modifier and characterization of the 2DMA using scanning electron microscope with Fourier transform analysis are discussed.

In chapter 6, mechanism of SW-method was discussed by using Vis adsorption spectroscopy and optical microscope.

In chapter 7, an analytical performance such as reproducibility and quantitatively of SW-substrate in SERS measurement is discussed.

Chapter 2

Titania surface assisted laser desorption/ionization mass spectrometry of oligosaccharides

2-1 Introduction

Laser desorption ionization (LDI) mass spectrometry (MS) was reported in the 1960's. In LDI-MS, sample molecules directly receive enough energy to desorb/ ionize from excitation laser. Detected ion species are mainly M^+ and their fragment ions. LDI-MS is appropriate for low molecular weight organic compounds which can absorb a laser. On the other hand, LDI-MS is not suitable for identification of nonvolatile compounds such as biological molecules and polymers because direct laser irradiation to such compounds cause fragmentation drastically. Thus, LDI-MS had not been paid attention until the development of matrix-assisted LDI-MS.

The matrix-assisted LDI (MALDI) was developed by K. Tanaka [43], who received the 2002 Nobel Prize in Chemistry, and F. Hillenkamp [44]. Because MALDI-MS had been improved remarkably in fragmentation of analytes with conventional LDI-MS, the use of the MALDI-MS has spread rapidly all over the world as a very effective analysis method.

In MALDI-MS, samples are prepared by mixing analytes and excessive

amounts of matrix molecules which can absorb a laser. Matrix molecules have three major roles to measure with high analytical performance. The first is that matrix molecules transfer absorbed photon energy from an exciting laser to surrounding analytes. In other words, matrix molecules assume a role of energy mediator. As a result, MALDI-MS measurement can avoid laser absorption of analyte. The second is that analytes which have strong intermolecular interactions are dispersed by matrix molecules. The third is that these molecules become a proton $[H]^+$ source to ionize sample molecules as $[M+H]^+$. From these reasons, MALDI-MS can identify high molecular-weight and nonvolatile compounds such as biological molecules and polymers with less fragmentation.

However, some drawbacks related to analytical performance exist. First, the mixture of analyte and excessive amounts of matrix molecules has large heterogeneities of not only concentration but also morphology. These heterogeneities cause too low reproducibility to analyze quantitatively. Second, LDI process produces many peaks of matrix molecules including their fragment ions and multimer. These peaks interfere with identification of low molecular-weight compounds. To overcome such drawbacks, many attempts have been made so far including use of additive such as ammonium salts, serine and cyclodextrines.

Surface-assisted LDI (SALDI) -MS is expected as one of alternative techniques for resolution of above-mentioned problem [45-47]. In the SALDI-MS, surface of inorganic material as an ionization substrate absorbs laser energy and supplies enough energy to desorb/ionize analytes on the surface. However, concerning practical utility, the remarkably lower sensitivity of the most SALDI-MS method compared to that of the MALDI-MS method, except in a few reports of SALDI-MS methods [45], is more serious than the abovementioned negative effect. The remarkably low sensitivity may be caused by the assumption that the ionization mechanisms in the SALDI methods are similar to the ionization mechanisms mainly based on rapid thermal energy supply in the MALDI method. In recent years, research on the nano-roughened surface has been progressing dramatically. Hence, their surface properties have been applied to SALDI-MS measurement for improvement the analytical performance such as sensitivity, selectivity and more. For example, Kawasaki and co-workers reported selective detection of peptides by using sulfonate group-modified FePtCu nanoparticles surface as a SALDI-MS substrate [46]. Sato and co-workers discussed interaction between surface property and SALDI-MS signal intensity by using pyroelectric substrate as a SALDI-MS substrate [47]. The author should consider that these SALDI substrates give not only thermal energy but also some surface effects from their surface

to sample molecules.

Currently, we have succeeded in detection of ultratrace samples by utilizing localized surface plasmon excitation on AuNPs surface [48]. It is understood that AuNPs can effectively absorb laser energy in the specific wavelength region via localized surface plasmon excitation, and cause charge interaction between the surface and adsorbed molecules. The author considered that the photo-excited surface may become an important key for a new application of SALDI-MS method. In this study, the author focused on a titania surface as a SALDI-MS substrate because photo-excited titania has a unique surface property based on electron-hole pairs which can cause interesting phenomena called photocatalytic reactions.

2-2 Experimental

Titania nanoparticles (Degussa, P 25) were purchased from Nippon aerosil. P25 (anatase: rutile = 3:1, average particle diameter: 30 nm) is known as a conventional photocatalytic material, which has a relatively large surface area (49 m^2/g) [49]. Titania thin films as ionization substrates were formed on n-type Si (100) (purchased from Nilaco) using a film formation method at a liquid-liquid interface (titania suspensiontoluene). For comparison, silicon substrates with comparable roughness to

the titania substrates were prepared with a sandpaper. As sample molecules, the author selected oligosaccharides, such as α-cyclodextrin (α-CD; purchased from Wako) and tetra-N-acetylchitotetraose, because these samples have no absorbance for an excitation laser. Each sample molecule was solved in ion-exchanged water (1 mmol/l) without a cationization salt. Each sample solution (ca. 1 μL, amount of sample molecules: 1nmol) was dropped on the titania thin film substrate, and then were dried at room temperature in dark room. These substrates were put into a linear time-of-flight mass spectrometer made by our laboratory with delayed extraction ion source. Acceleration voltage was 4.0kV-3.0kV and mass spectra were obtained by the positive ion mode. Nd:YAG pulsed laser FHG (λ =266 nm, 8 ns pulse width, a 10 Hz frequency) was used as an excitation laser. The laser beam was focused onto the surface with optical lens and its spot diameter was set to 0.17 mm. Its laser fluence was set to slightly stronger power (15 μJ/pulse) than thresholds for ionization of sample molecules.

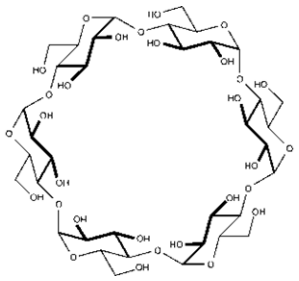

α-cyclodextrin(α-cd)

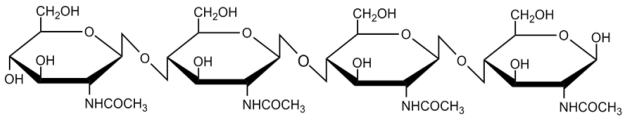

tetra-N-acetylchitotetraose

Fig. 2-1. Structural formulas of sample molecules.

2-3 Results and Discussion

Fig. 2-2 (a) shows mass spectra of α-CD measured by our method (without any cationization agents). [α-CD+Na]+ was detected strongly at m/z = 995, and several kinds of ions were detected at m/z = 349, 511, 673 and 835. The author considered that these ions come from α-CD because these ions were not detected on titania SALDI-MS substrate without α-CD. Differences in m/z values between these fragment ions were multiples of 162 Da. Because component monosaccharide of α-CD is D-glucose with

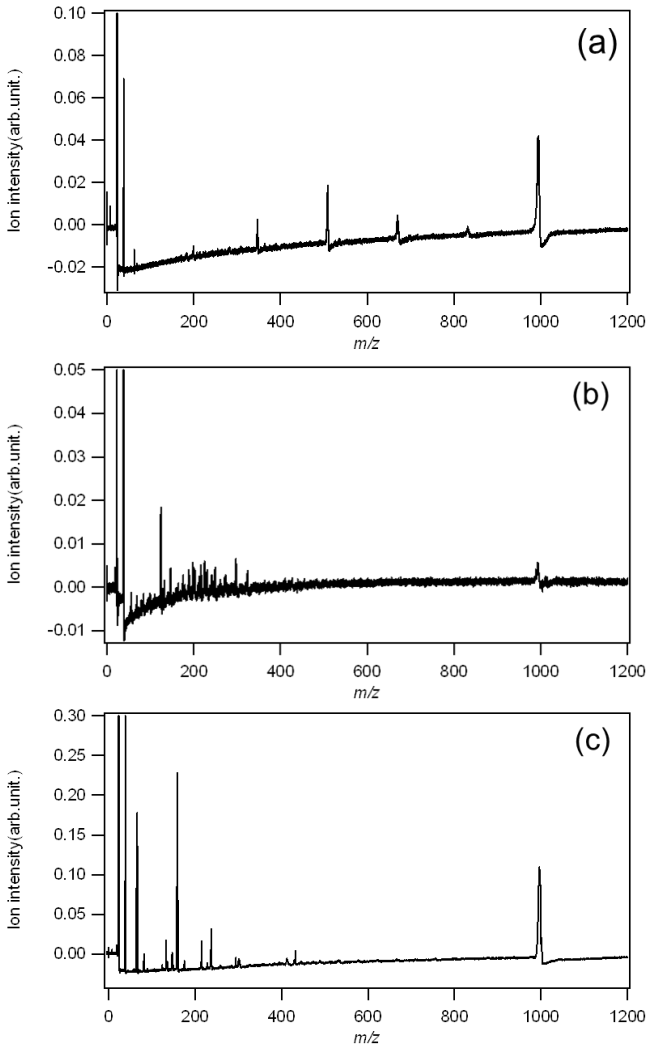

Fig. 2-2
(a) Mass spectra of a-CD measured by using a titania SALDI-MS substrate without citric acid.

(b) Mass spectra of a-CD measured by using surface roughened silicon substrate without citric acid.

(c) Mass spectra of a-CD mesured by using a titania SALDI-MS substrate with citric acid.

m/z value of 180 Da, α-CD is combination of dewatered D-glucose with m/z of 162 Da. This decrease of 162 Da agrees with decrease of number of suger units. From this reason, the author considered that these fragment ions were generated by dissociation of α-CD. However, m/z values of Na adduct biose, triose, tetraose and pentaose are 365, 527, 689 and 851, respectively, these m/z values were 16 Da higher than those of detectied ions. These differences of m/z values of 16 Da are very unique because these fragment ions were not observed by conventional LDI-MS measurement. At this stage, the author thinks that this value of 16 Da may correspond to oxygen atom in glycoside bond, although the author has no critical evidences.

In order to verify this unique result, the author attempted same SALDI-MS measurement by using surface roughened silicon substrate, as shown in Fig. 2-2 (b). In Fig. 2-2 (b), these unique fragment ions of α-CD cannot be detected with any laser fluence, although a $[\alpha\text{-CD+Na}]^+$ signal and many signals in low mass region from m/z = 150 to 350 were observed. Moreover, not only other SALDI-MS substrate such as metal nanoparticle thin film but also other excitation laser wavelengths such as 532 nm and 1064 nm gave us similar spectral pattern to this silicon substrate. It is known that these many signals in low mass region are caused by thermal dissociation. From these measurements, the author considered that these unique fragment ions on titania

SALDI-MS substrate are not caused by thermal dissociation. In order to investigate the mechanism of the non-thermal fragmentation, the author added typical cationization agent of sodium citrate (1nmol) to α-CD on titania SALDI-MS substrate, as shown in Fig. 2-2 (c), because sodium citrate is reported as a hole scavenger [50]. In Fig. 2-2 (c), detected ions were not these unique fragment ions but non-dissociated ions and thermal dissociated ions. This result shows that sodium citrate may lose charge interaction based on e-h pairs which is one of surface property of titania. For more verification, the author measured tetra-N-acetylchitotetraose (N-AT) by using titania SALDI-MS substrate without any cationization agent, as shown in Fig. 2-3. N-AT has component monosaccharide with m/z value of 221Da and is combination of dewatered monosaccharide with m/z value of 203Da. As well as Fig. 2-2 (a), $[\text{N-AT} + \text{Na}]^+$, $[\text{triose-16+Na}]^+$ and $[\text{biose-16+Na}]^+$ were detected at m/z = 853, 611 and 431, respectively. These results show that titania SALDI-MS substrate causes unique dissociation of oligosaccharide.

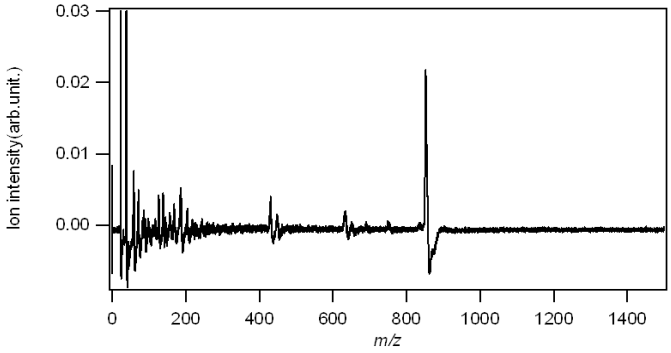

Fig. 2-3.
Mass spectra of N-AT
Measured by using
titania SALDI-MS substrate
without citric acid

In summary, SALDI-MS measurements of oligosaccharides on the titania substrate, which were prepared by using oil/water interface trapping method, were discussed. A lot of fragment ions of oligosaccharides were observed. These fragment ions had periodical molecular weight which is correspond to oligosaccharide units only by our substrate. It is suggested that the unique fragmentation process on the titania SALDI-MS substrate relates to photocatalytic reaction. Moreover, the author thinks that the unique fragmentation may be are useful to structural analysis of oligosaccharides because the titania SALDI-MS have a selective fragmentation to glycoside bonds.

Chapter 3

Localized Surface Plasmon Resonance (LSPR)

In chapter 1, the author had already described that an electromagnetic field caused by localized surface plasmon resonance (LSPR) is a dominant enhancement factor in SERS mechanisms. In this chapter, LSPR is discussed in detail in order to obtain a guideline for fabrication of a SERS active substrate with a high reproducibility and an ultra-high sensitivity.

3-1 What is LSPR?

Metal nanoparticles with a size (several tens of nanometers) much smaller than a wavelength of light exhibit brilliant colors. These colors are quite different from a bulk metal and so have attracted much interest of people. For example, AuNPs and silver NP have wine red and yellow color, respectively. And, the brilliant colors were employed in stand-glass manufacture in the middle ages. The origin of the brilliant color is attributed to strong absorption of incident light in a specific wavelength region and scattering of incident light by metal nanoparticles dispersed in medium [51-52]. And, the origin of the strong absorption is attributed to a resonance of collective oscillation of conduction electrons with incident electromagnetic radiation [53-54]. This collective

oscillation of free electrons in the metal is called a LSPR.

Plasma is described as an electrically neutral medium where an electron, ion, or its both can move freely. Since metal contains many free electrons, it can be considered to be a kind of plasma. In 1952, Pines and Bohm suggested an existence of plasma oscillation of electrons in a metallic solid to explain energy losses of fast electrons passing through metal foils [55]. This excitation is called plsmon polariton. Especially, when a surface exists, the plasma oscillation at the surface is different from that in bulk metal, as shown in Fig. 3-1. This excitation is called a surface plsmon (SP) polariton. Generally, for simplicity, the word of the polariton is often omitted.

SP associated with a metallic film whose thickness is several tens nanometers can travel across the interface between with the film and a dielectric. A type of this SP is called a propagating SP. On the other hand, SP associated with metal nanoparticles with

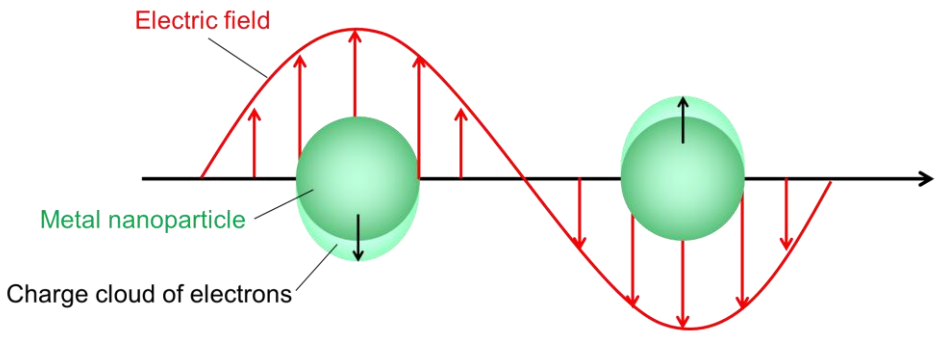

Fig. 3-1. The origin of localized surface plasmon resonance in nanoparticle

a size of several tens of nanometers is called a LSP. The LSPR caused by a coupling between electrons and incident photon in a frequency of oscillation can be characterized as a strong absorption band [56-57].

3-2 Relationship between electromagnetic filed caused by LSPR and SERS intensity

The SERS effect is a direct correspondence with the LSPR producing an intense electromagnetic field on the SERS active substrate. SERS is a phenomenon associated with the enhancement of the electromagnetic field surrounding a metal object optically excited near an intense dipole (or multipole) resonance. The radiated dipolar fields excite adsorbed molecules, and if the resulting molecular radiation remains at resonance with the enhancing object, the scattered radiation will again be enhanced. Therefore, under appropriate circumstances, an influence that the electromagnetic enhancement gives in SERS intensity can be explained as a following formula;

$$\mathrm{I}(\omega_2) = NA|L(\omega_1)|^2|L(\omega_2)|^2 I_{in}(\omega_1)$$

where $\mathrm{I}(\omega_2)$, N, A, $L(\omega_1)$, $L(\omega_2)$ and $I_{in}(\omega_1)$ are intensity of enhanced Raman scattered light, the number of molecules involved in the SERS process, Raman cross section of the molecule in contact with the surface of SERS active substrate, localized

field factor (enhancement factor of electromagnetic field) of excitation light, localized field factor of Raman scattered light and intensity of an electromagnetic field of the incident light, respectively. If enhancement factor of excitation light is as large as enhancement factor of Raman scattered light, intensity of enhanced Raman scattered light is proportional to the fourth power of the electromagnetic enhancement. Therefore, the electromagnetic enhancement based on LSPR is important for development of sensitive SERS-active substrate, and to understand the electromagnetic enhancement, optical properties of metal nanoparticles should be understood.

3-3 Dielectric functions of metal nanoparticle

Gold and silver NPs are commonly studied because they can exhibit strong LSP in the ultra violet and visible region. In this region, their optical properties can be described by a wavelength-dependent dielectric function (ε). The dielectric function (ε) is important in order to calculate optical and plasmonic property. Values of the dielectric function are complex numbers ($\varepsilon = \varepsilon' + i\varepsilon''$). Values of the complex dielectric function of bulk gold at different wavelength were obtained from Johnson and Christy [58]. And then, the dielectric function corrected for nanoparticle size ($\varepsilon(\omega)$) by using following formulas.

$$\varepsilon(\omega) = \varepsilon_{bulk}(\omega) + \frac{\omega_p^2}{\omega^2 + i\Gamma_{bulk}\omega} - \frac{\omega_p^2}{\omega^2 + i\Gamma\omega}$$

$$\Gamma = \Gamma_{bulk} + \frac{v_F}{r_1}$$

$\varepsilon_{bulk}(\omega)$ is the dielectric function of bulk gold. ω, ω_p, Γ, Γ_{bulk}, v_F and r_1 are frequency, plasma frequency of gold (13.8×10^{15} s^{-1}), damping constant of AuNP, damping constant of bulk gold (1.08×10^{14} s^{-1}), Fermi velocity (1.39×10^{8} cm s^{-1}) and radius of a AuNP, respectively. Water as surrounding medium for AuNPs with a dielectric function ε_2 was calculated a following formula reported by Thormahlen [59].

$$\varepsilon(\lambda) = \frac{5.743534 \times 10^{-3}}{\lambda^2 - 0.018085} + 1.769238 - 2.797222 \times 10^{-2} \times \lambda^2 + 8.715348 \times 10^{-3} \times \lambda^4 - 1.413942 \times 10^{-3} \times \lambda^6$$

Obtained these dielectric functions were shown in Fig. 3-2, 3-3. In future calculations, it was calculated using the values.

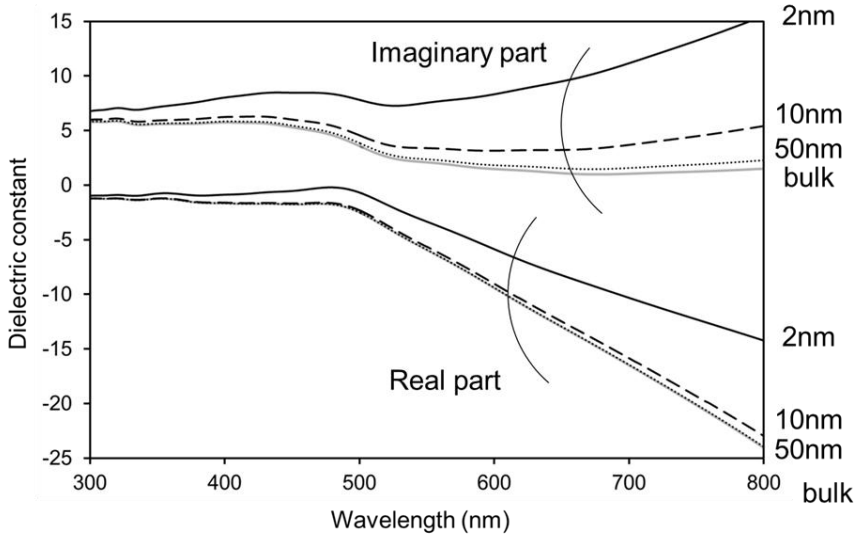

Fig. 3-2. Dielectric functions of spherical AuNPs

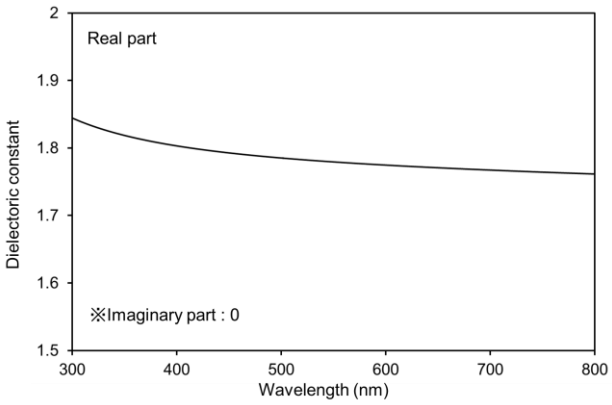

Fig. 3-3. Dielectric function of water

3-4 Quasistatic approximation

A quasistatic approximation is simple and gives good results when a diameter of particle is much smaller than the wavelength of the incident light, although this theory is classical. In this thesis, the author tried to evaluate optical properties of nanosphere by using the quasistatic approximation because the author treated with only nanosphere.

In the quasistatistic approximation, the Laplace equation for the scalar potential, Φ, can be solved.

$$\nabla^2\Psi = 0$$

(An electric field, E, is given by the gradient of the scalar potensial, $\mathrm{E} = -\nabla\Psi$.)

This formula can be represented in spherical coordinates.

$$\frac{1}{r^2}\frac{\partial}{\partial r}\left(r^2\frac{\partial\Psi}{\partial r}\right) + \frac{1}{r^2\sin\theta}\frac{\partial}{\partial\theta}\left(\sin\theta\frac{\partial\Psi}{\partial\theta}\right) + \frac{1}{r^2\sin^2\theta}\frac{\partial^2\Psi}{\partial\phi^2} = 0$$

Here, Ψ is set as follows.

$$\Psi = \mathrm{R}(r)\Theta(\theta)\Phi(\phi)$$

$$\frac{1}{R}\frac{d}{dr}\left(r^2\frac{dR}{dr}\right) = n(n+1)$$

$$\frac{\sin\theta}{\Theta}\frac{d}{d\theta}\left(\sin\theta\frac{d\Theta}{d\theta}\right) = m^2 - n(n+1)\sin^2\theta$$

$$\frac{1}{\Phi}\frac{d^2\Phi}{d\phi^2} = -m^2$$

The solution of these equations is expressed as follows.

$$\mathrm{R} = A_n r^n + B_n\frac{1}{r^{n+1}}$$

$$\Theta = C_{mn}P_n^m(cos\theta) + D_{mn}Q_n^m(cos\theta)$$

$$\Phi = E_m\exp(im\phi) + F_m\exp(-im\phi)$$

(P_n^m and Q_n^m are Legendre functions.)

When θ equal 0, $Q_n^m(cos\theta)$ diverge. Therefore, Ψ is given as follow.

$$\Psi = \sum_{n=0}^{\infty}\sum_{m=0}^{\infty}(a_n r^n + b_n\frac{1}{r^{n+1}})\,C_{mn}P_n^m(cos\theta)(\,E_m\exp(im\phi) + F_m\exp(-im\phi))$$

When an incident electric field is symmetric for z-axis, the term of φ does not exist, and only a term of m=0 remains.

$$\Psi = \sum_{n=0}^{\infty}\left(a_n r^n + \frac{b_n}{r^{n+1}}\right)P_n^0(cos\theta)$$

Moreover, when an incident electric field is plane wave incidence for the z-axis, incidence potential Ψ_0 can be described as follow.

$$\Psi_0 = -E_0 z = -E_0 r cos\theta = -E_0 r P_1^0(cos\theta)$$

From boundary condition, only a term of n=1 remains.

$$\Psi = \left(ar + \frac{b}{r^2}\right)(cos\theta)$$

An internal potential (Ψ_1) of the sphere and an outside potential ($\Psi_2 = \Psi_0 + \Psi_{sca}$) of the sphere satisfy boundary conditions on the surface of the sphere. Ψ_{sca} is scattering potential. If r_1 equals radii of the sphere, boundary condition of electric field and electric flux density are expressed as follows.

$$\frac{\partial \Psi_1}{\partial \theta}|_{r=r_1} = \frac{\partial \Psi_2}{\partial \theta}|_{r=r_1}$$
$$\varepsilon_1 \frac{\partial \Psi_1}{\partial \mathrm{r}}|_{r=r_1} = \varepsilon_2 \frac{\partial \Psi_2}{\partial \mathrm{r}}|_{r=r_1}$$

(ε_1: dielectric function of the sphere, ε_2: dielectric function of medium.)

When above differential equations are solved, Ψ_1 and Ψ_2 are expressed as follows.

$$\Psi_1 = -\frac{3\varepsilon_2}{\varepsilon_1 + 2\varepsilon_2} E_0 r cos\theta$$
$$\Psi_2 = -E_0 r cos\theta + \frac{\varepsilon_1 - \varepsilon_2}{\varepsilon_1 + 2\varepsilon_2} r_1^3 E_0 \frac{cos\theta}{r^2}$$

Electric field is explained by $\mathrm{E} = -\mathrm{grad}\,\Psi$.

$$E_1 = \frac{3\varepsilon_2}{\varepsilon_1 + 2\varepsilon_2}(E_0 cos\theta e_r - E_0 sin\theta e_\theta) = \frac{3\varepsilon_2}{\varepsilon_1 + 2\varepsilon_2} E_0 e_z$$
$$E_2 = E_0 cos\theta e_r - E_0 sin\theta e_\theta + \frac{\varepsilon_1 - \varepsilon_2}{\varepsilon_1 + 2\varepsilon_2} \frac{r_1^3}{r^3} E_0 (2cos\theta e_r + sin\theta e_\theta)$$
$$= E_0 e_z + \frac{\varepsilon_1 - \varepsilon_2}{\varepsilon_1 + 2\varepsilon_2} \frac{r_1^3}{r^3} E_0 (2cos\theta e_r + sin\theta e_\theta)$$

(e_z, e_r, e_θ are unit vectors)

This electric field is equal with the place that is generated when electric dipole moment p to be given in the next expression was put in the center of the sphere.

$$\mathrm{p} = \varepsilon_2 \alpha E_0$$

$$\alpha = 4\pi r_1^3 \frac{\varepsilon_1 - \varepsilon_2}{\varepsilon_1 + 2\varepsilon_2}$$

Therefore, we can consider the sphere in an electrostatic field to be one electric dipole put in the center. According to these formulas, when Re $(\varepsilon_1 + 2\varepsilon_2)$ equals zero, the value of α becomes very large, and this state is LSPR.

3-4-1 Scattering cross-section and absorption cross-section

As a guideline of characterizing optics properties of nanoparticles, a scattering cross section and an absorption cross section are used well. A scattering cross section is a cross section of the incident planar wave to equal all power of the scattered light. An absorption cross section is a similar definition. Moreover, an extinction cross section is a sum of a scattering cross section and an absorption cross section. These are explained as following formulas. In these calculations, a formula of polarizability which is corrected for nanoparticle size was used, because an above-mentioned formula of polarizability lacks a precision to obtain these cross sections. In this thesis, the author didn't use the above-mention formula but a formula corrected for a size of nano-particles calculation of polarizability.

Scattering cross-section: $C_{sca} = \frac{k^4}{6\pi}|\alpha|^2$

Absorption cross-section: $C_{abs} = k\, Im(\alpha)$

Extinction cross-section: $C_{ext} = C_{sca} + C_{abs}$

α: polarizability (corrected for nanoparticlesize [60]):

$$\alpha = 4\pi r_1^3 \frac{(\varepsilon_1 - \varepsilon_2)\left(1 - \frac{q^2}{10}\right)}{(\varepsilon_1 + 2\varepsilon_2) - \left[\frac{7}{10}\varepsilon_1 - \varepsilon_2\right]q^2 - (\varepsilon_1 - \varepsilon_2)i\frac{2}{3}q^3}$$

ε_1: dielectric function of a AuNP

ε_2: dielectric function of surrounding medium such as air, water and more

$$q = \frac{2\pi r_1}{\lambda} \ (q: size\ parameter)$$

3-4-2 Calculation of optical properties of gold nanospheres

Figure 3-4 (a) and (b) show calculated spectra of the absorption and scattering cross-sections for spherical AuNPs (diameter: 20, 60 and 100nm) normalized by its volume in water.

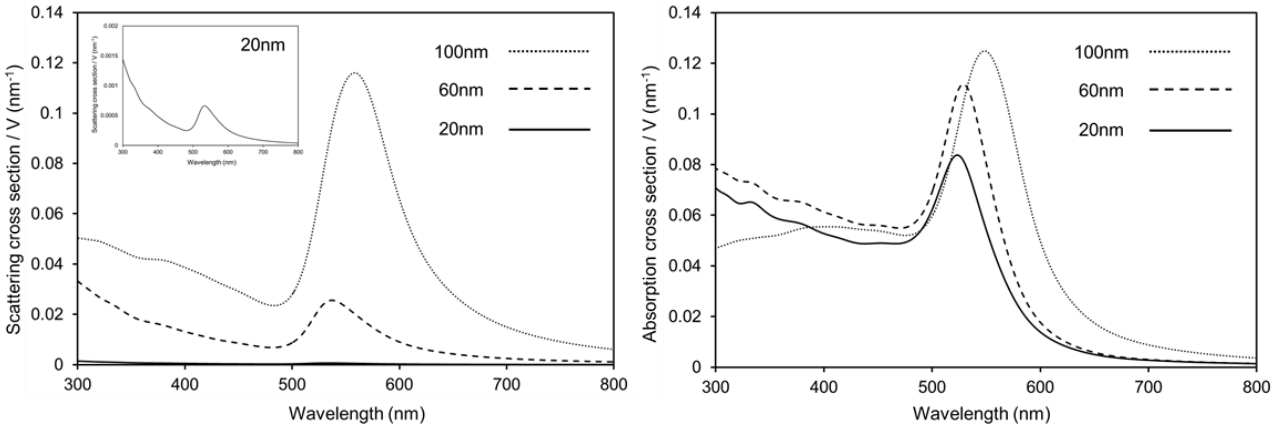

Fig. 3-4. (a) Scattering cross-sections normalized by volume of spherical AuNPs (diameter: 20, 60, 100nm) (b) Absorption cross-sections normalized by volume of spherical AuNPs (diameter: 20, 60, 100nm)

Strong peaks due to LSPR were observed from 500nm to 600nm on both spectra of the scattering cross-section and the absorption cross section. Shorter diameter gave us lower values of scattering cross section. This tendency is caused by a larger value of an imaginary part of dielectric constant for smaller diameter of the nanoparticle. On the other hand, a larger diameter of the nanoparticle gave us a larger shift of the strong peak. It is considered that this red shift is caused by an increase of mean free path of electrons excited by LSP in the particle.

Next, to evaluate the validity of the calculation, the author compared the result of calculation with experimental value. Dotted line in figure 3-5 (a) is a measurement data of an absorption spectrum of AuNP (diameter: 60nm) colloidal solution.

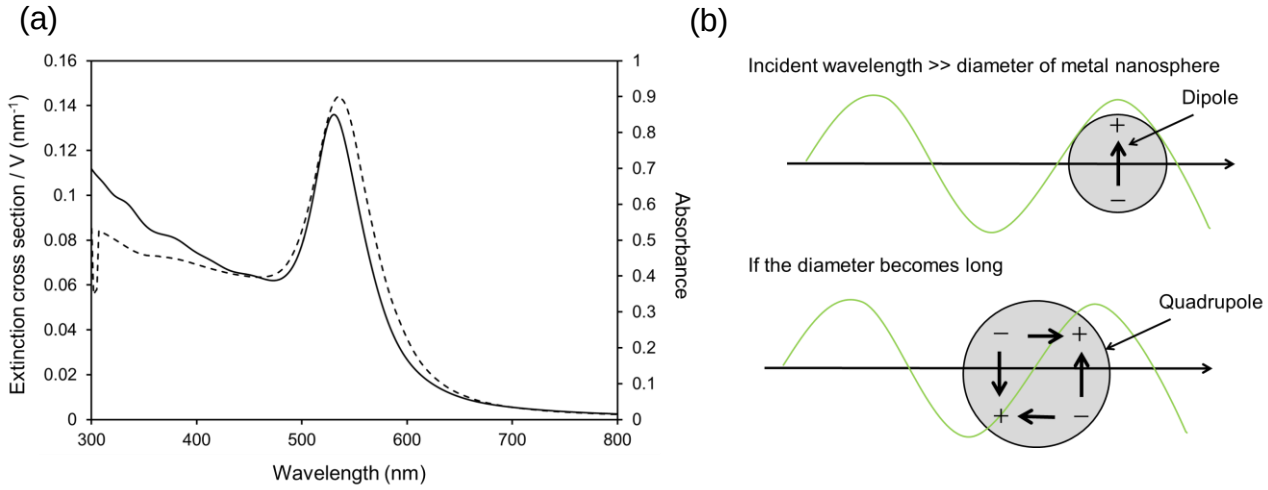

Fig. 3-5 (a). (solid line) Extinction cross-sections normalized by volume of spherical AuNPs (diameter: 60nm) (dotted line) A measurement data of an absorption spectrum of AuNP (diameter: 60nm) colloidal solution. (b). An image of retardation effect

The calculated spectrum and the experimental spectrum were almost in agreement, although there were a slight difference (λ_{max} of calculated spectrum: 529nm, λ_{max} of experimental spectrum: 536nm) in a wavelength of maximum absorption between these two spectra. This slight difference may be caused by (A) change of the dielectric constant of material by existence of an electrolyte or (B) retardation effect (dipole → quadrupole; described in Fig. 3-5 (b)) of phase in the nanoparticle. However, the author selected this calculation method for behavior of LSP in an absorption spectrum because

this slight difference can not affect our discussion of SERS evaluation in this thesis.

3-4-3 Suitable diameter of nanosphere for the SERS measurement

Using the above calculation method, the author estimated a diameter of particle that is suitable for SERS measurements. In this thesis, the author used a Nd:YAG laser with a wavelength of 532nm as a light source of SERS measurement because this wavelength is included in the wavelength region of the LSPR absorption of AuNPs. Fig. 3-6 shows a diameter dependency of these absorption cross sections at the wavelength of 532nm. As a result, values of from 60nm to 100nm were large compared with other diameters and this result was good agreement with a published data [61]. This means that nanoparticles with a diameter from 60 nm to 100 nm have high efficiency of SP excitation. Moreover, K. Shibamoto and co-workers reported that a particle diameter dependency of SERS intensity was evaluated by using two dimensional AuNP arrays with high-density as SERS active substrates and a diameter of 60nm has a strongest SERS intensity [62]. A slight difference between the calculated results and these experimental results may be caused by plasmonic interaction described in following section and a difference of surface-to-volume depended on its diameter.

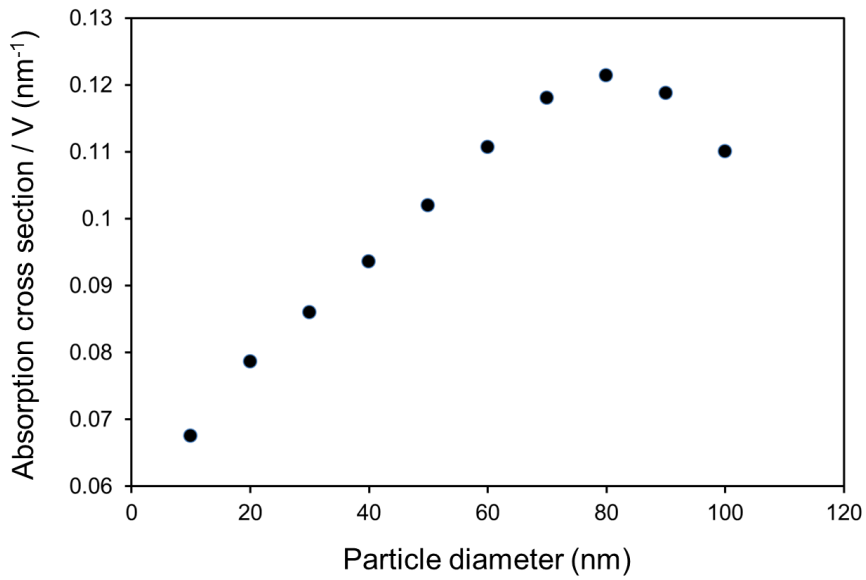

Fig. 3-6. Particle diameter dependency of absorption cross section

3-5 Electromagnetic field caused by LSPR excited on a spherical nanoparticle

Enhanced electromagnetic field caused by LSPR can be explained by dipole radiation. Electric field amplitude by LSPR excited on a spherical nanoparticle can express by a following formula in spherical coordinate. A derivation process was omitted, because this process is quite complicated.

$$\mathrm{E}(\mathrm{r},\theta) = \frac{\alpha E_0 \exp(ikr)}{4\pi}\left[2cos\theta\left(\frac{1}{r^3}-\frac{ik}{r^2}\right)e_r + sin\theta\left(\frac{1}{r^3}-\frac{ik}{r^2}-\frac{k^2}{r}\right)e_\theta\right]$$

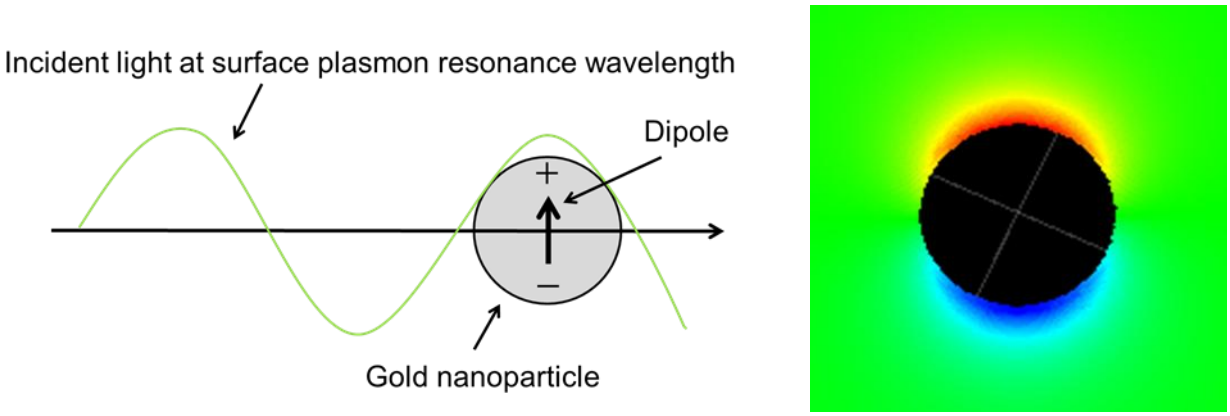

Fig. 3-7. A plot of electric field amplitude by localized surface plasmon resonance of a spherical nanoparticle

3-6 Strong electromagnetic field caused by interaction of nanoparticles

When two metal nanoparticles approach each other to several nanometers below, a dipole of one particle interacts with a dipole of the other particle [63-64]. In this case, the interaction (coupling) generates significantly stronger electromagnetic field in the space between nanoparticles compared with that on a surface of a single particle. This strong electromagnetic field in the nano-space is recognized as an origin of hot sites in SERS measurement. In fact, there is almost no report of SERS measurement on an isolated nanoparticle because of its lower enhancement factor compared with that of other SERS substrates.

In order to generate this hot site, matching between a vibration direction

(polarization direction) of the incident electric field and the placement of two particles is very important, as shown in Fig. 3-8.

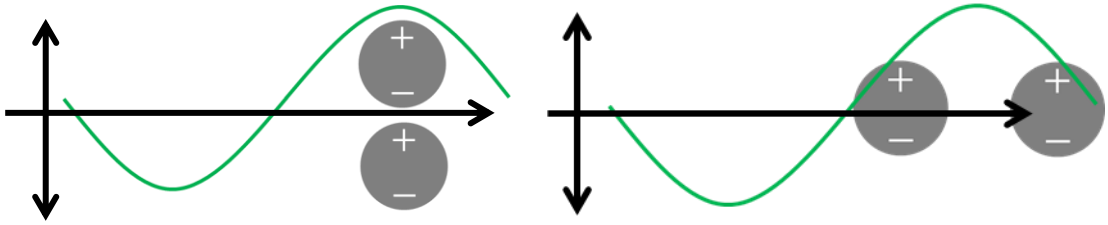

Fig. 3-8. Illustrations of vibration direction of the interaction between the incident light and the placement of two particles

When two nanoparticles are placed parallel to the vibration direction of the incident electric field, two polarizations as shown in the above figure occur in two nanoparticles. As a result, strong electromagnetic field is generated at the center of the condenser-like junction. It is considered that excited dipoles interact strongly each other (dipole-dipole interaction). However, if two nanoparticles contact directly, the stronger electromagnetic field cannot be generated. On the other hand, when two nanoparticles are placed vertically to the vibration direction of the incident electric field, the above-mentioned strong electromagnetic field at the center of the junction cannot be generated. In this case, excited dipoles cannot interact strongly each other due to the placement of two nanoparticles. For this system, there are a lot of studies to clarify the

mechanism and apply this strong electromagnetic field to enhancement of spectroscopic analysis.

According to a report of a theoretical calculation [65] (Fig. 3-9), a peak corresponding to the LSPR of a AuNP in an absorption cross-section shifted towards longer wavelengths. Moreover, a new peak appeared in longer wavelength region than the wavelength of the main peak. On the other hand, the intensity of the electromagnetic field was larger when the distance between these nanoparticles was shorter, and depended on wavelength. These calculated results have been demonstrated in many experiments. In other published report [66], optical responses of heptamers of AuNPs

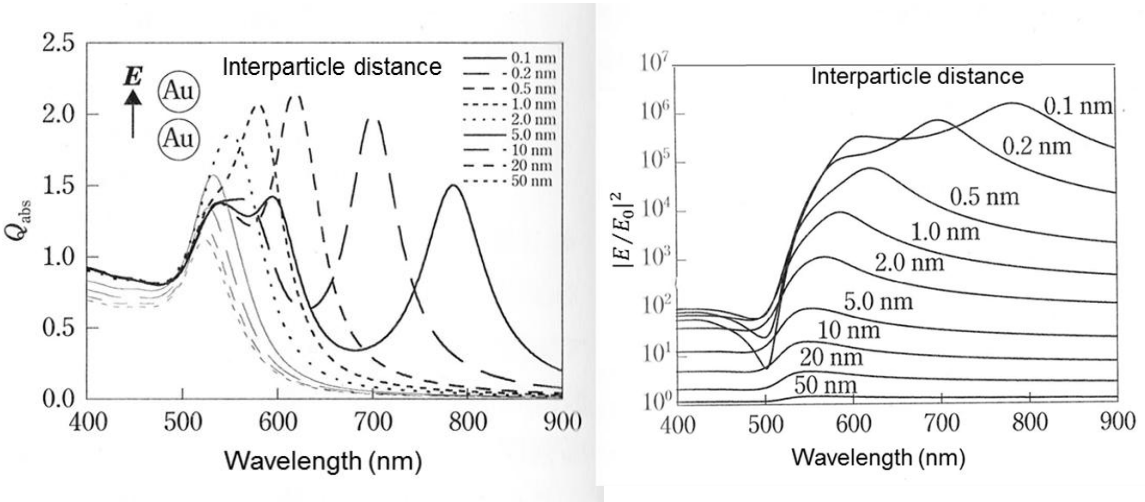

Fig. 3-9. (a). Dependence of absorption cross section on inter-particle distance
(b) Dependence of electromagnetic field enhancement on inter-particle distance
These figures were citation date from T. Okamoto and K. Kajikawa, plasmonics, 2010, Kodansya scientific [65]

with various inter-particle distances were evaluated and interactions of optical responses between nanoparticles were discussed by comparing experimental results with calculated results. As shown in this report (Fig. 3-10), the behavior of a heptamer is quite different from that of a dimer and an arrangement of nanoparticles has a cross relationship with an optical response in LSPR. Therefore, a control of the arrangement of nanoparticles is very important for fabrication of a SERS active substrate.

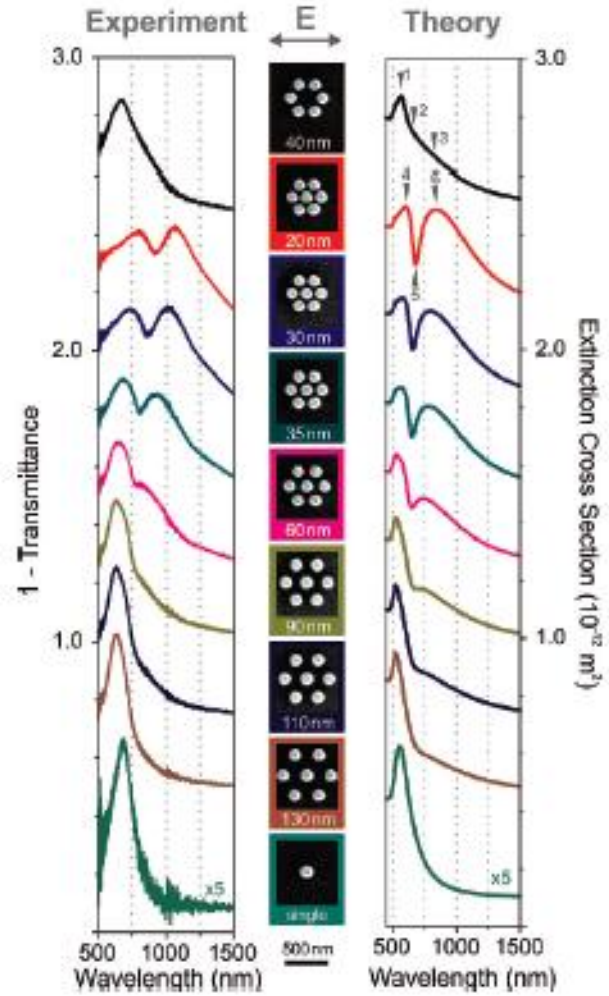

Fig. 3-10
Extinction spectra of a gold monomer, a gold hexamer and gold heptmers with different inter-particle distance.
This date was cited by
M. Hentschel, M. Saliba,
R. Vogelgesang, H. Giessen,
A. P. Alivisatos and N. Liu
Nano lett. 2010, 10, 2723 [66]

Chapter 4

Methodology of fabrication of two-dimensional metal nano-structured surfaces

4-1 Introduction

Fabrication of two-dimensional (2D) metal nano-structured surfaces with high uniformity is a key technology for application of molecular sensors based on SERS, because molecular sensors requires high analytical performances such as high sensitivity, identification ability, quantitative ability and so on. Previously, a number of methods for fabrication of 2D metal nano-structured surfaces on a supporting substrate have been proposed. In this chapter, various methods of fabrication of metal nano-structured surfaces are discussed to obtain a guideline of fabrication of a SERS active substrate with high reproducibility and ultra-high sensitivity. And behaviors of colloidal particles are discussed to understand a nature of colloidal particles.

4-2 Various methods for fabrication of two-dimensional metal nano-structured surfaces

Various methods for fabrication of 2D metal nano-structured surfaces have been proposed so far, and are classified roughly like the following figure 4-1.

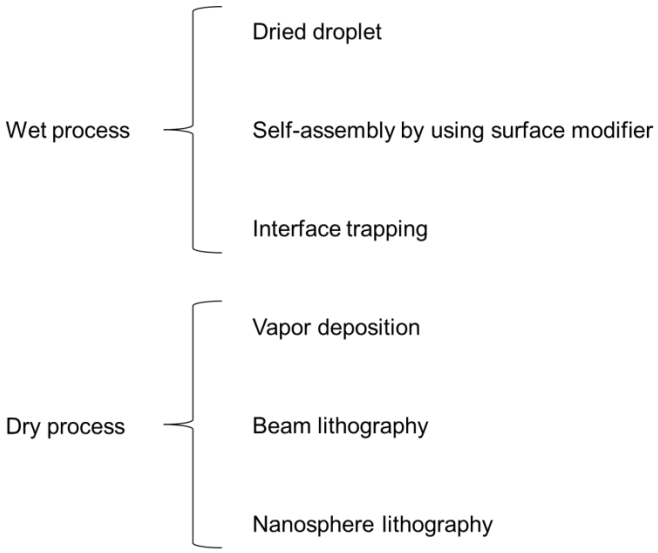

Fig. 4-1. Classification of various methods for fabrication of 2D metal nano-structured surface

In a dry process, 2D metal nano-structured surfaces are fabricated on supporting substrates directly by physical methods. Commonly, dry processes need expensive and huge devices for nanoengineering. Therefore, fabrication methods in the dry process cost a lot of money, although a part of these methods such as beam lithography method can fabricate a enough precise nanostructure to satisfy users' requests. From these reasons, the dry process method is not suitable for practical uses.

On the other hand, in a wet process, metal nanoparticles in solution are mainly used as building blocks of 2D metal nano-structured surfaces on a supporting substrate. Fabrication methods in the wet process cost not so much money commonly because this process requires only materials. In a view of practical uses, this wet process is much

more suitable for fabrication of 2D nano-structured surfaces than the dry process. In the wet process, fabrication of highly-ordered 2D metal nanoparticle arrays (2DMAs) is important to obtain 2D metallic nanostructured surface with high uniformity.

4-2-1 Dried droplet method

Dried droplet method is one of the simplest methods for fabrication of 2D nanostructured surfaces. In this method, metal nanoparticle colloidal solution is dropped onto a supporting substrate, and the droplet is dried completely. As a result, metal nanoparticles are deposited on a supporting substrate. However, metal nanoparticles are thermodynamically metastable and easily aggregate due to its large van der Waals attraction. As a result, a lot of aggregations with various sizes form at random positions on the substrate. Therefore, the fabricated structure by this method has a low uniformity, which is a world apart from a highly-ordered 2DMA.

Moreover, the fabricated structure has a characteristic ring pattern which is known as a coffee ring [67]. This formation is caused by a pinning of an edge of the droplet because this pinning effect prevents the edge from moving to inside of the droplet and keeps oversupplying nanoparticles along a curvature of the droplet. On the other hand, in a case of non-metallic colloidal particles such as polystyrene particles and

silica particles, these particles can form a highly-ordered 2D particle array by this method [68-69].

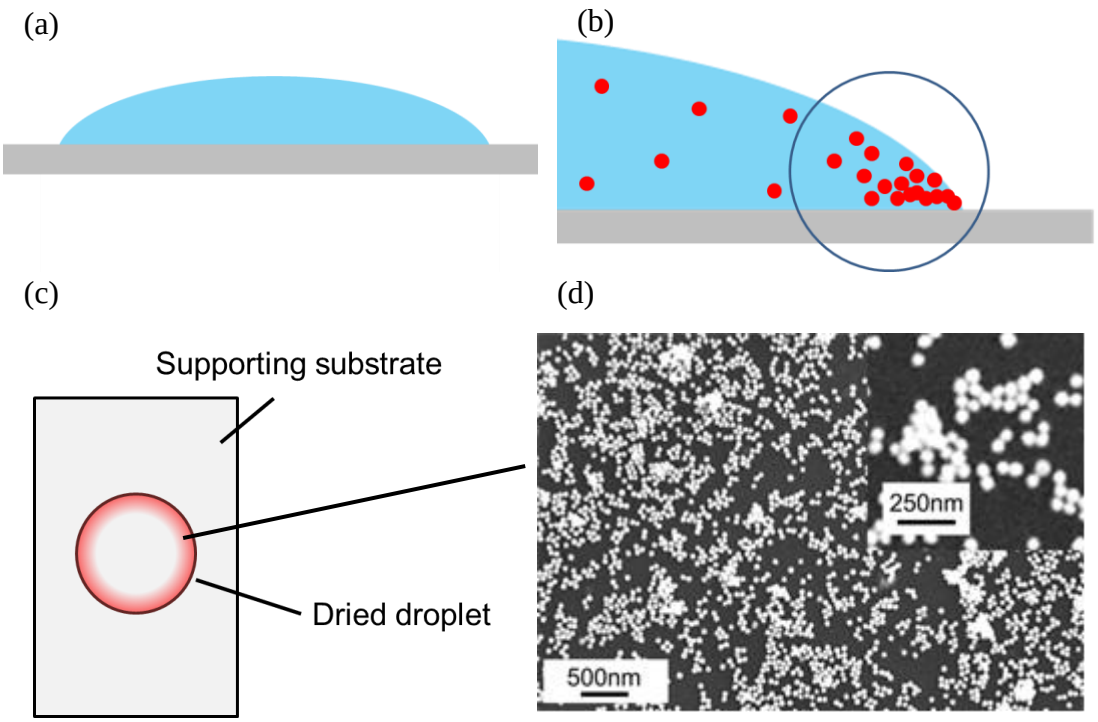

Fig. 4-2. Schematic illustration of dried droplet method; (a) a shape of droplet on a flat substrate (b) behavior of metal nanoparticles near the contact line (c) Overall view of dried droplet substrate (d) SEM image of dried droplet substrate.

4-2-2 Self-assembly method by using surface modifiers

Surface modifiers prevent nanoparticles from aggregating because these molecules play a role of spacer between particles. Self-assembly method by using surface modifier is devised to overcome aggregations of above-mentioned dried droplet method [70-74]. In this method, metal nanoparticles are decorated by surface modifiers

such as alkanethiol, fatty acid and so on. As a result, decorated metal nanoparticles arranged in highly-ordered 2D metal nanoparticle array (2DMA) by only dropping its solution. This method has two major advantages for fabrication of a highly-ordered 2DMA.

1. This method can easily fabricate 2D metal nano-structured surfaces with a high uniformity.
2. Inter-particle distances which are important for generation of hot sites are tunable by changing molecular length.

However, surface modifiers give us three major negative effects for SERS measurement.

1. Surface modifiers change optical properties of metal nanoparticles.
2. SERS signals of surface modifiers are observed strongly, and these signals interfere in detection of analyte molecules.
3. Surface modifiers prevent analyte from adsorbing directly on a metal surface, and introducing to hot site.

From these problems, the author considered that use of the surface modifier should be avoided for fabricating of SERS sensors.

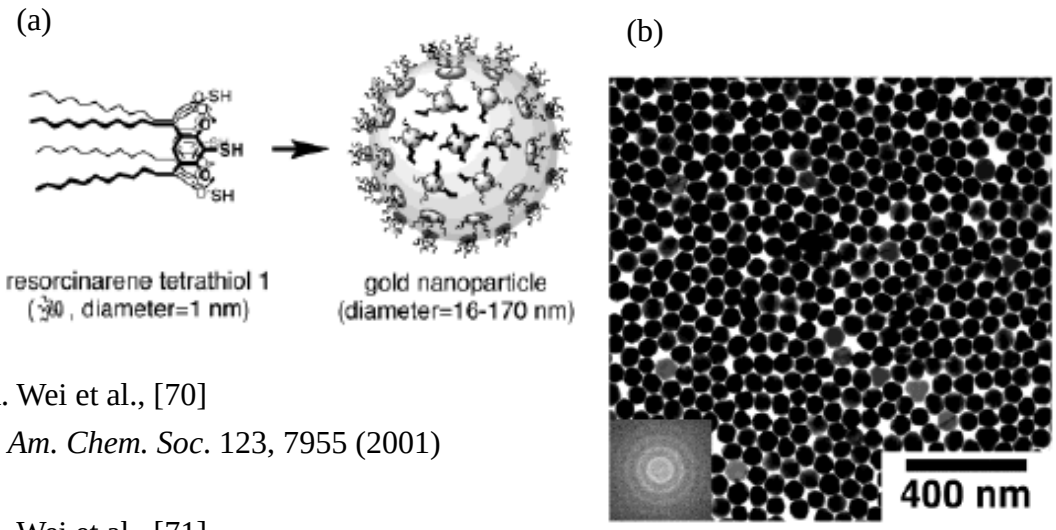

A. Wei et al., [70]
J. Am. Chem. Soc. 123, 7955 (2001)

A. Wei et al., [71]
Chem. Phys. Chem. No. 12 (2001)

Fig. 4-3. A. Wei and co-workers developed a surface modifier based on calixarene to prevent aggregate of AuNPs. (a). image of the surface modifier and modified AuNP (b). electron microscope image of a 2DMA composed by the modified AuNPs.

4-2-3 Interface trapping method

In an interface trapping method, metal nanoparticles in solution are trapped at an interface between oil and water or air and water, and then the layer of the trapped metal nanoparticles is transferred from the interface to a supporting substrate [75-76]. The layer of metal nanoparticles is almost monolayer and its density of metal nanoparticles is larger than that of a substrate fabricated by the dried droplet method. In this method, bare metal nanoparticles can be used, although metal nanoparticles easily aggregate due to its large van der Waals attraction. This method has three major

advantages for fabrication of 2DMAs.

1. Very large-area of the 2DMA (cm^2 order) can be obtained.

2. The fabrication procedure is quite easy.

3. The 2DMA is almost monolayer.

However, this method has two drawbacks for fabrication of highly-ordered 2DMAs.

1. The 2DMAs composed by bare metal nanoparticles have a low uniformity due to formation of a lot of aggregations.

2. The 2DMAs is mainly composed by 2D aggregations, which cannot generate strong electromagnetic field.

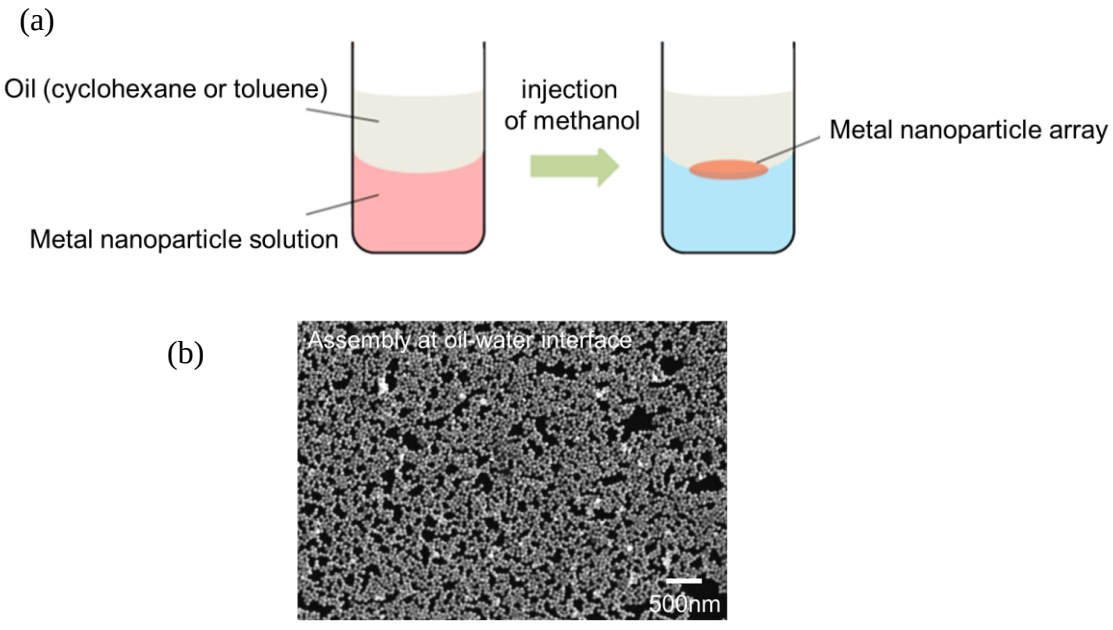

Fig. 4-4. (a) Schematic illustration of oil-water interface trapping method
(b) SEM image of a 2DMA fabricated by the method.

4-2-4 Vapor deposition method

Vapor deposited layers of metals with a thickness of several tens of nanometers on a supporting substrate [77] can become a SERS active substrate. When a pressure in vapor deposition is high such as several Pa, the evaporated metal has an island structure on a supporting substrate. As a result, the island structure has a SERS activity. This method is easy due to its simple vapor deposition process. However, a control of morphology of the nano-structured surface is very difficult because the thin film is formed by random collisions between metal clusters and a supporting substrate. Therefore, the vapor deposition method is not suitable for fabrication of a two-dimensional (2D) metal nano-structured surface with high uniformity.

4-2-5 Beam lithography

Beam lithography methods such as electron beam lithography methods [78-80] and focused ion beam methods [81-82] can control morphology of nano-structured surface such as size, shape, and lattice spacing of nanostructures. In the electron beam lithography method, the desired pattern can be produced by exposing a photo-resist layer to high energy electron beams, followed by chemical development and deposition of the noble metal. However, these lithography methods have two major drawbacks.

The first is that it costs very high due to very expensive equipments. The second is that its diffraction limited resolution is ca. λ/2. Therefore, these lithography methods can't create the hot site.

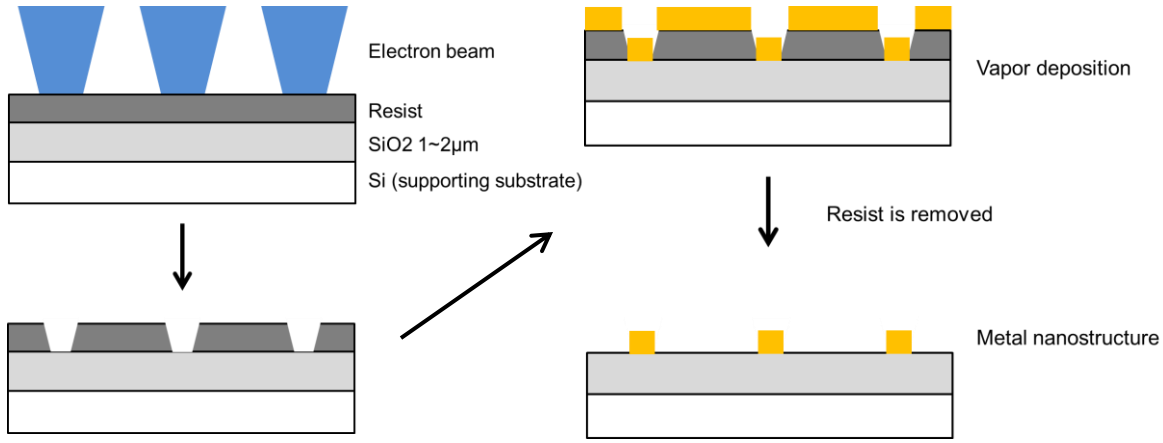

Fig. 4-5. Schematic illustration of electron beam lithography

4-2-6 Nanosphere lithography

Van Duyne and co-workers have developed a nanosphere lithography method [83-85]. The nanosphere lithography method is an inexpensive, high-throughput, and materials-general nanofabrication technique, which is capable of producing well-ordered 2D particle arrays of nanoparticles with a high periodicity. The conventional nanosphere lithography process begins with self-assemmbly of a nanosphere mask onto a substrate followed by deposition of a metal through the mask. The nanosphere used as deposition masks are usually polystyrene or silicon

nanoparticles, because these particles can be arranged easily. Diameters of the nanosphere determine a size and inter-spacing distance of nanoparticles in fabricated 2D arrays. Previously, nanosphere lithography was one of the most common methods for fabrication of SERS active substrates.

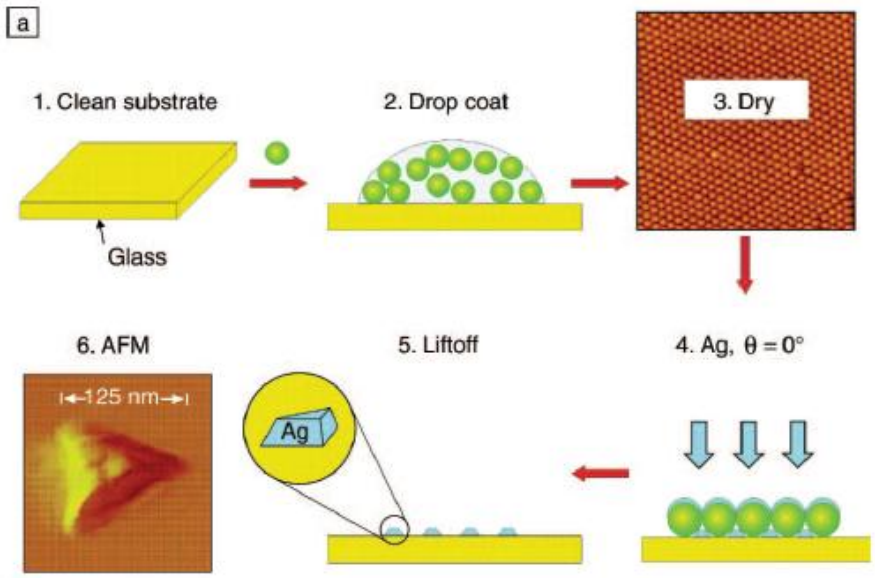

Fig. 4-6. Schematic illustration of nanosphere lithography

Amanda J. Haes et al. MRS Bulletin vol 30 2005 [85]

4-3 Guideline of fabrication of a SERS active substrate with high reproducibility and ultra-high sensitivity

In this thesis, the author aimed for fabricating a SERS sensor which has a high reproducibility and a ultra-high sensitivity. Moreover, in term of a practical use, the sensor should be robust and cost-effective. A SERS active substrate obtained by the dry

process is too expensive to use for a sensor, although the dry process can fabricate a precise nanostructure. Therefore, the author has paid much attention to the wet process. Especially, the author considered that highly-ordered 2DMAs composed by same AuNPs without any surface modifiers are suitable for SERS sensor, because AuNP has a high chemical stability and a high efficiency of SP excitation. However, there still remains as a big issue to fabricate highly-ordered 2DMAs. This big issue is that it is very difficult to fabricate highly-ordered 2DMA without any surface modifier. Therefore, theories for a behavior of colloidal nanoparticles are described in next section.

4-4 Theories of colloidal nanoparticles

Various kinds of forces between colloidal particles in solution depend on their particle diameters dominantly, as shown Fig. 4-7.

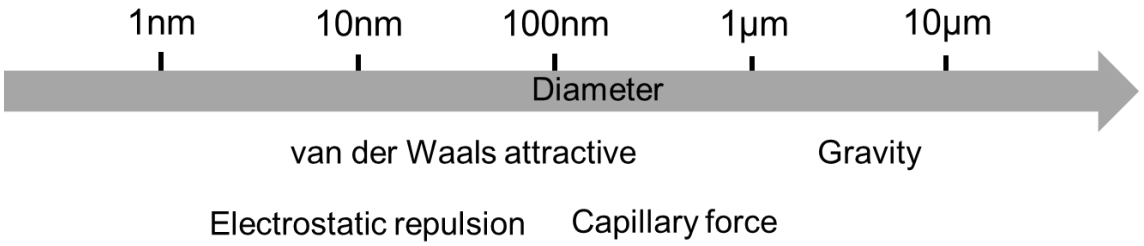

Fig. 4-7. Various kinds of forces between colloidal particles in solution on their particle diameters

For nanoparticles with diameters from 60 nm to 100 nm, van der Waals attractive force

and electrostatic repulsive force interact each other mainly. On the other hand, a gravity force hardly acts on metal nanoparticles due to too small mass of metal nanoparticles. Because the author don't know whether a capillary force acts on metal nanoparticles or not in this stage, further discussion for this force is required. In addition, it is known that all colloidal particles behave Brownian motion. Brownian motion assists a self-assembly process of nanoparticles but becomes a major factor of aggregation.

4-4-1 Brownian motion

The Brownian motion is a well-known feature of colloidal particles in solution. The Brownian motion means that colloids always move in solution at random. And, the intensity of motion affects probability of collisions between particles. The root-mean-square motion $\langle r^2 \rangle^{\frac{1}{2}}$ of the particle in time t due to random walk can be quantified using Stokes-Einstein diffusion coefficient D_0;

$$\langle r^2 \rangle^{\frac{1}{2}} = \left(\frac{2kT}{6\pi\eta r} \times t \right)^{\frac{1}{2}} = (2D_0 \times t)^{\frac{1}{2}}$$

k, T, η and r are Boltzmann's constant, the absolute temperature, the solvent viscosity and particle radius, respectively.

This formula shows that a higher temperature activates more intense motion of the particle. As a result, the high temperature increases a probability of collision

between particles, and then these particles aggregate. However, it is difficult to understand the aggregation condition or colloidal stability of nanoparticles from only this formula. Considering aggregation of nanoparticles, DLVO theory is very important and is described in the next section.

4-4-2 Derjaguin-Laudau-Verwey-Oberbeck (DLVO) theory

Derjaguin-Laudau-Verwey-Oberbeck (DLVO) theory is based on the idea that pairwise interaction forces, which arise from the interplay of van der Waals attraction force and electrostatic repulsive force [86-88]. The colloidal particles are dispersed stably when the repulsive force is larger than the attractive force, whereas the colloidal particles form aggregation when the attractive force is larger than the repulsive force.

DLVO theory states that the total interaction potential between two nanoparticles can be expressed as the sum of the van der Waals attractive force (V_{vdW}) and electrostatic repulsive force (V_{elec}).

$$V_{total} = V_{vdW} + V_{elec}$$

Essentially, a magnitude of the attractive force depends on the difference in permittivities of the interacting bodies and intervening media. For spheres, the van der Waals attractive force takes a following formula.

$$V_{vdW} = -\frac{1}{6}A\left(\frac{2R_1R_2}{d^2-(R_1+R_2)^2} + \frac{2R_1R_2}{d^2-(R_1-R_2)^2} - \ln\frac{d^2-(R_1+R_2)^2}{d^2-(R_1-R_2)^2}\right)$$

A is Hamaker coefficient, and d is the center-to-center distance between particles of radius R_1, R_2. Hamaker coefficient plays an important role in the description of attraction energy between the particles [89-90]. The Hamaker constant can be represented by the equation.

$$A_{121} = \left(\sqrt{A_{11}} - \sqrt{A_{22}}\right)^2$$

The term A_{11} represented a AuNP-AuNP interaction and A_{22} corresponds to the solvent interaction. According to literatures of [91-92], a value of A_{11} and A_{22} were used as 4.5 $\times 10^{19}$ J and 0.4 $\times 10^{19}$ J respectively. Therefore, a value of A_{121} can be calculated as 2.2 $\times 10^{19}$ J.

On the other hand, electrostatic repulsive force between two colloidal particles can be expressed in the following two formulas.

$$V_{elec} = 4\pi\varepsilon\psi_0^2 \frac{R_1 R_2}{R_1 + R_2} \ln\left(1 + exp(-\kappa x)\right) \quad (in\ the\ case\ of\ \kappa R < 5)$$

$$V_{elec} = 4\pi\varepsilon R_1 R_2 Y_1 Y_2 \left(\frac{k_B T}{e}\right)^2 \frac{ex(-\kappa x)}{x + R_1 + R_2} \quad (in\ the\ case\ of\ \kappa R < 5)$$

$$\kappa = \left[\frac{1000 e^2 N_A (2I)}{\varepsilon k_B T}\right]^{1/2}$$

$$Y_i = \frac{8tanh\left(e\psi_0 / (4k_B T)\right)}{1 + \left[1 - \frac{2\kappa R_i + 1}{(\kappa R_i + 1)^2} tanh^2\left(e\psi_0 / (4k_B T)\right)\right]^{1/2}}$$

ε is the permittivity of a medium, ψ_0 is the potential at the particle surface which can be estimated from ζ potential measurement, κ is inverse of the Debye length, x is the distance of closest approach between two particle surfaces, e is the electronic charge, k_B is the Boltzmann's constant, T is the temperature, N_A is the Avogadro number and I is the ionic strength of the solution.

Fig. 4-8 shows the DLVO potential curves of AuNP in aqueous solution. Because the author cannot obtain experimental value of the AuNP colloidal solution such as ζ potential and ion strength, the author employ literature values [93].

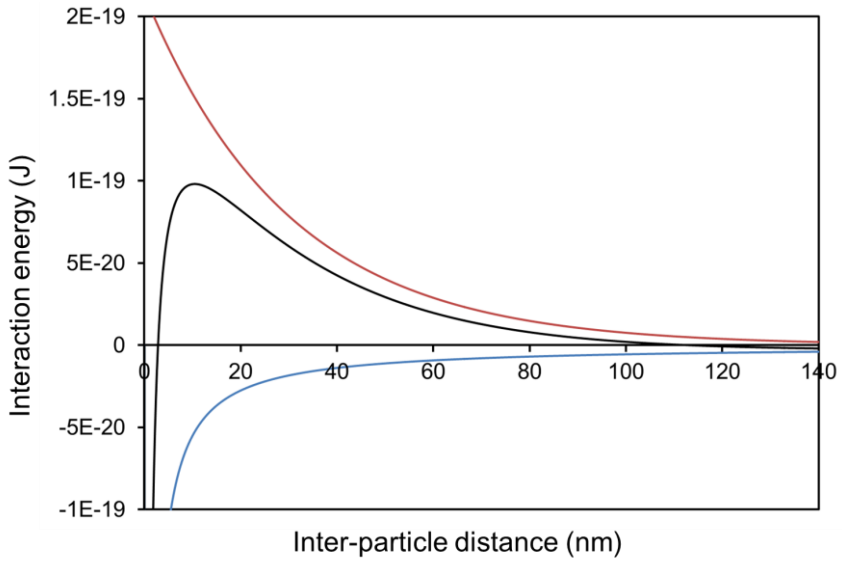

Fig. 4-8. Change in the DLVO potential. Blue line indicates van der Waals attraction and red line indicates electrostatic repulsive. Black line indicates a sum of these inter-particle interactions.

An energy barrier is observed at about 10nm in the DLVO potential curves, and the energy barrier prevents AuNPs from forming aggregations in aqueous solution. Therefore, a balance of the inter-particles interaction is very important for fabrication of highly-ordered 2DMAs.

4-4-3 Lateral capillary force

A lateral capillary force acts in the drying process of colloidal solution [94-95]. When a thickness of colloidal solution is comparable with a height of the nanoparticle, the lateral capillary force acts between the two particles and can be expressed in the following this formula.

$$F \approx -\frac{2\pi\gamma d^2}{L} \quad (r_i < L < q^{-1})$$

γ, d, L, r_i and q are the surface tension of the solution, the diameter of the particle, the interparticle distance, the radius of the particle contact line and the capillary constant, respectively. F is calculated to be approx. 4×10^{-8} N for the case of d = 100nm, L = 110nm, which is 5×10^{7} times larger than the force of gravity for the AuNP. Thus the capillary force is strong enough to work as the driving force for packing particles. Utilizing this force, Nagayama and co-workers successfully fabricated the 2D arrays of polymer particles and globular proteins (several μm) [68, 94, 95]. However, the capillary force cannot be used effectively for metal nanoparticles in the dried droplet method.

4-5 A guideline of fabrication of 2DMAs without any surface modifier

According to the DLVO theory, dispersion of metal nanoparticles in solution means that electrostatic repulsive force is stronger than van der Waals attractive force. Therefore, nanoparticles do not aggregate.

In order to fabricate a highly-ordered 2DMA, it is considered that a control of this inter-particle balance just before formation of 2DMA is very important. In other words, it is necessary that its fabrication condition is enough calm to keep the inter-particle

balance between the attractive force and the repulsive force. From this reason, a sudden change breaking this inter-particle balance such as a temperature change and an extreme density change should be excluded.

On the other hand, our group has developed a technique to enable fabrication of 2DMAs under the calm condition. The fabrication method is discussed in chapter 5 in detail.

Chapter 5

Fabrication of Two Dimensional Metal Nanoparticle Array

5-1 Introduction

According to past chapters, it is considered that a highly-ordered 2DMA composed by same gold nanoparticles (AuNPs) without any surface modifier is effective as a SERS active substrate with a high reproducibility and an ultra-high sensitivity. However, fabrication of the highly-ordered 2DMA is very difficult, because AuNPs easily aggregate by small physical change such as heat, concentration, purity and so on. These aggregations break uniformity of the highly-ordered 2DMA. In order to fabricate the highly-ordered 2DMA without any aggregations, these AuNPs should be maintained under a calm condition without any sudden change which breaks inter-particle balances.

To create this calm condition, our group covered the droplet by another flat plate. This reason is that this second plate is expected to decrease the evaporation rate of droplet and change a curvature of droplet near the edge which becomes fabrication point. And we succeeded in fabrication of a 2DMA. We called this method sandwich (SW) method [96]. However, the SW-method was not still optimized. In this chapter, the author tried to optimize conditions of the SW-method in order to fabricate

highly-ordered 2DMAs for more practical use.

5-2 Experimental

Aqueous solutions of AuNPs were used as received from BBInternational. The average diameters of the nanoparticles were 60 nm and 100 nm, with 8% standard deviation. No surfactant molecule or electrolyte was added in the solutions. Silicon wafers and glass plates of 1mm thickness were used as supporting substrates. Typical volume of a droplet and its contact area on the substrate were 400 μl and 4 cm^2, respectively. A second plate was used to cover the top of the drop, with a 1 mm thick spacer, as shown in Fig. 5-1. The AuNP colloidal solution in the sandwich configuration

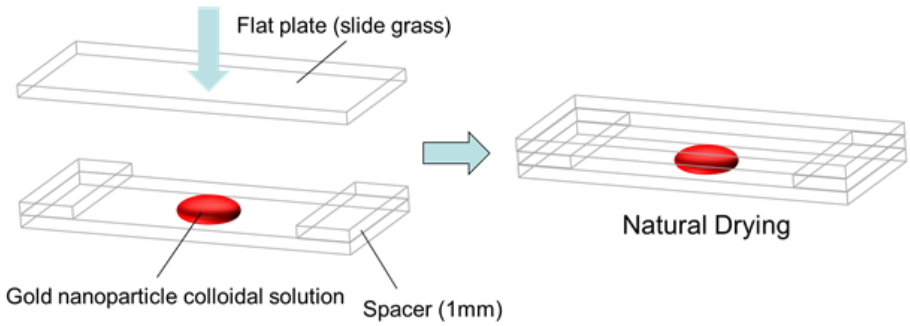

Fig. 5-1. Schematic illustration of experimental procedure in SW-method

was left at room temperature until the liquid was completely dried for more than 24 h. This experiment was performed at a temperature of 24 ± 2 °C and a humidity of 60 ± 10 %. Morphologies of each prepared 2DMAs were characterized by scanning electron microscopy (SEM; KEYENCE VK-9700). An acceleration voltage of 5 kV for glass

substrate and of 20 kV for silicon was employed.

5-3 Results and discussion

5-3-1 Early stage of sandwich method

First, the author tried to make a highly-ordered 2DMA which is composed by AuNPs with a diameter of 100 nm using the SW-method. A silicon wafer was used as a supporting substrate.

(a) (b)

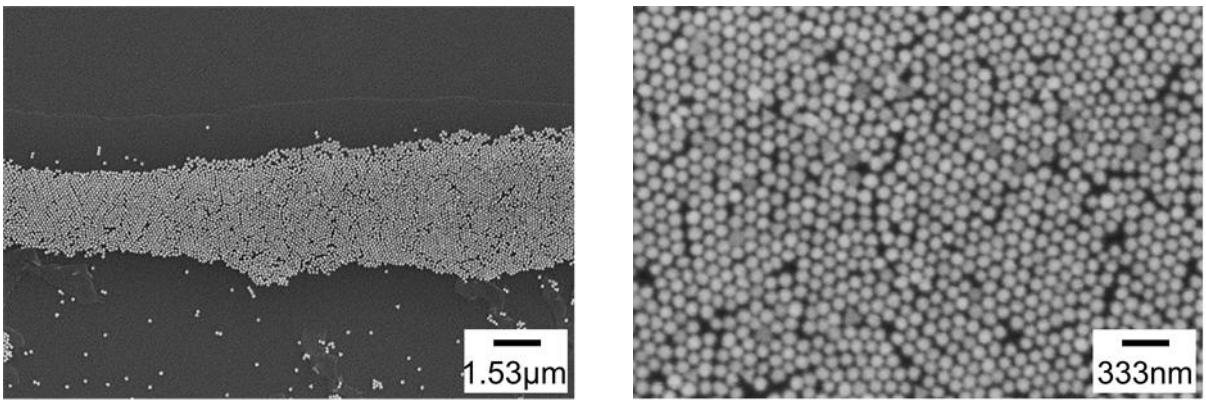

Fig. 5-2. SEM images of SW substrate which was composed by AuNPs with a size of 100nm before optimization of experimental condition;
(a) × 6500, (b) × 30000

A SEM image (× 6500) of a part of the SW-substrate was shown in Fig. 5-2 (a). In Fig. 5-2 (a), a belt-shaped structure which corresponds to assembly AuNPs was observed. A width of the belt-shaped structure was several micron meters. This belt-shaped structure was the largest domain in this experiment. In order to observe the belt-shaped structure

in detail, a SEM image (× 30000) was obtained as shown in Fig. 5-2 (b). An assembly of AuNPs with high particle density was observed, although some voids were observed in the assembly. Moreover, it seemed that multilayers and three dimensional aggregations of AuNPs were not observed in this image. Therefore, the author regarded the assembly of AuNPs as a 2DMA. However, an area of the 2DMA was too small to obtain many SERS spectra for quantitative analysis. Therefore, the author optimized experimental conditions of the SW-method in order to expansion area of the 2DMA.

5-3-2 Cleaning procedure of supporting substrate

First, the author paid attention to a SEM image which was obtained in the previous experiment in order to obtain a hint for optimization of the experimental conditions. A SEM image (× 25000) of characteristic point in SW-substrate was shown

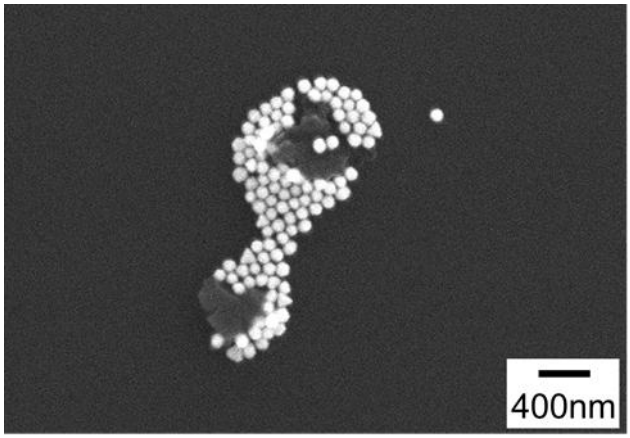

Fig. 5-3. A SEM image (× 25000) of characteristic point in the SW-substrate

in Fig. 5-3.

Two objects at a center of the image and AuNPs deposited around these objects were observed. On the other hand, there were almost no AuNPs around the block. This result might mean that discontinuous sites such as contaminants on a supporting substrate gathered AuNPs and disturbed fabrication process of the 2DMA. Namely, it is considered that these sites break the calm condition of AuNPs such as inter-particle balances between attractive force and repulsive force in fabrication process. A cleaning procedure of previous experiment was only washing with deionize water. The author thought that this procedure could not remove all contaminants on a supporting substrate completely. Therefore, this procedure should be improved.

Supporting substrate were washed three times per 15 min in acetone, methanol

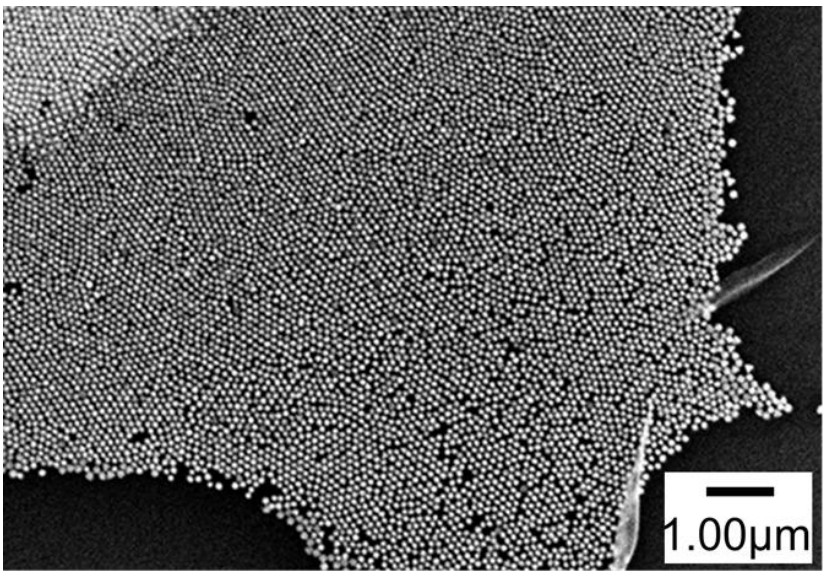

Fig. 5-4. SEM images (× 10000) of the SW-substrate which is composed by AuNPs with a size of 100 nm after cleaning procedure of supporting substrate.

and deionize water in ultrasonic bath. And then, a 2DMA is fabricated again by using SW-method after a new cleaning procedure. A SEM image of a 2DMA after the cleaning procedure was shown in Fig. 5-4. This experimental condition was same as the previous experiment except for cleaning of a supporting substrate. Approximately, an area of the 2DMA was several hundred μm^2. The area of the 2DMA was much larger than that of previous one. Therefore, it was considered that cleanliness on a supporting substrate was a critical factor in forming of 2DMA in the SW-method and contaminants on a supporting substrate should be removed.

5-3-3 Temperature dependence

In order to optimize experimental conditions in the SW-method additionally, the author examined under three temperatures (20 °C, 25 °C and 30°C) in a cabinet with a control system of temperature. These experiments were performed at humidity of 60 ± 10 %. In these experiments, AuNPs whose diameters were 60nm and glass plates as supporting substrates were used. SEM images of SW-substrates fabricated under these temperatures were showed in Fig. 5-5.

(a) 20°C

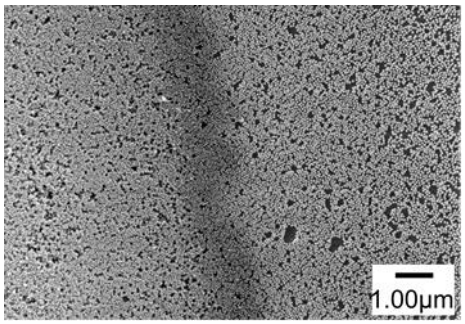

(b) 25°C

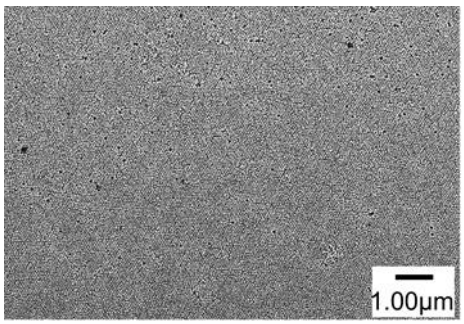

(c) 30°C

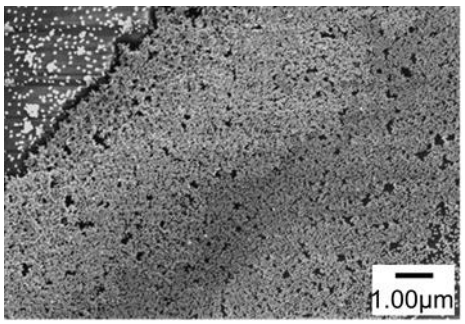

Fig. 5-5. SEM images (× 10000) of the SW-substrates which fabricated in three different temperatures; (a) 20°C, (b) 25°C, (c) 30°C

SEM image (× 10000) of the SW-substrate in 20 °C were shown in Fig. 5-5 (a). Highly-ordered 2DMAs was not observed in this condition. At center of this SEM image, a dark line was observed. In the left side of the dark line, multi-layers were observed. In contrast, in the right side of the dark line, mono-layer was observed. SEM image (× 10000) of the SW-substrate in 25 °C were shown in Fig. 5-5 (b). Highly-ordered 2DMAs was observed. AuNPs arranged orderly as with the case of AuNP with a diameter of 100 nm. A SEM image (× 10000) of SW substrate in 30 °C

was shown in Fig. 5-5 (c). Highly-ordered 2DMAs was not observed in this condition. Moreover, it appeared that the assembly of AuNPs became multi-layers and formed aggregations. This disarrangement of AuNPs might be caused by aggregations which are induced by intense Brownian motion in a high temperature. From these results, it is considered that a temperature of 25 °C is suitable for fabrication of 2DMAs. Moreover, it is considered that an experimental temperature affects formation of multilayer and aggregations of AuNPs.

5-3-4 Humidity dependence

Next the author examined under two conditions of humidity (20 ± 5 % and 60 ± 10 %), as shown in Fig. 5-6 (a), (b). These experiments were performed at temperature of 25 °C.

(a) (b)

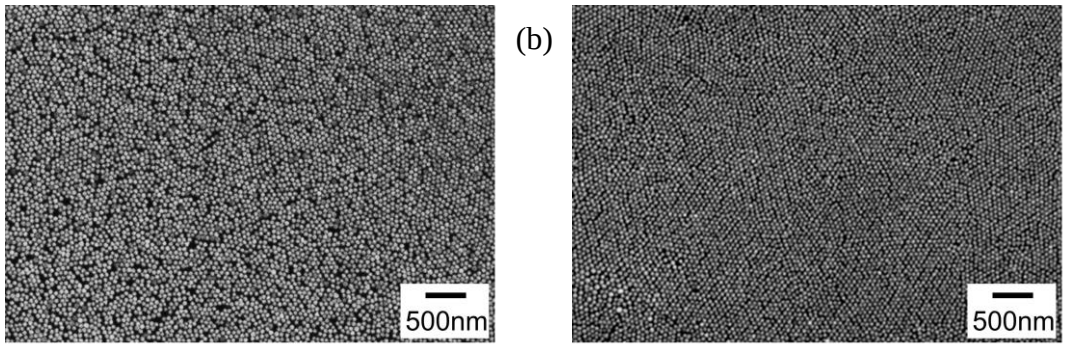

Fig. 5-6. SEM images (x20000) of SW-substrates which fabricated in two different conditions of humidity; (a) 20 ± 5 %, (b) 60 ± 10 %

Seemingly highly-ordered 2DMAs were observed in both substrates. However, particle density of SW-substrate fabricated in humidity of 20 ± 5 % was slightly smaller than that of SW-substrate fabricated in humidity of 60 ± 10 %. In order to clarify the difference of particle density in both SW-substrates, the author estimated packing rates of both SW-substrates by counting AuNPs per unit area. As a result, packing rate of SW-substrates fabricated in two different of humidity of 20 ± 5 % and 60 ± 10 % were 72% and 78%, respectively. The author considered that humidity in this experimental system mainly affected an evaporation rate of the droplet. Namely, it is suggested that packing rates of SW-substrates depend on evaporation rate of the droplet. From these results, it is considered that humidity of 60 ± 10 % is suitable for fabrication of 2DMAs.

5-3-4 Features of sandwich method

Features of the SW-method obtained from past experiments and previous studies by K. Shibamoto and co-workers [96] were described below.

1. The SW-method enables the fabrication of highly-ordered 2DMAs for wide range of nanoparticle size from 5 to 200 nm. [96]
2. Formation of the 2DMA in the SW-method is not likely to be associated with materials of supporting substrates. [96] However, surface cleanness of

supporting substrate is very important for forming large size of the 2DMA.

3. In order to fabricate highly-ordered 2DMAs, temperature of 25 ℃ and humidity of 60±10% are desirable for the experimental condition. Experimental temperature and humidity define a quality of 2DMAs.

In terms of fabrication of molecular sensors, the feature of 1 is important because fabrication cost is inexpensive. Moreover, reproducibility of fabrication of 2DMAs is very high because the arrangement of 2DMAs is defined unambiguously. The feature of 2 indicates that interactions between AuNPs and supporting substrates such as friction and epitaxial growth are not related to formation of the 2DMA in the SW-method. However, surface cleanness of supporting substrate is very important for forming large size of the 2DMA because contaminations on the supporting substrate break inter-particle balances in fabrication process. From the feature of 3, the author considered that a formation mechanism of the 2DMA is mainly based on evaporation rate of the droplet.

5-3-5 Predictable model of sandwich method

A difference of experimental procedure between the SW method and dried droplet method was only existence of second plate, but assemblies of AuNPs obtained by these methods were quite different. The author discussed what causes the difference.

It is considered that the second plate decreases an evaporation rate of the droplet, because gas-liquid interfacial area which specifies evaporation rate is decreased. Slow evaporation of the droplet may induce slow supply of AuNPs toward contact line, and this slow supply may not break inter-particle balances. Moreover, 2DMA was developed toward inside of droplet in evaporation process. This behavior of development may indicate a movement of the contact line. Moreover, the second plate decreases a contact angle of the droplet. Sharp contact angle may prevent piling up of AuNPs and pinning of the droplet. From these discussions, the author thought a predictable model near the contact line of the SW-method, as shown in Fig. 5-7.

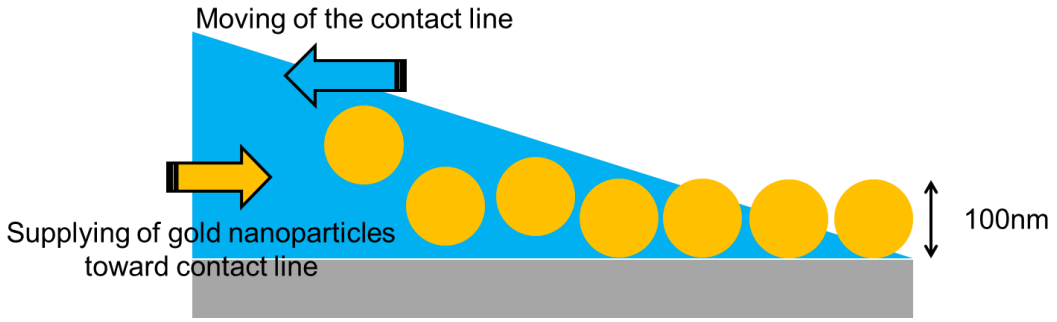

Fig. 5-7. Scheme of predictable model of sandwich method.
In this model, AuNPs are supplied toward a sharp
contact line and deposited on a supporting substrate gently.

The author considered that supplying AuNPs toward the contact line and moving the contact line are dominant process in the SW method. A balance of these processes may determine a quality of 2DMA. For example, when the movement rate of contact line is slower than supply rate of AuNPs, it is considered that a concentration near the contact line reaches oversaturation as shown in Fig. 5-8. Therefore, experimental temperature and humidity are important for formation of the 2DMA.

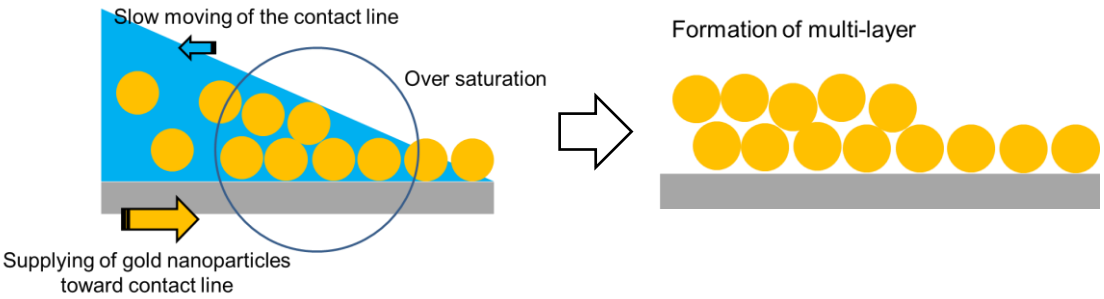

Fig. 5-8. Scheme of predictable mechanism of formation of multi-layer. Relative slow moving of the contact line may induce saturation of AuNPs near contact line.

5-4 Conclusions

The author demonstrated the SW method and tried to optimize experimental conditions of the SW method in order to expand area of the 2DMA. In the SW method, removal of contaminant on supporting substrate is important for formation of 2DMA. Therefore, we improved the cleaning procedure of supporting substrates. As a result, the author succeeded in fabrication of 2DMAs by using SW method. Moreover, the author

examined a dependency of temperature on arrangement of AuNPs. And, it is considered that a temperature of 25°C is suitable for fabrication of 2DMAs. Further research for uniformity of 2DMA and mechanism of the SW-method were discussed in chapter 6.

Chapter 6

Evaluation of 2DMAs with spectroscopy and Chase of the Assembly Process

6-1 Introduction

In chapter 5, our group has developed a very simple technique that everyone can fabricate 2DMAs of bare AuNPs only by sandwiching the gold colloidal solution between two flat plates and drying naturally. As far as SEM images are concerned, the author verified that an arrangement of our 2DMAs seems to have a higher uniformity than that of conventional 2DMAs qualitatively. However, the author has not discussed the uniformity of the 2DMAs such as an aggregation condition, an inter-particle distance and a periodicity in detail. In this chapter, the author combined the SEM analysis with spectroscopic analysis in order to discuss the uniformity of the 2DMAs in detail.

Furthermore, the assembly mechanism of SW method was not yet clear. However, in order to expand an area of the fabricated 2DMAs by this SW method, more understanding for the assembly mechanism is required. In the latter half of this chapter, the author discussed the assembly mechanism of SW method by evaluating its uniformity of SW-substrates fabricated by the SW method shown in the first half of this

chapter.

6-2 Experimental

Aqueous solution of gold spherical nanoparticles (diameter : 60 nm, density : 2.6×10^{10} particles/ml) with narrow size distribution was purchased from BBInternational. Glass plates of 1mm thickness and 76 mm × 26 mm size were used as substrates. These plates were rinsed several times in acetone, methanol, and deionized water in an ultrasonic bath. After dropping the gold colloidal solution onto a plate, the author placed a second plate covering top of the droplet with a distance of 1 mm from the first plate. Droplet volume on the substrate was 100 μl. The droplet was left until the solution was completely evaporated up to about 2 days. The author called the obtained 2DMAs sandwich (SW) substrates. A series of these experiments were performed at a temperature of 24 ± 2 °C and a humidity of 60 ± 10 %. For comparison, the author prepared two other 2DMAs substrates, which were formed by oil-water trapping method (OW) and dried droplet method (DD). In the OW method, 5ml of AuNP colloidal solution was transferred to a vial, and 5 ml of cyclohexane was added to the colloidal solution in order to form an interface between cyclohexane and water. After forming the interface, 5 ml of methanol was injected into the vial vigorously, and then

AuNPs were trapped at the interface layer. AuNPs trapped at the interface formed 2DMAs. In DD method, 400μl of AuNP colloidal solution was dropped onto a slide glass, and then the droplet was dried naturally. Octave 3.6.4 was employed for Fourier transform analysis of the SEM images of all fabricated substrates.

6-2-1 Construction of Vis-near IR microspectometer

The author constructed a Vis-near IR microspectrometer. A halogen lamp was employed as a light source in the system. The halogen lamp was collimated by three convex lenses (f=1000 mm, 70 mm, 50 mm) and two pinholes. The collimated light focused on prepared 2DMAs substrates by a convex (f=50 mm). The transmitted light was guided into a detector by using a mirrors and a convex lens. The focal spot diameter confirmed by optical microscope was about 100μm. Absorption spectra of 2DMAs substrates were obtained by a spectrometer (StellarNet Inc.) connected to the detector. The absorption spectra were acquired by accumulating 50 spectra with 0.3 seconds integration time each.

6-3 Results and Discussion

6-3-1 Evaluation of uniformity of 2DMAs by using SEM

A SEM image (× 50) of SW-substrate composed by AuNPs was shown in Fig. 6-1 (a). White area in Fig. 6-1(a), which corresponds to assembly of AuNPs, had a step-by-step structure. A width of the white line area was up to 150 μm. In order to confirm morphology in the white area in detail, a SEM image (× 20000) in the white area was shown in Fig. 6-1 (b).

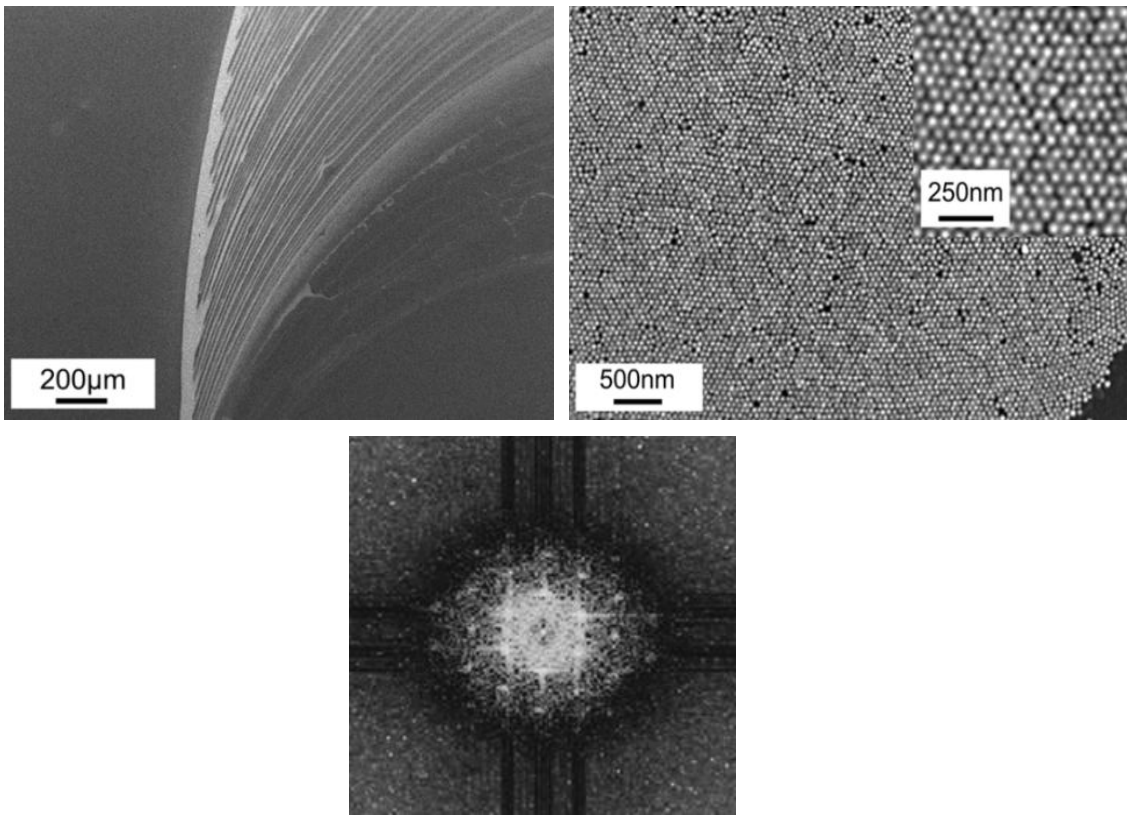

Fig. 6-1. SEM image of the 2DMA composed by gold nanoparticles (diameter: 60 nm) formed by SW method; (a) at ×50 magnification (b) at ×20000 magnification (c) image of Fourier transform

AuNPs were arranged orderly in all of the area. A SEM image (× 20000) of OW-substrate was shown in Fig. 6-2 (a). 2DMAs in OW-substrate seemed disorderly and included large voids, compared with 2DMAs in SW-substrate. A SEM image (× 20000) of DD-substrate was shown in Fig. 6-2 (b).

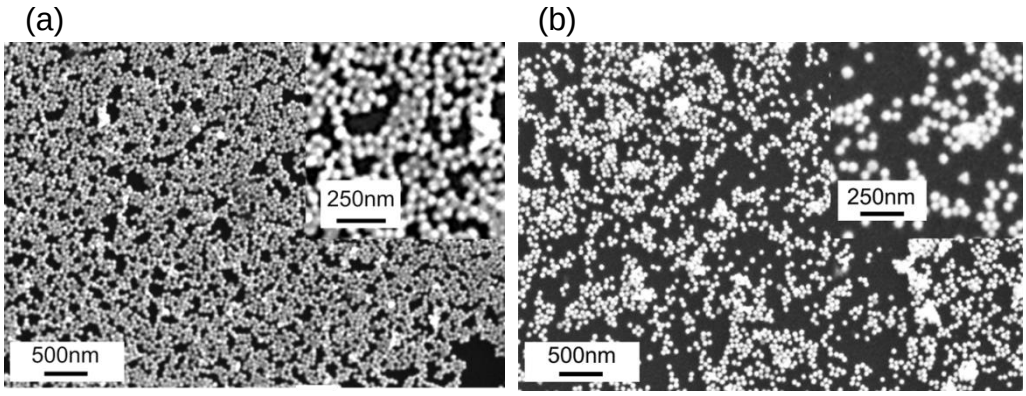

Fig. 6-2. SEM image of 2DMAs composed by gold nanoparticles (diameter: 60 nm); (a) OW substrate (b) DD substrate

DD-substrate had no 2DMAs structure but included small amount of large aggregations. The DD-substrate had the lowest density of AuNPs in three substrates. For estimation of a uniformity of these 2DMAs, these SEM images were divided into a division with a size of 500 nm×500 nm, and packing rates at each division were counted. Average packing rates and its relative standard deviations (RSD) of these substrates are shown in Table 6-1.

Method	Average packing rate	RSD (%)
Sandwich	78%	4.3%
Oil-water interface trapping	65%	10%
Dried droplet	29%	33%

Table. 6-1.Average packing rates and relative standard deviations of three types of substrates.

Packing rates of these substrates (SW-substrate, OW-substrate and DD-substrate) were 78%, 65% and 29%. And, their RSDs were 4.3%, 10% and 33%. An image which visualized packing rate is shown in Fig. 6-3.

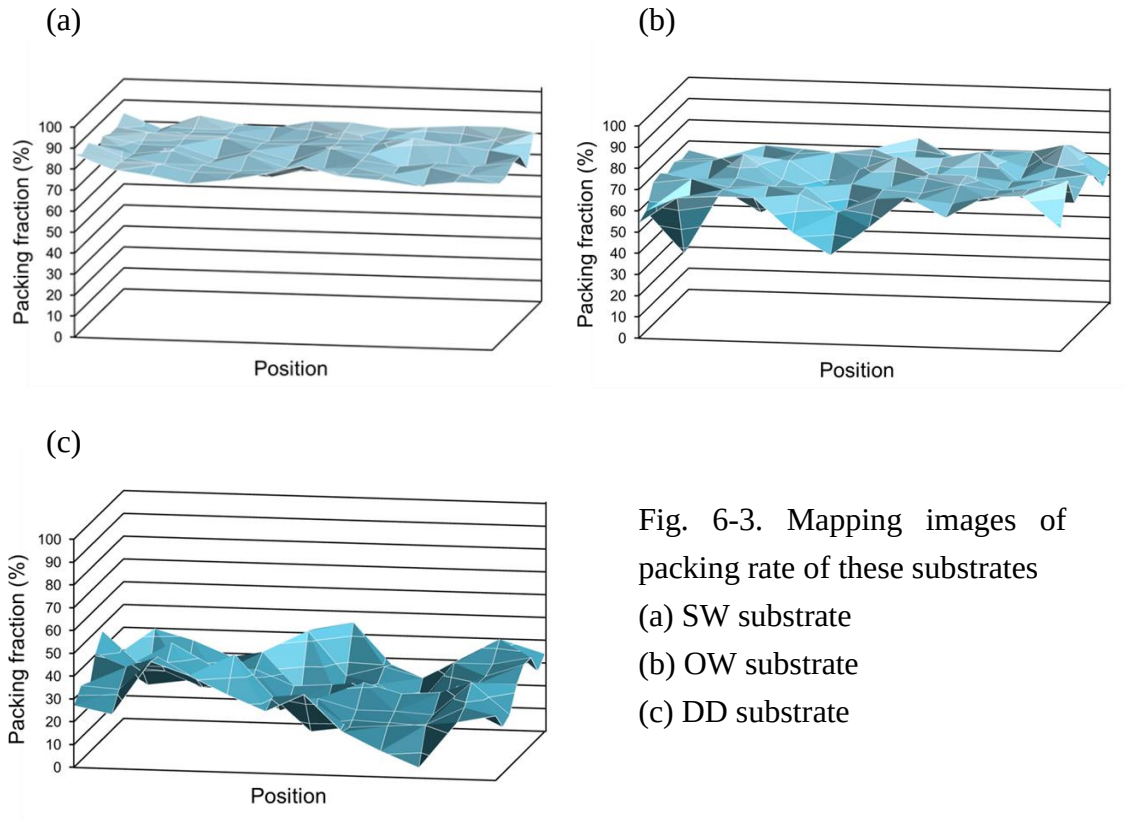

Fig. 6-3. Mapping images of packing rate of these substrates
(a) SW substrate
(b) OW substrate
(c) DD substrate

The SW-substrate had a higher packing rate and smaller RSD of packing rate than other substrates. This result means that SW-substrate has a higher uniformity than other substrates. Next, for evaluation of their periodicity and inter-particle distance, the author attempted Fourier transform analysis of these SEM images of all substrates. As a result, a pattern of Fourier transform of SW-substrate was obtained as shown in Fig. 6-1 (c), and clear points in this pattern formed a hexagonal array, although any clear points were not found from Fourier transform images of other substrates. This hexagonal array means a hexagonal periodic structure of 2DMAs in SW-substrate and other substrates don’t have any periodic structure. However, the packing rate of SW-substrate was smaller than 2D closest packing rate of 91 %, although our 2DMAs has 2D a largest packing rate. The hexagonal lattice constant of the SW was 64.5 nm. In consideration of the hexagonal lattice constant of 64.5 nm, 2D closest packing rate was recalculated to be 81%. This value is good approximation of 78 % which is the packing rate of SW-substrate. These results indicate that 2DMAs in SW have inter-particle gaps. An average gap of inter-particle was estimated at 4.5 nm.

6-3-2 Spectroscopic analysis of 2DMAs

Visible-near infrared absorption spectra of these 2DMAs are shown in Fig. 6-4.

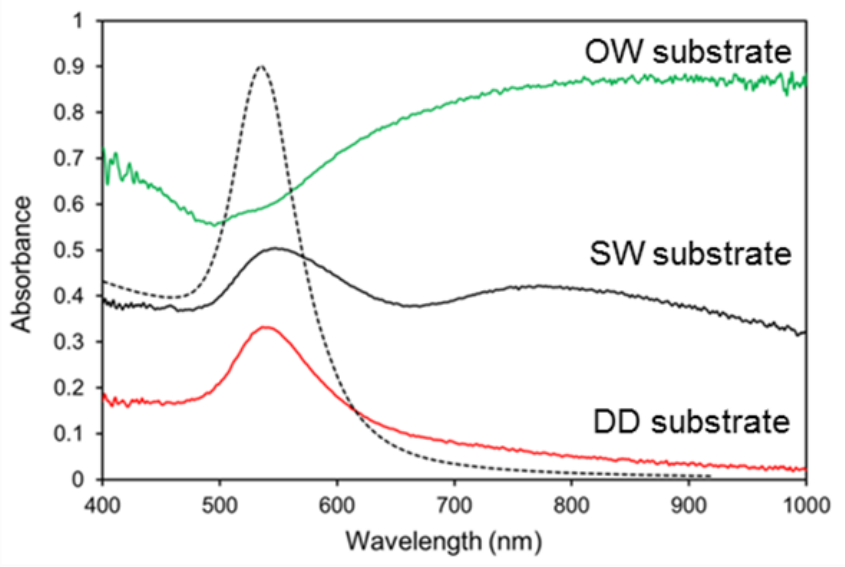

Fig. 6-4. Absorption spectra of 2DMAs composed by AuNPs (diameter: 60 nm); black line: SW substrate, green line: OW substrate, Red line: DD substrate, dotted line: AuNP aqueous solution

An absorption spectrum of SW-substrate had two major peaks at 547 nm and about 750 nm. An absorption spectrum of OW-substrate had a broad peak in the wavelength region from 600 nm to 1000 nm, and that of DD-substrate had a single peak at 540 nm. It is well-known that an absorption spectrum of isolated gold nanospheres in water has a single peak at 537 nm, which corresponds to the LSPR of a gold nanosphere. Therefore, the peak of the SW-substrate at 547 nm and the peak of the DD-substrate at 540 nm can be interpreted as an LSPR peak of isolated gold nanosphere, although these

peaks were slightly red-shifted from the peak of isolated gold nanospheres at 537 nm due to existence of neighbor nanoparticles. When AuNPs aggregate on a plate, it is known that the substrate has a lot of aggregations with various size and shape and then has not the LSPR absorption of an isolated AuNP but a new broad peak at longer wavelength region [97]. Therefore, the LSPR peak of SW-substrate indicates that almost of AuNPs in 2DMAs don't contact directly. On the other hand, the LSPR band in the spectrum of OW-substrate was almost disappeared or hidden in background signals, although a broad peak in the wavelength region from 600 nm to 1000 nm was observed. This result indicates that OW-substrate is composed by random aggregations of AuNPs, because its disordered arrangement generates various plasmon modes in the same wavelength region due to various inter-particle distances or various sizes of aggregates and their complex generates a broad peak in longer wavelength region. In contrast, not only a peak at 547 nm but also other peak at 750 nm was clearly observed in the spectrum of SW-substrate. It is reported that a peak appears in a much longer wavelength region than 537 nm and its position depends on a distance of inter-particle gap when a few AuNPs come close each other. Therefore, the author interpreted this peak at 750 nm in the spectrum of SW-substrate as a coupling of the LSPR between neighboring AuNPs with inter-particle gap of several nm. Moreover, because this

sharpness of this peak at longer wavelength region suggests smallness of distribution of the gap distance, it is considered that our 2DMAs has a constant distance of inter-particle gap. In this stage, the author can't estimate a precise distance of this gap from the absorption spectrum because many AuNPs may interact each other in this 2DMAs arrangement, although this gap at 4.5 nm was estimated from the result of Fourier transform analysis.

6-3-3 Assembly process of the 2DMAs and its considerable mechanisms in the SW method

An optical microscope image of lateral meniscus which was formed by the SW-method was shown in Fig. 6-5.

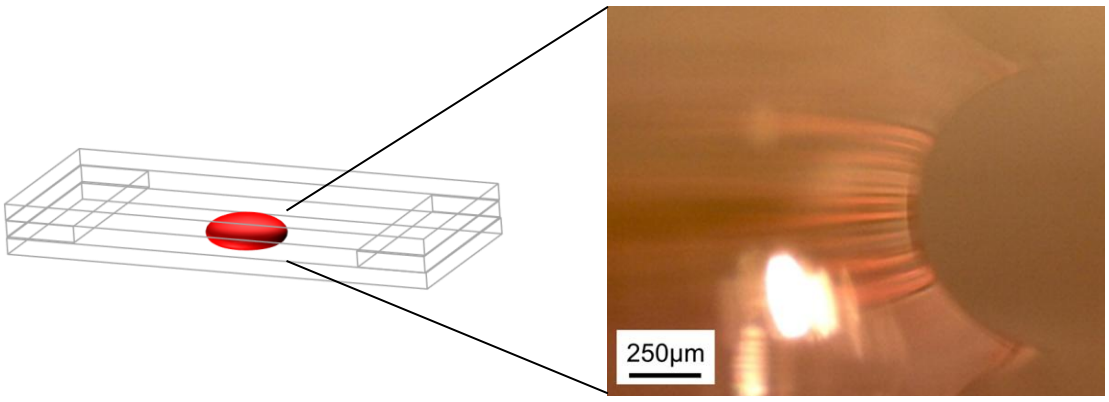

Fig. 6-5. A lateral image of meniscus of a droplet in SW method.

The meniscus had a half moon shape and sharp contact angle, which was different from a simple droplet on flat plate. Fig. 6-6 showed an optical microscope image at a contact line of the meniscus every 15 minute in initial evaporation process.

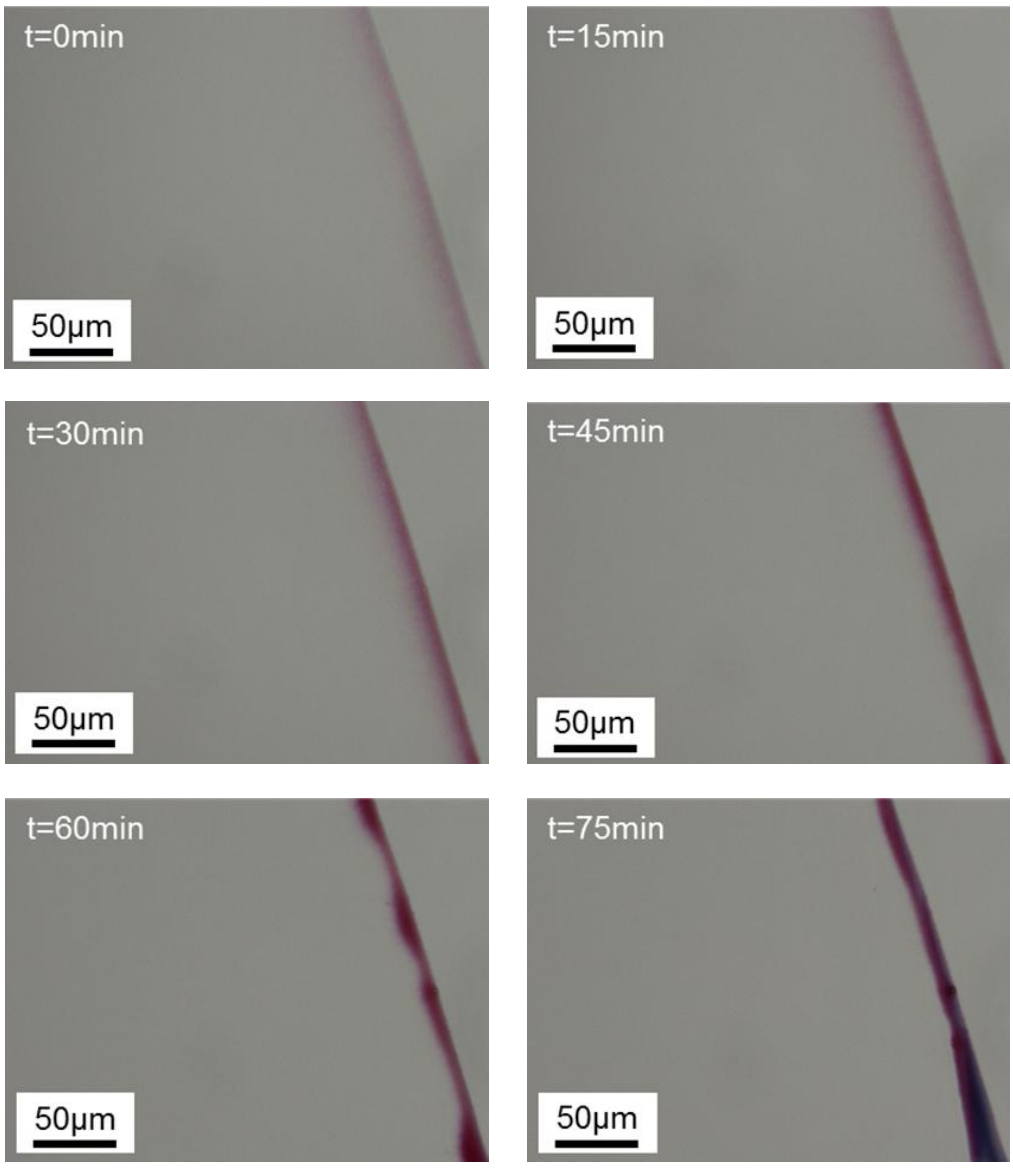

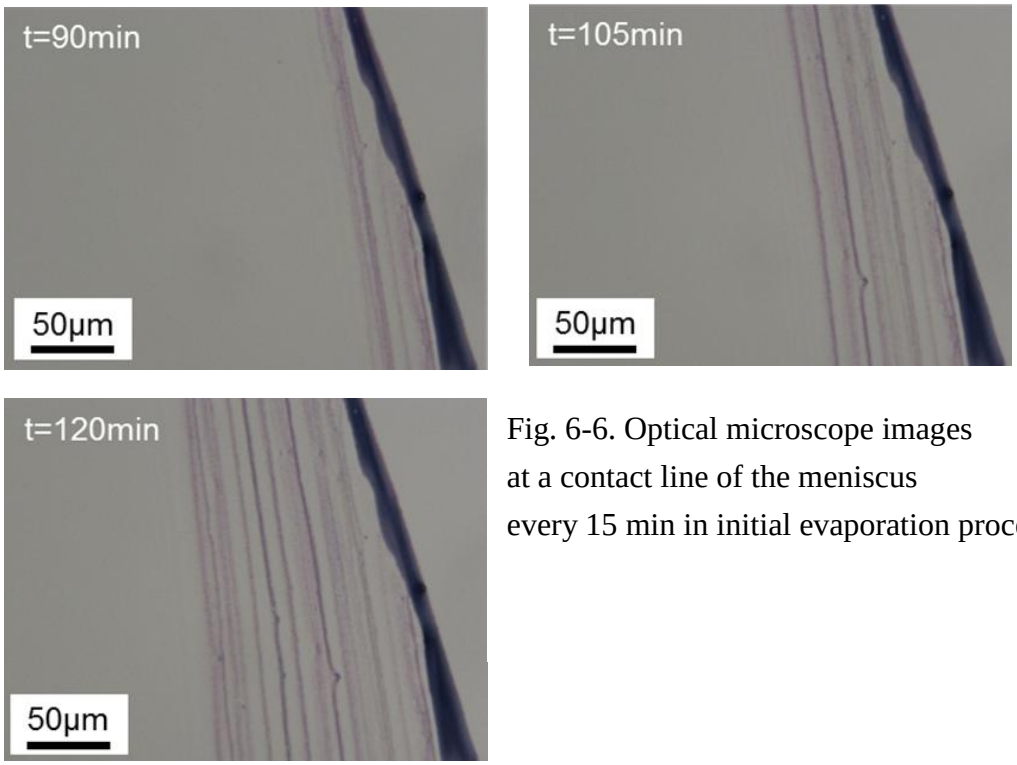

Fig. 6-6. Optical microscope images
at a contact line of the meniscus
every 15 min in initial evaporation process

In the optical microscope image at t=0 min, the contact line had a red color. This color of contact line became darker with time until t=75 min. In optical microscope images from t=60 min to t=90 min, this dark red area became large. In optical microscope images from t=45 min to t=75 min, the color of contact line became deep purple from red. Because this color change was not clearly observed by transmission optical microscope, the auhor observed the contact line at t=45 min with a reflection microscope, as shown in Fig. 6-7.

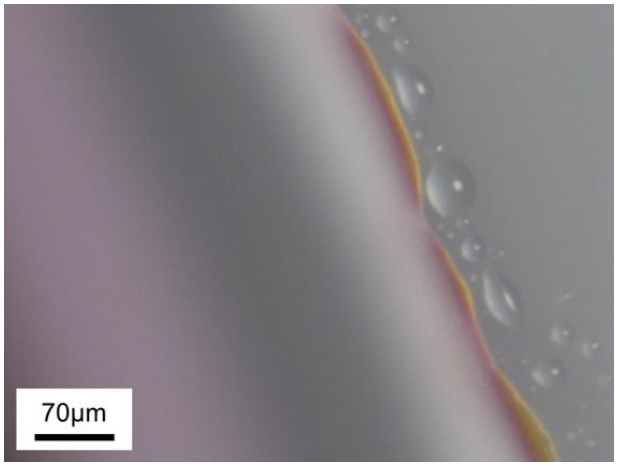

Fig. 6-7. Reflection microscope of the contact line at t=45 min

At an edge of the contact line, a structure which had color gradation from red to gold was clearly observed. In an optical microscope image at t=90 min, step-by-step structures were observed, and then the area of structures were increased from t=90 min to t=120 min.

In an early stage of observation (t=0~45 min), the red color of the contact line corresponded to LSPR absorption of isolated AuNPs in water solution. It is considered that becoming darker in red at the contact line corresponds to an increase in concentration of AuNP colloidal solution. In this case, AuNPs were concentrated in a small region of the contact line, although solute should be diffused uniformly to become stabilize thermodynamically. This non-equilibrium situation may indicate a presence of a convective flow toward the contact line. A gold area of gradation structure which is

observed in Fig. 6-7 had a 2DMAs arrangement of AuNPs. This means that 2DMAs were formed at only an edge of the contact line. Remarkable point was that a color changes in this structure from red to gold smoothly without a color change to black because aggregations of AuNPs have a black color. In other word, this color change indicates that AuNPs maintained isolated state until 2DMAs were formed. It is considered that maintaining the isolated state of AuNPs was one of reasons why SW-method can form high ordered 2DMAs without any aggregations. The author thinks that inter-particle distance, which was average 4.5 nm, may relate to a potential barrier which is caused by sum of van der Waals attractive force and electrostatic repulsive force by electric double layer between nanoparticles in the 2DMAs.

The Step-by-step structures which were observed from t=90 min to t=120 min indicated a movement of the contact line toward inside, because 2DMAs were formed at only an edge of the contact line. This movement toward inside was smooth according to the observation of optical microscope images. Generally, a contact line of simple droplet on flat plate is pinned and then almost keeps initial position until complete evaporation of solvent. One of the reasons was considered that the shape change of droplet, which was decrease of height of droplet, has a priority to the movement of the contact line. On the other hand, the contact line in SW method was almost not pinned except early stage

of observation (t=0~45 min). the author thought that the reason why the pinning effect is resolved is because the shape change of the half-moon like meniscus, which is stabilized in capillary bridge, has a priority to the movement of the contact line toward inside. This smooth movement of the contact line may contribute to formation of highly ordered 2DMAs, because the movement of the contact line prevented AuNPs from supplying toward the contact line in large excess. From these discussions, the author thought that SW method has three important factors.

1. Supplying AuNPs toward the contact line along a convective flow

2. Maintaining dispersive nature just before formation of 2DMAs

3. Smooth movement of the contact line toward inside

These factors were described as shown in Fig. 6-8. The reason why step-by-step structures were formed might be caused by disbalance between supplying rate of AuNPs and regression rate of the contact line. Therefore, it may be important for area expansion of highly-ordered 2DMA to ensure a proper balance of these rates, because step-by-step structures become one large domain.

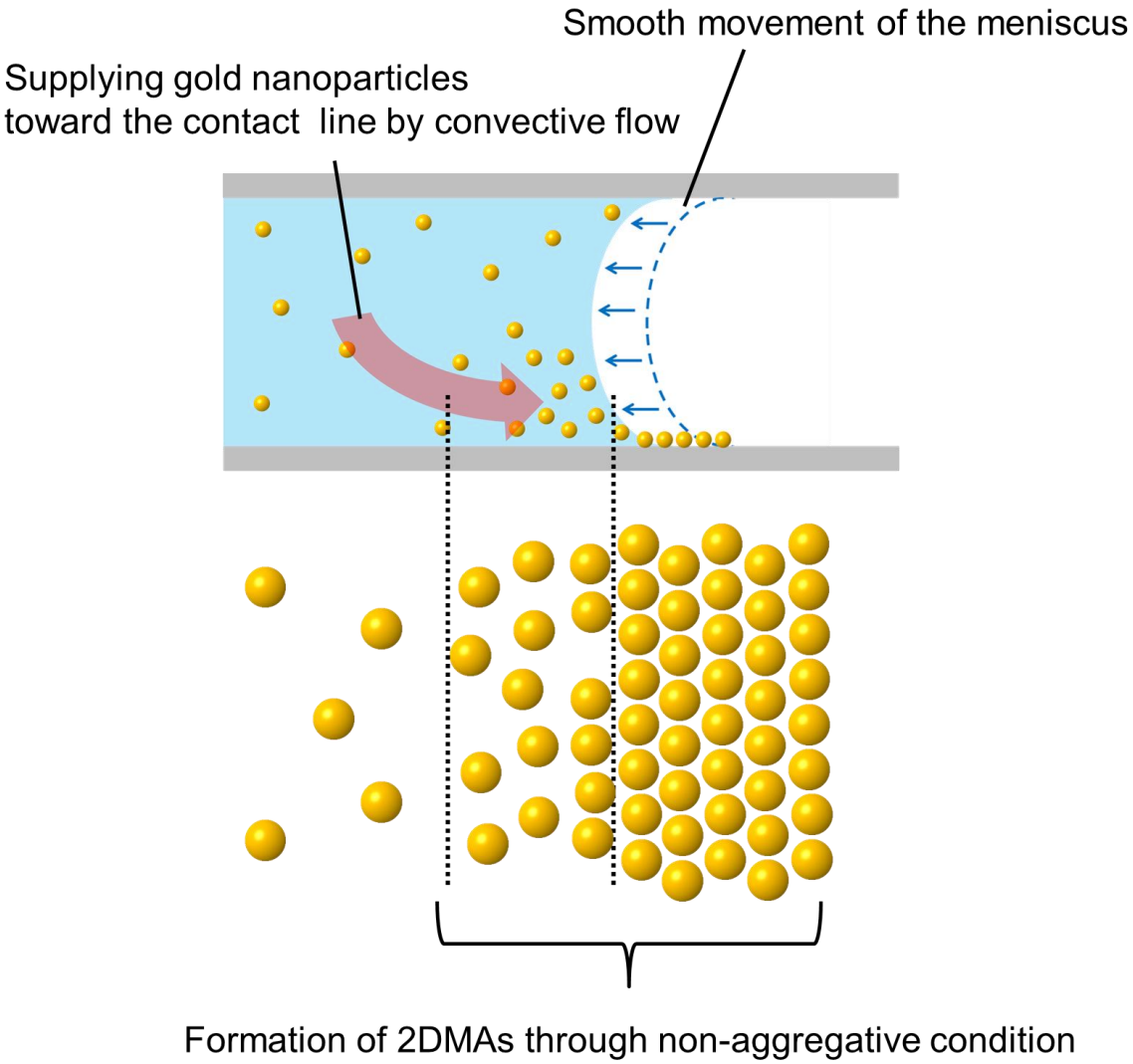

Fig. 6-8. Schematic illustration of considerable mechanisms in the SW method

6-4 Conclusions

The author has discussed a uniformity of the 2DMAs without any surface modifier by using SEM observation and spectroscopic analysis. SEM analysis with Fourier Transform analysis showed that our 2DMAs have a high uniformity and a hexagonal periodicity in the arrangement and also the 2DMAs have inter-particle gaps of average 4.5 nm, although SEM analysis lacks sufficient evidence. On the other hand, spectroscopic analysis showed that AuNPs in our 2DMAs exist in the neighborhood of less than several nanometers but not contact each other. From these results, it is considered that our 2DMAs have a high uniformity and a constant inter-particle distance which has a large potential to generate a giant enhancement effect.

Moreover, the author has discussed the assembly mechanism of SW method by the information about an uniformity of SW-substrate obtained in the first half of this chapter and observations of assembly process with an optical microscope. The color changes of the contact line indicated existence of a convective flow toward the contact line, and the flow transferred AuNPs from solution to the edge of contact line. As a result, concentration of AuNPs at the contact line was increased. However, AuNPs did not aggregate at the contact line. It was considered that these AuNPs maintained a dispersive nature just before forming of the 2DMA. Moreover, contact line can move

smoothly with drying of the droplet in SW method, although commonly a contact line of deposited droplet did not move by a pinning effect. This movement may prevent AuNPs from supplying toward the contact line in a large excess. From these processes, it is considered that SW-method can fabricate highly-ordered 2DMA.

Chapter 7

Surface Enhanced Raman Scattering Detection with Highly-Ordered Gold Nanoparticle Array

7-1 Introduction

Surface Enhanced Raman Scattering (SERS) is an attractive tool for ultratrace analysis of sample molecules due to its huge enhancement effect caused by surface plasmon (SP) resonance on nano-structured surface. However, the enhancement effect strongly depends on morphology of the nano-structured surface. Therefore, in order to control the enhancement effect, the nanostructured surface should be consisted of same metal nanosphere as a two dimensional metal nanoparticle array (2DMA) because its efficiency of SP resonance strongly depends on metallic species, shape, size, inter-particle distance and arrangement. In this stage, there are many reports for the fabrication method but there still remains as a big issue to fabricate nanostructured surface which enables to control the enhancement effect. In order to solve this problem and apply for a bio-sensor, uniform arrangement of bare metal nanoparticles such as an ordered 2DMA is required. However, there is almost no report for fabrication of the highly-ordered 2D metal nanoparticle array.

On the other hand, as showed in previous chapters, we have succeeded in

forming of 2DMA of AuNPs by using a sandwich method. In this chapter, we evaluated its uniformity of the arrangement in the 2DMA and spot-to-spot reproducibility of SERS signals, and discussed a relationship between the uniformity of arrangement and the reproducibility of SERS signals.

7-2 Experimental

The author used colloidal aqueous solution of AuNPs, whose diameter is 60 nm with narrow size distribution. The colloidal solution was purchased from British Biocell International (BBI). The concentrations of the AuNPs aqueous solution were 2.6 $\times 10^{10}$ particles/mL. Crystal violet, which was purchased from Sigma-Aldrich, was used as a sample molecule to examine its SERS activity. Methanol (99 %) and cyclohexane (99 %) were purchased from Wako. The author selected three type methods involving our method for fabricating 2DMAs in order to compare their packing condition of these 2DMAs substrates. All 2DMAs were constructed onto an n-type (100) Si wafers (Nilaco) and slide glasses as supporting substrates. These substrates were washed in ultrasonic bath along with deionized water for 15min and then washed with methanol. A series of these experiments were performed at a temperature of 24 ± 2 °C and a humidity of 60 ± 10 %. Morphologies of all prepared 2DMAs were characterized by

scanning electron microscopy (SEM; KEYENCE VK-9700) with an acceleration voltage of 20 kV.

7-2-1 Preparation of SERS active substrates

Sandwich-method (SW-method)

AuNPs solution was dropped onto the supporting substrate. After dropping the solution, we placed another substrate covering the top of the droplet with the distance of 1mm from the first supporting substrate. Volume of a droplet and its contact area on both substrates are 100 μl and 1 cm^2, respectively. The AuNP colloidal solution in the sandwich configuration was left at room temperature until the liquid was completely dried for more than 24 h.

Dried droplet method (DD-method)

AuNP solution was dropped onto the supporting substrate (Si single crystal). And then, the droplet was left at room temperature until the liquid was completely dried for about 1 h.

Oil-water interface trapping method (OW-method)

5ml of AuNP colloidal solution was transferred to a vial, and then 5 ml of cyclohexane was added to the colloidal solution in order to form an interface between

cyclohexane phase and water phase. After forming the interface, 5 ml of methanol was injected into the vial vigorously, and then AuNPs were trapped and formed 2DMAs at the interface layer. The 2DMAs trapped at the interface was put to the supporting substrate by removing both solvent.

7-2-2 Construction of optical system for detection of Raman scattered light

The author constructed an optical system for detection of Raman scattered light, as shown in Fig. 7-1. 532 nm lines of Nd:YAG laser was employed as an excitation laser source and its laser power was about 40mW, because the wavelength can match the LSPR of AuNPs. The laser line was collimated by a pair of convex (f=100 mm) and concave (f=50 mm) lenses. After the collimation, the laser line was passed a band pass filter in order to cut wavelength region not involving 532 nm, because the initial laser wavelength range was wide. The laser line was split half-half and one was curved to a right side by cubic beam splitter, the other was not used for this optical system. Prepared samples on 2DMAs substrates (sample preparation process was described next section) were irradiated by the laser line after passing through a 20 × objective lens, and then Raman light scattered from the sample was collected with the same objective lens. The

precise position of the objective lens was aligned by confirming the profile of repassed light through the objective lens. When the objective lens position is set in a proper position, the profile of repassed light becomes congruent with the initial profile of laser source. The laser power at sample position was about 5mW and its laser focal spot was ca. 10 μm^2. The repassed Raman light was passed cubic beam splitter again and then two filter of a notch filter and a high-pass filter cut Rayleigh scattered light. In this stage, passed light consisted of only Raman scattered light and then was guided into a detector in a black box by using a mirror and a convex lens. Raman spectra were obtained by a -15 ℃ air-cooled spectrometer (HAMAMATSU PHOTONIC Inc.) connected to the detector. The spectra were acquired by accumulating five spectra with 10 seconds integration time each. Moreover, these experiments were done under dark-room environment in order to reduce noises.

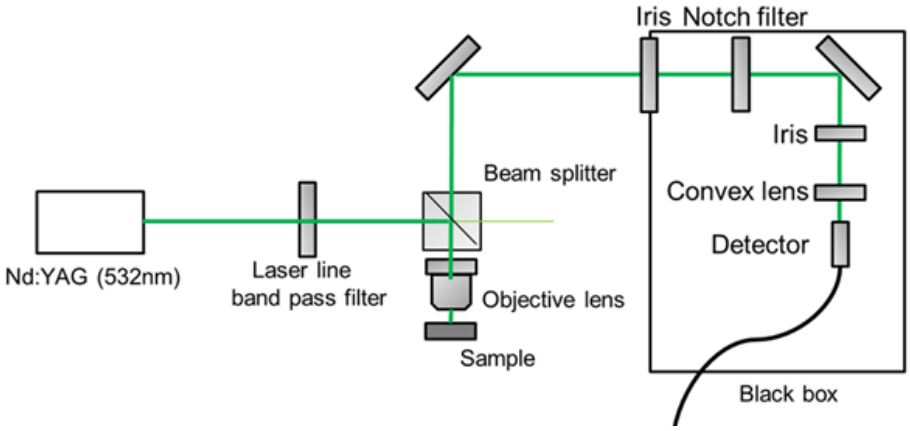

Fig. 7-1. Constructed optical system for detection of Raman scattered light

7-2-3 Sample molecule

Crystal violet (CV) molecule was employed as a sample molecule of SERS measurement. CV is often used in SERS studies [98]. A molecular formula and absorption spectrum of CV in aqueous solution were shown in Fig. 7-2. The CV molecule has a structure with a carbon in the center and three benzene rings at each apex of a triangle.

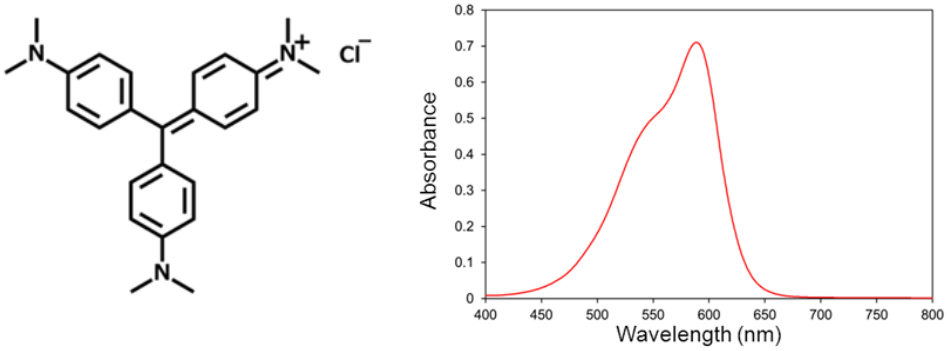

Fig. 7-2. Molecular structure of crystal violet and absorption spectrum of crystal violet aqueous solution

7-2-4 Adsorption to SERS active substrates of crystal violet

These SERS active substrates were dipped in the 10^{-5} M CV aqueous solution for several minutes in order to adsorb CV molecules. After dipping them in the 10^{-5} M CV aqueous solution, these SERS active substrate were washed by pure water in order to remove impurities and non-adsorbed CV molecules, as shown Fig. 7-3. The amount of adsorbed CV was determined by estimating the surface area of the AuNP and the

average adsorption area of each CV molecule. The CV molecule has a structure with a carbon in the center and three benzene rings at each apex of a triangle. Therefore, the author assumed that the number densities of adsorbed molecules per unit area were almost equal for every sample and were estimated at 1.3×10^{14} molecules/cm^2.

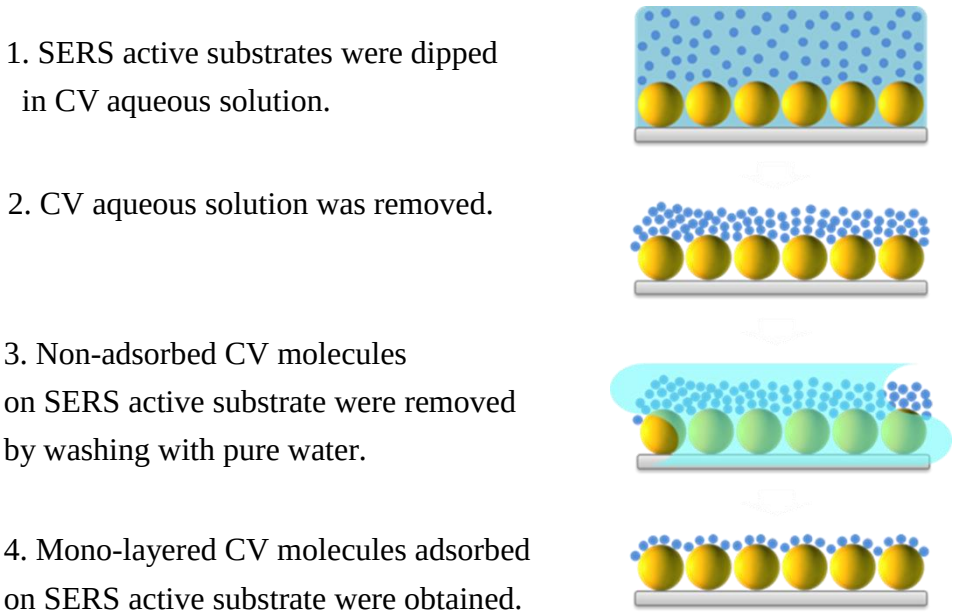

Fig. 7-3. Schematic illustrations of a procedure for adsorption to SERS active substrates of crystal violet

7-3 Results and Discussion

7-3-1 SERS active substrates

A SEM image (× 20000) of a substrate fabricated by the SW-method (SW-substrate 1) was shown in Fig. 7-4 (a). AuNPs were arranged orderly in all of the area, although the substrate included some voids. SW-substrate 1 had almost no aggregations of AuNPs and had gaps with an inter-particle distance of sub-10 nm. Moreover, the author prepared one more substrate fabricated by the SW-method (SW-substrate 2), although the experiment was performed at a humidity of 20 ± 5 %. According to our previous work, uniformity of an arrangement in a SW-substrate strongly depends on an evaporation rate of AuNPs aqueous solution. Therefore, the author expected that the SW-substrate 2 has a difference in arrangement of 2DMA in detail. A SEM image (× 20000) of SW-substrate 2 was shown in Fig. 7-4 (b). In Fig. 7-4 (b), it seems that the SW-substrate 2 is composed by small structures which consist of several AuNPs and have much more voids than SW-substrate 1. SEM images of substrates fabricated by the OW-method and the DD-method with same magnification ratio and images of their Fourier transform were shown in Fig. 7-4 (c) and (d), respectively. AuNPs in the OW-substrate seemed to be arranged disorderly and this substrate included more voids and a lot of aggregations of AuNPs than SW-substrates.

The DD-substrate had the lowest density of AuNPs among four substrates. The DD-substrate was composed by some isolated AuNPs and a lot of aggregations of

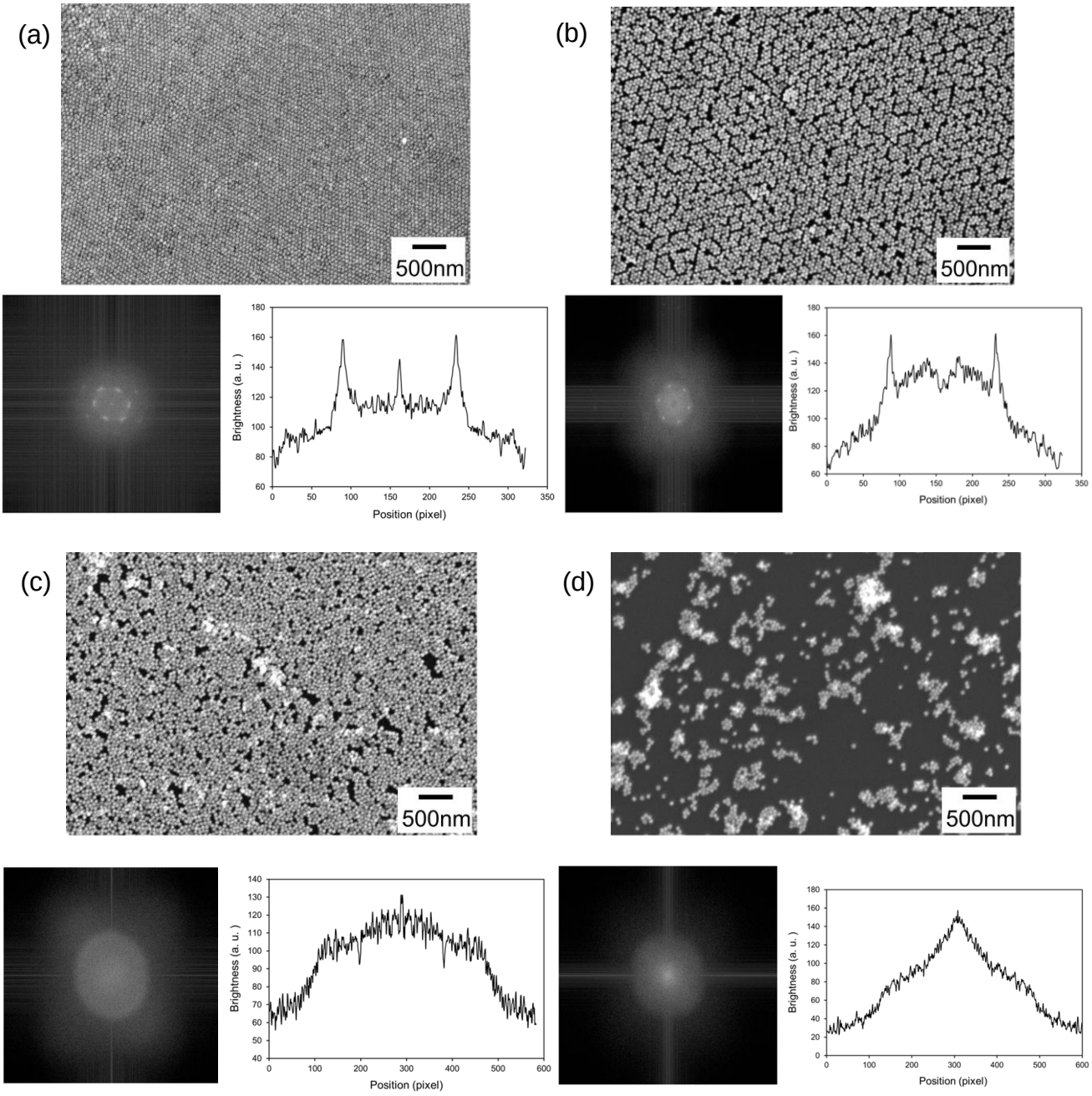

Fig. 7-4. SEM image at × 20000 magnification, their Fourier transform image and their brightness distribution of four substrates composed by AuNPs with diameter of 60nm; (a) SW-substrate 1 (b) SW-substrate 2 (c) OW-substrate (d) DD-substrate

AuNPs.

To evaluate uniformities of these substrates in terms of density and its relative standard deviations (RSD), these SEM images were divided into a division with a size of 500 nm×500 nm, and we counted AuNPs to estimate packing rates at each division. Average packing rates and their RSDs of these substrates were shown in table 7-1. Packing rates of these substrates (SW-substrate 1, SW-substrate 2, OW-substrate and DD-substrate) were 78 %, 73 %, 68 % and 16 %, respectively. And, their RSDs were 3.1 %, 5.5 %, 6.2 % and 70 %. The SW-substrate 1 had highest packing rate and smallest RSD. This result means that SW-substrate 1 and 2 have a higher uniformity than other substrates.

Substrate	Average packing rate	RSD of packing rate
SW substrate1	78%	3.1%
SW substrate 2	73%	5.5%
OW substrate	68%	6.1%
DD substrate	16%	71%

Table 7-1. Average and RSD of packing rates of four substartes

7-3-2 SERS measurement of crystal violet molecules

Mono-layered CV molecules adsorbed on the SW-substrate 1 was measured with a 532 nm excitation and its spectrum in a Raman shift region from 0 cm^{-1} to 3000 cm^{-1} was shown in Fig. 7-5. On the other hand, CV molecules on a flat Si substrate was not detected with same experimental condition, although much larger amount of CV molecules than mono-layered thin film were prepared by dropping 5 μl with a concentration of 10^{-6} M on the substrate. These results show that our substrate has an enough SERS activity. In this spectrum, there are several sharp peaks and a broad peak. It is well-known that the broad peak as large background is often observed in SERS measurement due to the enhancement effect caused by the LSPR. This broad peak is a good evidence of SERS activity, too. These sharp peaks are assigned to various vibration modes as shown in table 7-2. In order to discuss peak intensities of these vibration modes, the background must be removed. The background is mainly consisted of fluorescence of CV molecules. Therefore, this background was removed by subtracting fluorescence spectrum of normal CV molecules from the SERS spectrum, as shown in Fig. 7-6.

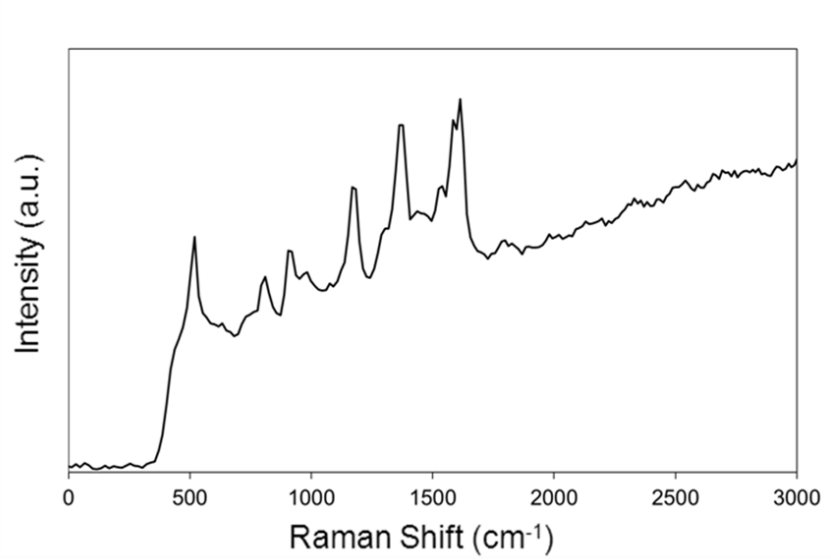

Fig. 7-5. SERS spectrum of mono-layered CV molecules on SW substrate

Observed Raman shifts of crystal violet	
1612 cm^{-1}	Stretching vibration of aromatic ring
1583 cm^{-1}	Stretching vibration of aromatic ring
1363 cm^{-1}	Symmetry deformation of methyl group
1167 cm^{-1}	Degenerate vibration of amine group
920 cm^{-1}	Ring breathing of aromatic ring
(520 cm^{-1})	(Single crystal silicon of supporting substrate)

table 7-2. Observed Raman shifts of crystal violet.

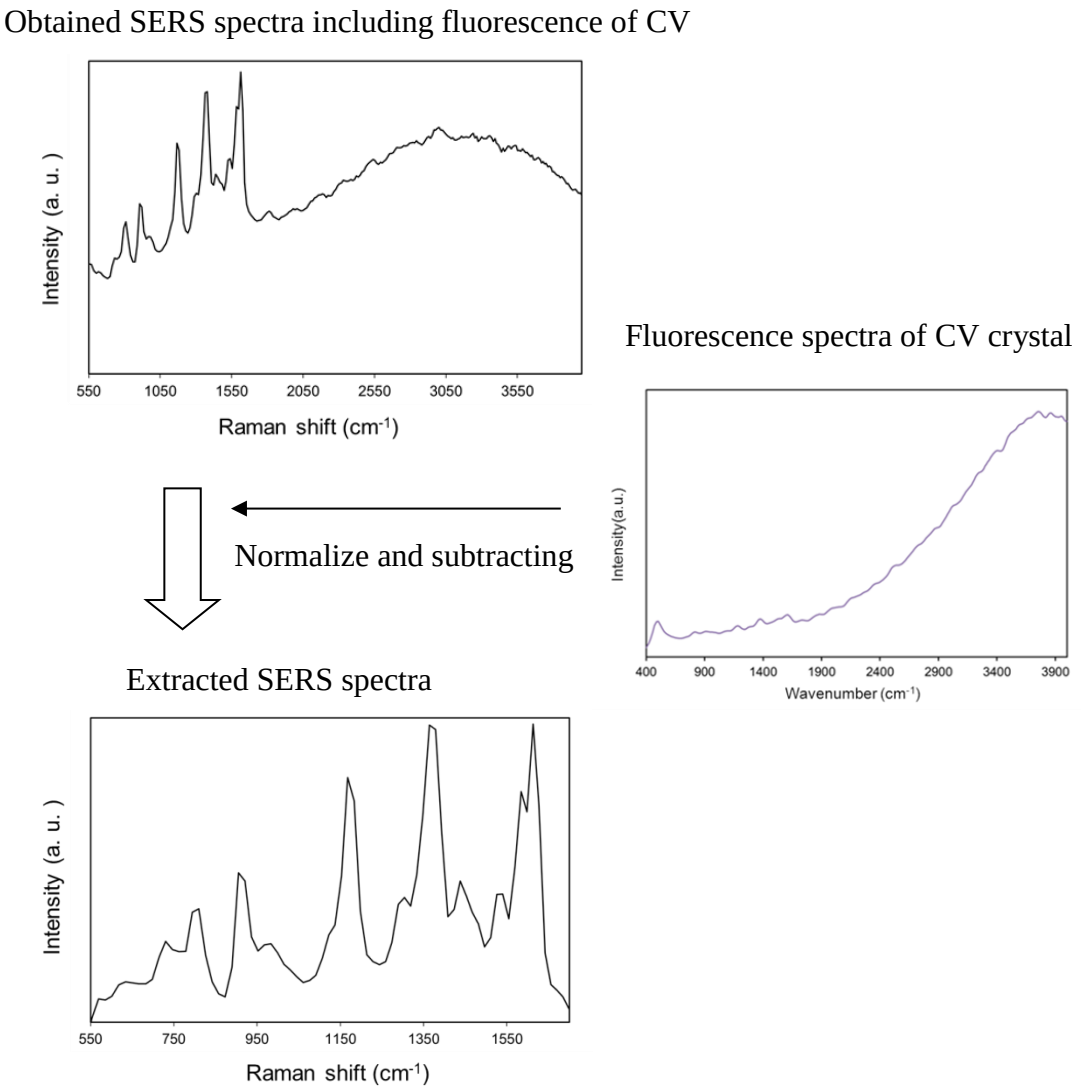

Fig. 7-6. A chart of removal of the fluorescence background of CV

7-3-3 Optimization of the dipping time

CV molecules adsorb to prepared substrates gradually. Therefore, the author must estimate saturation time of adsorption of CV molecules in order to decide amount of adsorbed CV molecules. The author examined dependence at dipping time of the

SERS intensity to estimate saturated adsorption time. OW substrates were employed as SERS active substrates in this experiment because OW substrates can be created easily. CV molecules are known for quasi-chemical adsorption to a surface of gold. In this experiment, SERS spectra of CV were recorded after removing, washing and drying the surface of each substrate in order to optimize dipping time for saturated adsorption, as shown in Fig. 7-7.

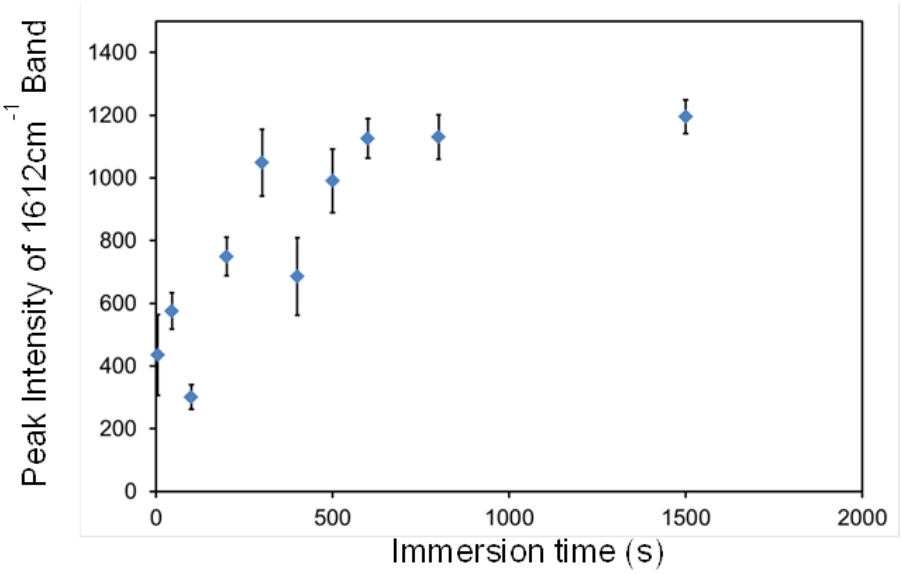

Fig. 7-7. A dependence of a peak intensity of 1612 cm^{-1} band on dipping time

Its vertical axis indicated peak intensities of 1612 cm^{-1} band, and the horizontal axis indicated immersion time. At the time of 600 seconds (10 minutes), the peak intensity was saturated. Therefore, the author estimated that it took 10 minutes to reach the saturated adsorption.

7-3-4 Enhancement factor of the 2DMA substrate

The 2DMA substrate showed remarkably high spot-to-spot reproducibility in a SERS measurement. On the other hand, its sensitivity was still not discussed, although the sensitivity is important for development of sensors. In this experiment, the author estimated the enhancement factor (E_F) of the 2DMA roughly. Generally, an E_F is an approximate indicator of sensitivity of a SERS active substrate. An E_F is given as follow.

$$E_F = \frac{I_{SERS}/N_{SERS}}{I_{Normal}/N_{Normal}}$$

I: intensity of a Raman signal, N: number of molecules which contribute to a Raman signal

The E_F of SW-substrate was evaluated by adsorbing CV molecules on the SW-substrate and detecting their Raman scattering signals using 514.5 nm exciting laser (Ar laser). In saturated adsorption, the amount of adsorbed CV can be estimated. The amount of adsorbed CV was determined by estimating the surface area of the AuNP and the average adsorption area of each sample molecule. The CV molecule has a structure with a carbon in the center and three benzene rings at each apex of a triangle. Therefore,

the CV molecule is roughly regarded as a circle with a diameter of 1 nm. Therefore, 10^{12} to 10^{13} molecules/mm^2 CV molecules are adsorbed on our 2DMAs made of 60 nm AuNPs. The Raman spectrum of the CV on our 2DMAs is compared in Fig. 7-8 with CV molecules on a glass substrate whose density is 10^{17} to 10^{18} molecules/mm^2 measured under the same condition.

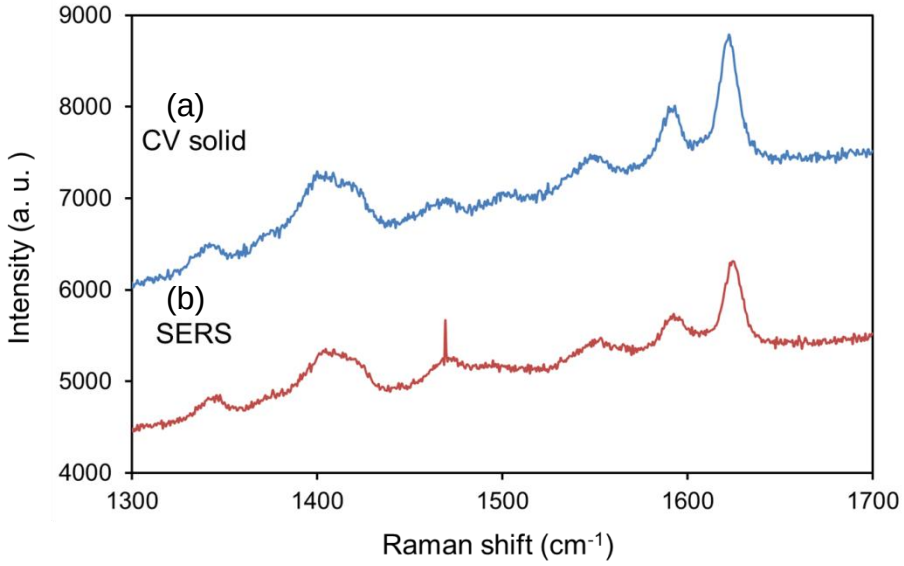

Fig.7-8. Raman spectra of CV; (a) CV solid (b) SW-substrate 1

It is evident that our 2DMA gives the enhancement in the Raman signal by 5 to 6 orders of magnitude. The efficiency is much higher than the surface enhancement effect by rough metal surface, which is typically in the order of 3 to 4. It is considered that this high enhancement effect may be caused by two features of the SW-substrate 1.

One is inter-particle gap with a distance of sub-10 nm between AuNPs because this gap plays as a hot site. The other is absence of aggregations of AuNPs. Moreover, we verified that other prepared substrates also had enough SERS activities although these substrates gave us lower enhancement than the SW-substrate 1.

7-3-5 SERS reproducibility of each substrate

In order to evaluate reproducibility of SERS signals detected on the SW-substrate 1, spot-to-spot SERS signals from these SERS active substrates were measured. In Fig. 7-9, its vertical axis indicated normalized peak intensities of each band of CV, and the horizontal axis indicated packing rates of these substrates. Errors of SERS intensities of each band improved with increase of packing rates of these substrates. However, these degrees of improvement have different. The author considered that these differences were due to adsorption condition of CV on AuNPs. It is known that adsorption condition of analyte molecule has an effect on SERS intensity and Raman shift because charge transfer enhancement is affected by the adsorption. In this thesis, the author focused on electromagnetic enhancement which is dominant.

1167 cm^{-1}
Degenerate of amine group

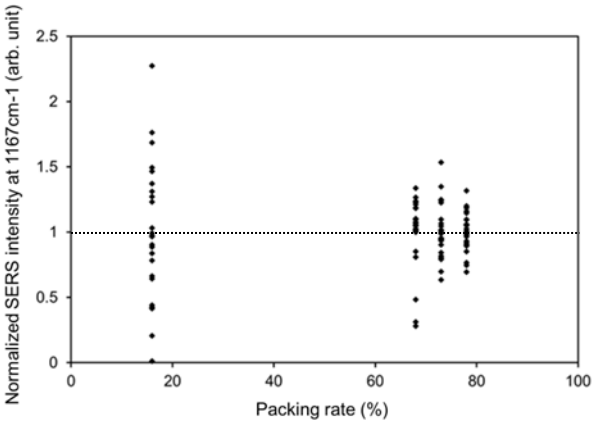

1363 cm^{-1}
Symmetry deformation
of methyl group

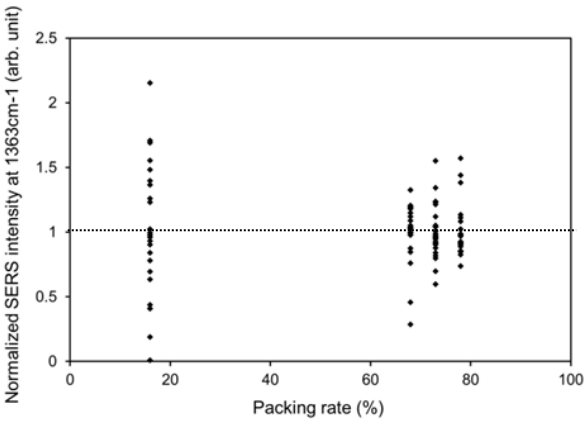

1612 cm^{-1}
Stretching vibration
of aromatic ring

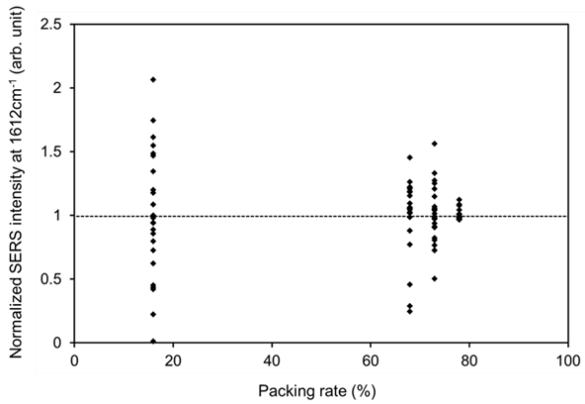

Fig. 7-9. A graph of normalized peaks intensities of bands at 1167 cm^{-1}, 1363 cm^{-1} and 1612 cm^{-1} versus packing rates of four substrates. These peaks intensities were obtained from different 25 spot in these substrates.

The author considered that the band at 1612 cm^{-1} which was attributed to stretching vibration of aromatic rings was not affected by charge transfer enhancement because these aromatic rings were far from adsorbed sites. Therefore, we thought that the intensity of the band at 1612cm^{-1} mainly reflected to the EM enhancement. An error of SERS intensities obtained from the SW-substrate 1 (packing rate: 78 %) showed the smallest value in these experiments. Errors of SERS intensities from the SW-substrate 2 (packing rate: 73 %) and the OW-substrate (packing rate: 68 %) showed medium value in these experiments, and an error of SERS intensities from the DD-substrate (packing rate: 16 %) showed the largest value in these experiments. These results indicated that the SW-substrate 1 gave us a high reproducible detection of SERS signals which were mainly enhanced by the enhanced EM field. Therefore, it is considered that the SW-substrate 1 had more uniform EM fields on its surface than other substrates because 2DMA in the SW-substrate 1 had well-ordered arrangement with a constant inter-particle distance of sub-10 nm. On the other hand, the SW-substrate 2, the OW-substrate and the DD-substrate didn't have uniform EM fields. Moreover, the OW-substrate and the DD-substrate gave us significant lower sensitivities at several measurement points than their average intensities. It is considered that these lower sensitivities are caused by aggregations of AuNPs in these substrates, which decrease

the enhanced EM field, because the OW-substrate and the DD-substrate include many aggregations of AuNPs at random positions.

Next, a graph with RSD of the peak intensities as a vertical axis to compare these variations of each substrate was shown in Fig. 7-10.

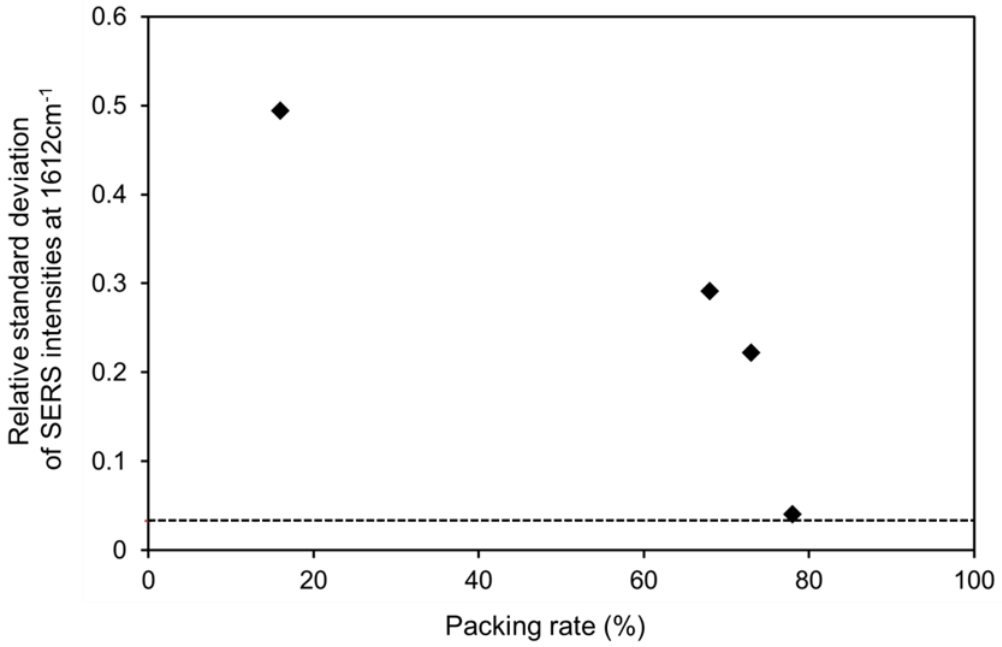

Fig. 7-10. A graph with RSD of the peak intensities versus packing rates of these substrates. Dotted line indicates a systematic error in this experiment obtained from single silicon crystal.

RSD values of peak intensities at 1612 cm^{-1} were decreased with increase of packing rate. It is considered that this improvement of the reproducibility in SERS measurement between the DD-substrate and the OW-substrate is mainly caused by the RSD value of

packing rate because this RSD value becomes one of barometers of uniformity of the nano-structure surface. On the other hand, there were improvement of the reproducibility in SERS measurement between the OW-substrate and the SW-substrate 2, although the difference between not only packing rates but also RSD values of packing rate of these substrates is not so large. The reason is that the OW substrate had an unbalance of density of AuNPs compared with the SW substrate, that is, this improvement relates with existence of aggregations which break the balance.

In order to discuss the balance in detail, we compared two SW-substrates with packing rates of 73 % (SW-substrate 2) and 78 % (SW-substrate 1) for reproducibility of SERS measurement. There were large improvement of reproducibility in SERS measurement between the SW-substrate 1 and the SW-substrate 2, although difference between packing rate of SW-substrate 2 and packing rate of SW-substrate 1 was small. Moreover, difference of those RSD was also small. On the other hand, the SW-substrate 1 had high uniformity and inter-particle gaps of average sub-10 nm, while the SW-substrate 2 consisted of a lot of small structures which consist of several AuNPs. There were differences in arrangement between these SW-substrates. Therefore, the SW-substrate 2 broke its balance compared with the SW substrate 1. From these results, we considered that spot-to-spot reproducibility significantly depended on not only

packing rates and those RSD but also the local uniformity of arrangement in the 2DMA. Surprisingly, RSD of from the SW-substrate 1 was similar to a systematic error of our Raman measurement system shown in Fig. 6-10. The systematic error was obtained by a spot-to-spot Raman measurement of a Si single crystal. This result meant that the SERS measurement with the SW substrate 1 showed very high reproducibility.

6-4 Conclusions

SW-substrates were applied as SERS active substrates, and their analytical performances such as sensitivity and reproducibility were evaluated. We verified that AuNPs in SW-substrate 1 arranged orderly and its 2DMA had a gap with an inter-particle distance of sub 10 nm, although these AuNPs were not decorated by any surface modifiers. Raman measurements revealed that SW substrates gave us an enhancement in Raman signals of CV by 5 to 6 orders of magnitude. Therefore, SW substrates had high SERS enhancement effect. Next in order to evaluate a reproducibility of SERS signals detected on the SW substrate 1, we measured spot-to-spot SERS signals from the SW -substrate 1. The SW substrate 1 enabled a high reproducible detection of SERS signals. It is considered that the SW-substrate 1 had uniform EM fields because 2DMA in the SW-substrate 1 arranged orderly. Possible

future investigations lead to applications of the SERS measurement with this SW substrate to quantitative analysis of ultra-trace analytes.

Appendix

Study of two-dimensional highly-ordering of gold nanoparticles for an optical sensor by using surface plasmon excitation as an assistance effect

Introduction

In chapter 3 and 4, I had described that there are a lot of methods for fabricating 2DMAs. In order to fabricate molecular sensors based on SERS, we paid attention to not only sandwich method but also oil-water trapping method (OW method) because OW method can obtain large 2DMA (cm^2 order) easily. However, the 2DMA fabricated by OW method has not enough uniformity to apply molecular sensors based on SERS. This non-uniformity is caused by a lot of aggregations of metal nanoparticles in the 2DMA. We considered that the aggregations of AuNPs are formed by breaking a balance of inter-particle forces which are mainly composed by van der Waals attraction and electrostatic repulsive when metal nanoparticles are trapped at oil-water interface. On the other hand, Y. Tanaka and co-workers reported that electrostatic repulsive force is enhanced by localized surface plasmon resonance (LSPR) [99]. Therefore, we considered that SP excitation of metal nanoparticles may suppress formations of aggregations of metal nanoparticles, and introduced this phenomenon into the OW

method.

Experimental

Aqueous solution of spherical AuNPs whose diameter was 60nm with narrow size distribution was purchased from BBInternational. The concentrations of the AuNPs aqueous solution were 2.6×10^{10} particles/ml. Crystal violet (CV), which was purchased from Sigma-Aldrich, was used as a sample molecule to examine its SERS activity. Methanol (99 %), acetone (99 %) and toluene (99 %) were purchased from Wako. 2DMAs were constructed onto slide glasses as supporting substrates. These slide glasses were purchased by Matsunami. These supporting substrates were washed in ultrasonic bath along with deionized water for 15 min and then washed with methanol and acetone. In OW method, 5ml of AuNPs aqueous solution was transferred to a vial, and 5 ml of toluene was added to the solution in order to form an interface between toluene and water. After forming the interface, 5 ml of methanol was injected into the vial vigorously, and then AuNPs were trapped at the interface layer. AuNPs trapped at the interface formed a 2DMA. Subsequently, the 2DMA was transferred onto the supporting substrate. No surface modifier agent was used in fabricating these substrates.

In addition, we constructed a system which can irradiate a laser to both layers including the toluene / water interface, as shown in Fig. 1. 532 nm lines of Nd:YAG

laser was employed as an laser source because the wavelength can match the localized surface plasmon (LSPR) of the AuNP. The laser power was controlled by a neutral density filter (maximum laser power 30 mW). Moreover, the system can obtain absorption spectra of 2DMAs trapped at oil / water interface.

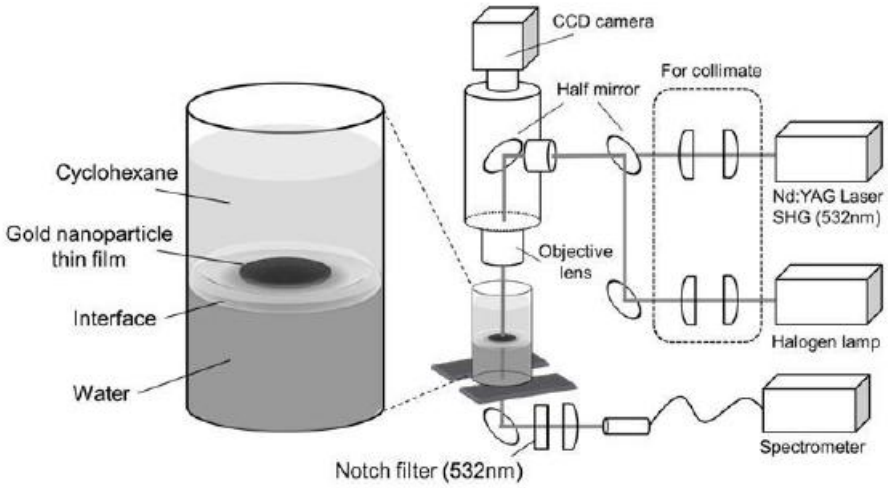

Fig. 1 Experimental system of two-dimensional array fabrication system and spectroscopic system

Morphologies of all prepared 2DMAs were characterized by scanning electron microscopy (SEM; KEYENCE VK-9700) with an acceleration voltage of 20 kV. Raman measurements were carried out by our Raman measurement system. 532 nm lines of Nd:YAG laser was employed as an excitation laser source. The laser power at sample position was about 5mW and its laser focal spot was ca. 10 μm^2. Raman spectra were obtained by a -15 °C air-cooled spectrometer (HAMAMATSU PHOTONIC Inc.) connected to the detector. The spectra were acquired by accumulating five spectra with

10 seconds integration time each. These SERS active substrates were dipped in the 10^{-5} M CV aqueous solution for 15 minutes in order to achieve saturated adsorption of CV molecules. After dipping them in the 10^{-5} M CV aqueous solution, these SERS active substrate were washed by pure water in order to remove impurities and non-adsorbed CV molecules.

Results and Discussion

A SEM image (× 20000) of a substrate fabricated by OW method was shown in Fig. 1 (a). White areas and black areas in Fig. 1(a) corresponded to aggregations and defects in AuNP assembly. On the other hand, a SEM image (× 20000) of a substrate fabricated by OW method with laser irradiation (532 nm, 0.25 mW / mm^2) by our system was shown in Fig. 1 (b).

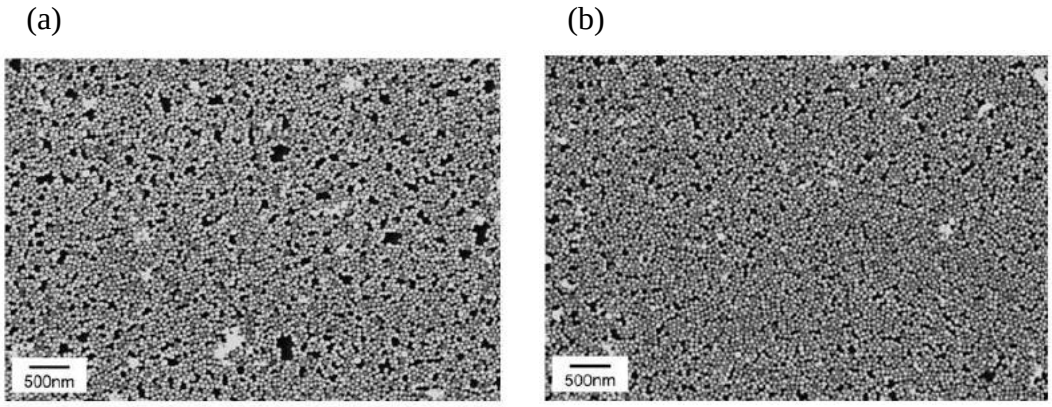

Fig. 2 SEM images of two-dimensional array of AuNP
(a) without laser irradiation (b) with laser irradiation

In Fig. 1 (b), white areas and black areas were decreased compared to these in Fig. 1 (a). Namely, 2DMAs fabricated by OW method with laser irradiation had higher flatness and uniformity than conventional OW method. For estimation of a uniformity of these two 2DMAs, these SEM images were divided into a unit with a size of 500 nm×500 nm, and we counted a number of AuNPs at each unit, as shown in Fig. 2 (a), (b).

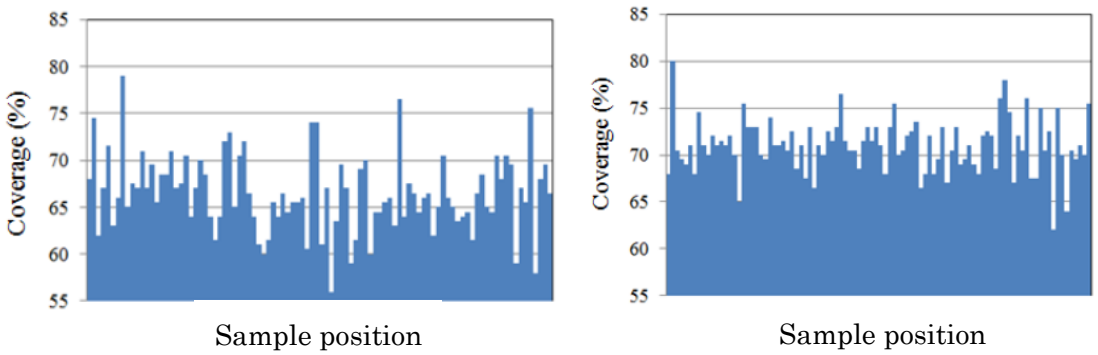

Fig. 3 Coverage (packing rate) of two-dimensional array of AuNP
(a) without laser irradiation (b) with laser irradiation

Average packing rate of the 2DMA fabricated by OW method without laser irradiation and its relative standard deviation (RSD) were 75 % and 7 %, respectively. On the other hand, average packing rate of the 2DMA fabricated by OW method with laser irradiation and its RSD were 80 % and 5 %, respectively. Considering the 2D closest packing rate of 91 %, a difference between these two average packing rates was

significant. In addition, RSD of packing rate of 2DMA fabricated by OW method with laser irradiation was higher than that of 2DMA fabricated by OW method without laser irradiation. Therefore, 2DMA fabricated by OW method with laser irradiation had higher uniformity than without laser irradiation. In Fig. 2 (a), it seems that the 2DMA is composed by small structures which consist of several AuNPs. We considered that the 2DMA had a lot of defects and low uniformity because these small structures had various sizes. On the other hand, in Fig. 2 (b), formation of these small structures was suppressed more or less.

Next we obtained absorption spectra of these two 2DMAs and compared them in order to discuss an aggregation condition of AuNPs. These absorption spectra were shown in Fig. 4.

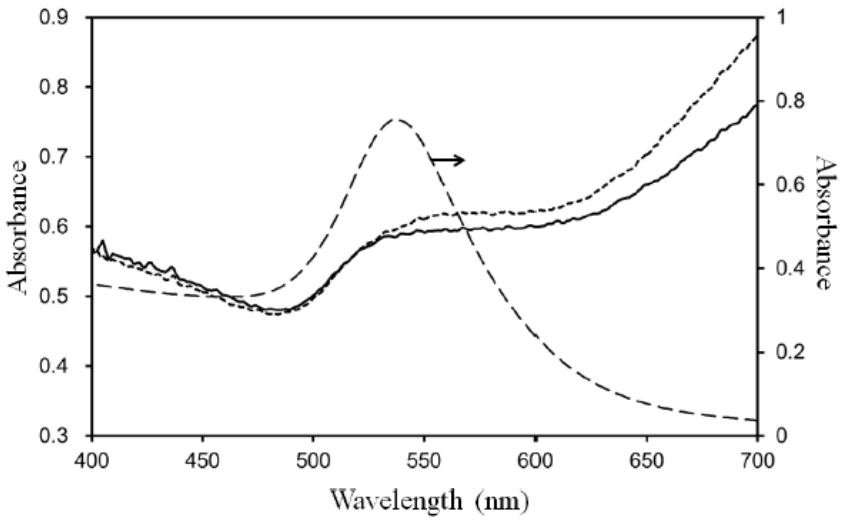

Fig. 4 Absorption spectra of two-dimensional array of AuNP on a glass plate without laser irradiation (dot line) and with laser irradiation (solid line). Dashed line shows absorption spectrum of AuNP aqueous solution (right axis).

Absorption spectrum of 2DMA fabricated by OW method without laser irradiation was red-shifted from absorption spectrum of 2DMA fabricated by OW method without laser irradiation. It is known that an absorption spectrum of isolated AuNPs in water has a single peak at 537 nm, which corresponds to the LSPR of a AuNP. In addition, when AuNPs form aggregations, it is known that the LSPR peak is shifted to long-wavelength region. Therefore, the absorption spectra of 2DMA with laser irradiation indicated that number or sizes of aggregations in 2DMA were decreased. From these result, we predicted that the laser irradiation at 532 nm which excite LSPR enhance inter-particle repulsive force. In order to verify the prediction, 2DMA trapped at oil / water interface was irradiated by laser with higher power (150 mW / mm^2) than previous experiment. Optical microscope images of 2DMA trapped at oil / water interface before and after laser irradiation were shown in Fig. 5 (a), (b).

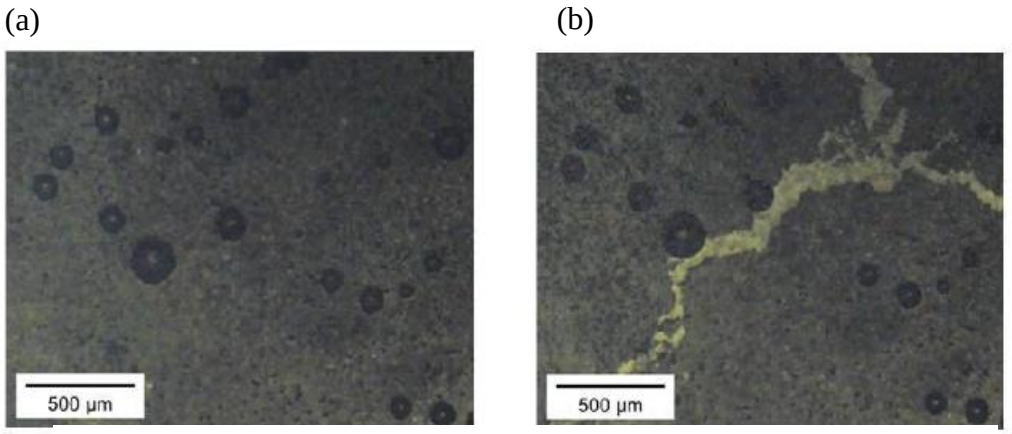

Fig. 5 Optical microscopic images of two-dimensional array of AuNPs
(a) before laser irradiation (b) after laser irradiation

Black area in Fig. 5 was attributed to a 2DMA of AuNPs. In Fig. 5 (a) (before laser irradiation), the 2DMA was observed in whole of the image. On the other hand, large crack was observed in Fig. 5 (b). This cracking behavior worked closely with the laser irradiation. Moreover, we introduced a 632 nm laser line (He-Ne laser) instead of 532nm laser line to the laser irradiation system, and 2DMA trapped at oil / water interface was irradiated by this laser with same laser fluence as first experimental condition. As a result, the crack was not observed. This result suggested that the cracking was not caused by thermal motions of AuNPs. Therefore, in order to observe an aggregation condition of 2DMA trapped at oil / water interface, absorption spectra of 2DMAs at oil / water interface without laser irradiation and with laser irradiation were

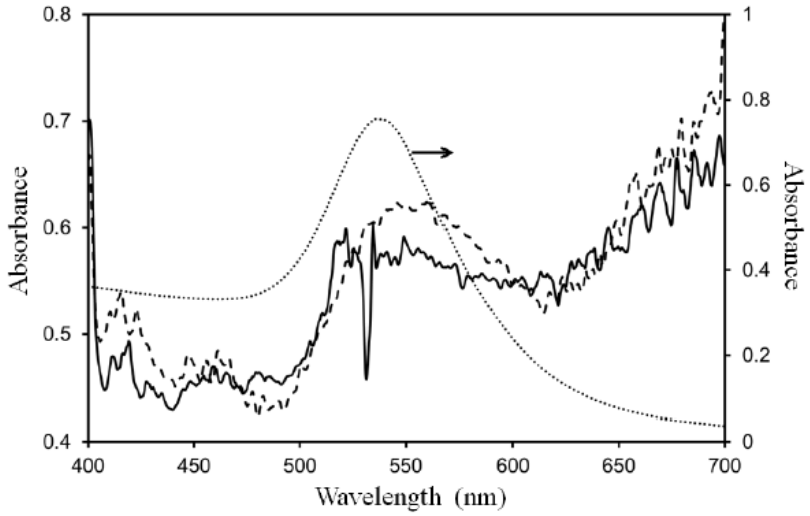

Fig. 6 Absorption spectra of two-dimensional array of AuNP at oil / water interface without laser irradiation (dashed line) and with laser irradiation (solid line). Dot line shows absorption spectrum of AuNP aqueous solution (right axis).

shown in Fig. 6. A depression near 532 nm in absorption spectrum of 2DMA with laser irradiation was due to an optical filter for interruption of irradiation laser. Absorption spectrum of 2DMA without laser irradiation had a broad peak in the wavelength region from 500 nm to 600 nm, and the peak was red-shifted from the LSPR peak of AuNP aqueous solution. This result indicates that the AuNPs contact with neighboring AuNPs in 2DMA. On the other hand, a peak in absorption spectrum of 2DMA with laser irradiation was observed in almost same region as the LSPR peak of AuNP aqueous solution. This result indicates AuNPs are almost present in an isolated state. From these results, we considered that LSPR excitations of AuNPs enhanced repulsive force and the repulsive force induced isolation of AuNPs.

In order to evaluate analytical performances of the 2DMA, we performed a Raman measurement of CV. Raman spectra of CV adsorbed on 2DMAs without laser irradiation and without laser irradiation were shown in Fig. 7.

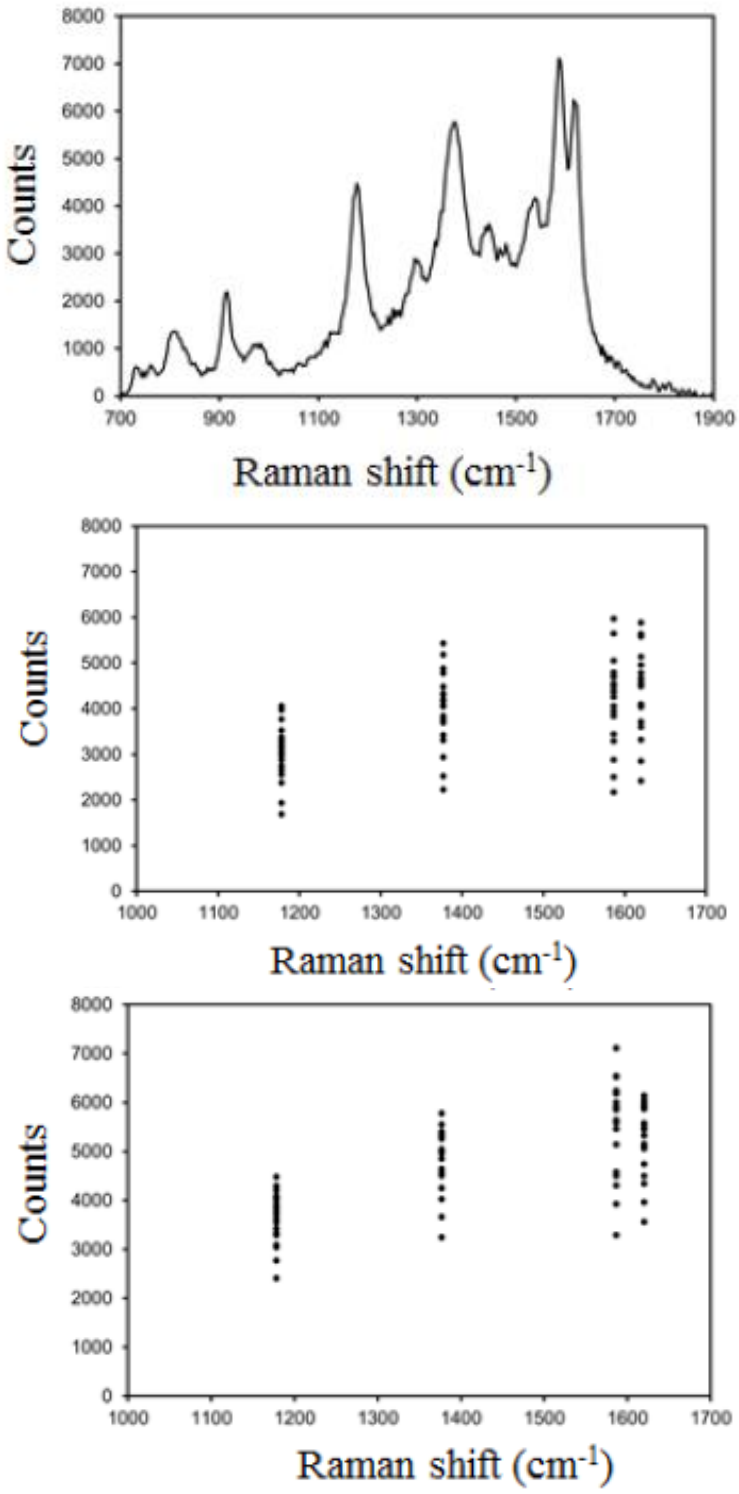

Fig. 7 (a) Raman spectrum of crystal violet on the 2DMA
(b) peak intensities of Raman spectra on the 2DMA without laser irradiation
(c) peak intensities of Raman spectra on the 2DMA with laser irradiation

The laser power at sample position was about 0.2 mW and its laser focal spot was ca. 0.5 μm^2. Both substrates had enough SERS activities. To estimate a spot-to-spot reproducibility of peak intensities based on arrangement of AuNPs, we paid attention to CH stretching vibration band in aromatic ring at 1178 cm^{-1}, phenyl stretching vibration band at 1377 cm^{-1} and CC stretching vibration bands in aromatic ring at 1587 cm^{-1} and 1620 cm^{-1}. The reason why peak intensities of these band were chosen was that these bands were unaffected by charge transfer enhancement very much. Average Raman peak intensities of CV adsorbed on both 2DMA and their RSD were showed in table 1.

	1178cm^{-1}		1377cm^{-1}		1587cm^{-1}		1620cm^{-1}	
	Counts	RSD	Counts	RSD	Counts	RSD	Counts	RSD
Without laser irradiation	3034	20%	4000	21%	4188	21%	4398	21%
With laser irradiation	3638	15%	4801	14%	5540	17%	5280	14%

table 1. Values of average peak intensities and their relative standard deviations of obtained Raman spectra on both two-dimensional arrays of AuNPs.

Average peak intensities on the 2DMA with laser irradiation were higher from 20 % to 30 % than those without laser irradiation. Considering a difference of the surface area between both 2DMAs was several percent, this result indicates that the 2DMA with laser irradiation give us higher SERS enhancement than those without laser irradiation. It is known that a shorter gap distance generates a significantly stronger EM

enhancement field. The gap is called hot site, when two or more particles approach each other with gap of several nanometers. Therefore, it is reasonable that the 2DMA with laser irradiation have high SERS enhancement factor. On the other hand, RSD of peak intensities on the 2DMA with laser irradiation were improved from 20 % to 30 % than those without laser irradiation. It is considered that this improvement of RSD of peak intensities is caused by higher uniformity of 2DMA with laser irradiation than those without laser irradiation. From these result, we succeeded in higher sensitive and higher reproducible Raman measurement by using LSPR of AuNP for enhancement of repulsive force and controlling of aggregation.

Conclusion

We succeeded in fabrication of 2DMA of AuNPs with highly-ordering by using LSPR of AuNP for enhancement of repulsive force and controlling of aggregation through the process of fabrication. From SEM observation and spectroscopic measurement, we evaluated the order of the 2DMA taking account of particle isolation. Moreover, the highly-ordering of the 2DMA gives us higher sensitive and higher reproducible Raman measurement. From these results, it is expected that our fabricated 2DMA of AuNP leads to apply for a molecular sensor.

General Conclusion

In this thesis, two types of optical functional films were fabricated in order to apply to optical molecular sensors with high analytical performance.

The first was titania thin film as a SALDI-MS substrate. Commonly, mass spectrometry combined with soft ionization methods such as matrix assisted LDI-MS (MALDI-MS) and SALDI-MS provide us with molecular-weight of analyte molecule. However, only information of molecular-weight is not enough to identify molecular structures which have many structural isomers such as sugar chains and so on. In order to identify their molecular structures, the author considered that a selective fragmentation in MS measurement is effective because site selective fragmented ions have structural information of analyte molecules. Therefore, the author paid attention to photocatalytic degradations of adsorbate molecules. In this thesis, the author fabricates titania thin films as SALDI-MS substrate and investigates relationship between titania SALDI spectra pattern and photocatalytic effect.

The second was ordered 2D AuNPs arrays as a SERS substrate. Surface enhanced Raman scattering (SERS) is an attractive technique for ultra-trace analysis of analyte owing to its huge enhancement effect caused by surface plasmon (SP) resonance on a metal nanostructured surface. However, it is difficult to control the enhancement

effect because the efficiency of SP resonance strongly depends on a surface morphology of the SERS active substrate. From this reason, conventional SERS measurement lacks in reproducibility and has seldom been applied to practical uses as molecular sensors. Therefore, in order to solve this problem and apply to a molecular sensor, uniform surface morphology of nanostructure is required as a SERS active substrate. To create a uniform surface roughness of a nanostructured surface, a highly-ordered two-dimensional metal nanoparticle array (2DMA) with a constant inter-particle distance has been fabricated by using the same metal nanoparticles because fabricated SERS active substrates are expected to have the same enhancement effect at any position of the substrate. And, in terms of development of molecular sensor, metal nanoparticles in the sensor require a high chemical stability and a high efficiency of SP excitation. Therefore, AuNPs were selected as SP excitation source. On the other hand, more highly-ordered 2DMAs requires elimination of aggregations because aggregations cause not only a random efficiency of SP excitation but also a decrease of enhancement effect. Generally, in order to prevent nanoparticles from aggregation, surface modifier are used because they play a role as a spacer between nanoparticles. However, the surface modifier changes its optical property and generates background signals which interfere with the detection of target molecules. From these reasons, it is expected that

the 2DMA composed by AuNPs without any surface modifier has a large potential for a molecular sensor, but fabrication methods of the 2DMA still have not been proposed.

On the other hand, our group succeeded in fabricating highly-ordered 2DMA without any surface modifier by using the novel technique, which is called sandwich (SW) method. The SW-method is a very simple technique which is only by sandwiching the AuNPs colloidal solution between two flat plates and drying naturally. However, the 2DMA at this stage could not work for SERS analysis. The reason was that an area of the 2DMA was too small (< mm^2) to obtain many SERS spectra from one substrate and to estimate the quantitative performance, although its SERS enhancement is enough large. In this thesis, the fabrication condition of the SW-method has been optimized in order to expand the area of the 2DMA and a fabrication mechanism in the SW-method has been studied. Then the 2DMA has been applied to SERS measurement in order to develop a molecular sensor with a high reproducibility and an ultra-high sensitivity.

Chapter 1 deals with general introduction. Proposed mechanisms of SERS enhancement effect, importance of fabricating SERS active substrates and purpose of this thesis are discussed.

In chapter 2, SALDI-MS measurements of oligosaccharides on the titania substrate were discussed. A lot of fragment ions of oligosaccharides were observed.

These fragment ions had periodical molecular weight which is correspond to oligosaccharide units only by our substrate. It is suggested that the unique fragmentation process on the titania SALDI-MS substrate relates to photocatalytic reaction. Moreover, the unique fragmentation may be are useful to structural analysis of oligosaccharides because the titania SALDI-MS have a selective fragmentation to glycoside bonds.

In chapter 3, fundamentals of localized SP (LSP), calculation of optical properties of AuNPs and inter-particle coupling effect are discussed in order to understand a relationship between LSP excitation and electromagnetic enhancement in SERS. Optimum diameter of AuNP was estimated for the SERS measurement. To be from 60 nm to 100 nm are suitable because they have high efficiencies of SP excitation.

In chapter 4, common fabrication methods of two-dimensional metal nanostructure and the reason why attention was paid to the 2DMA as quantitative SERS active substrates are discussed. And, the theory for interactions between colloids in solution is discussed. As a result, a guideline for fabricating the highly-ordered 2DMA composed by AuNPs without any surface modifier was obtained.

In chapter 4, SW method and characterization of the 2DMA fabricated by SW method using scanning electron microscope are discussed. And, experimental conditions of the SW method were optimized. As a result, the area of the 2DMA composed by

AuNPs without any surface modifier was expanded compared with that at early stage of this method. Moreover, the 2DMA had a higher packing rate compared with those fabricated by conventional methods.

In chapter 5, a uniformity of the 2DMA of the SW-method and a mechanism of arrangement in the SW-method are discussed by using SEM analysis with Fourier Transform analysis, Vis absorption spectroscopy and optical microscope. These analyses showed that the 2DMA had a high uniformity and a hexagonal periodicity with inter-particle distance of 4nm in the arrangement. From these results, it is considered that the 2DMA have a high uniformity and a constant inter-particle distance which has a large potential to generate a giant enhancement effect. Moreover, the assembly mechanism of SW method was investigated by observations of assembly process with an optical microscope. As a result, it was found that the SW method had three important processes;

1. Supplying AuNPs toward the contact line
2. Maintaining dispersive nature just before formation of the 2DMA
3. Smooth movement of the contact line toward inside

In chapter 6, SW-substrates were applied as SERS active substrates, and their

analytical performances such as sensitivity and reproducibility were evaluated. It was verified that AuNPs in SW-substrate arranged orderly and its 2DMA had a gap with an inter-particle distance of sub 10 nm, although these AuNPs were not decorated by any surface modifiers. Raman measurements revealed that SW substrates gave us an enhancement in Raman signals of CV by 5 to 6 orders of magnitude. Therefore, SW substrates had high SERS enhancement effect. Next in order to evaluate a reproducibility of SERS signals detected on the SW substrate, spot-to-spot SERS signals from the SW –substrate were measured. The SW substrate enabled a high reproducible detection of SERS signals. It is considered that the SW-substrate had uniform EM fields because 2DMA in the SW-substrate arranged orderly.

In conclusion, in this work the author developed two types of optical functional thin films, titania nanoparticle thin film as SALDI-MS substrate, two dimensional AuNPs arrays as SERS substrate. Improvements of analytical performance of SALDI-MS and SERS were achieved by using these optical functional thin films. And, this thesis indicates possibility of development of molecular sensor with high analytical performances such as quantitative ability, qualitative ability, label-free analysis, ultra-high sensitivity by using optical functional thin films.

References

1. C. V. Raman, K. S. Krishnan, Nature, 1928, 121, 501

2. M. Fleischmann, P. J. Hendra, A. J. McQuillan, *Chem. Phys. Lett.* 1974, 26, 163

3. D. L. Jeanmaire, R. P. VanDuyne, *J. Electroanal. Chem.* 1977, 84, 1

4. M. G. Albrecht, J. A. Creighton, *J. Am. Chem. Soc.* 1977, 99, 5215

5. P. F. Liao, J. G. Bergman, D. S. Chemla, A. Wokaun, J. Melngailis, A. M. Hawryluk,

N. P. Economou, *Chem. Phys. Lett.* 1981, 82, 355

6. M. Moskovits, *Rev. Mod. Phys.* 1985, 57, 783

7. A. Campion, P. Kambhampati, *Chem. Soc. Rev.* 1998, 27, 241

8. A. Otto, J. Raman. *Spectrosc.* 2005, 36, 497

9. M. Quinten, *Appl. Phys. B.* 2000, 70, 579

10. E. J. Zeman, G. C. Schatz, *J. Phys. Chem.* 1987, 91, 634

11. M. Futamata, Y. Maruyama, M. Ishikawa, *J. Phys. Chem.B. 2004*, 108 (35), 13119

12. K. Faulds, D. Graham, *Appl. Spectrosc*. 2011, 65, 8, 825

13. M. Fan, G. F. S. Andrade, A. G. Brolo, *Anal. Chim. Acta.* 2011, 693, 7

14. K. Faulds, W. E. Smith, D. Graham, *Anal. Chem*. 2004, 76, 412

15. H. Cho, B. R. Baker, S. W. Hogiu, C. V. Pagba, T. A. Laurence, S. M. Lane, L. P.

Lee, J. B. H. Tok, *Nanolett*. 2008, 8, 4386

16. L. Fabris, M. Dantem, G. Braun, S. Lee, N. Reich, M. Moskovits, T. Nguyen, G. J. Bazan, *J. Am. Chem. Soc*. 2007, 129, 6086

17. X. Han, G. Huang, B. Zhao, Y. Ozaki, *Anal. Chem*. 2009, 81, 3329

18. J. Driskell, K. Kawata, R. Lipert, M. Porter, J. Neill, J. Ridpath, *Anal. Chem.* 2005, 77, 6147

19. B. Yakes, R. Lipert, J. Bannantine, M. Porter, *Clinical and Vaccine Immunology.* 2008, 15, 227

20. Y. W. C. Cao, R. C. Jin, C. A. Mirikin, *Science*. 2002, 297, 1536

21. D. K. Lim, K. S. Jeon, H. M. Kim, J. M. Nam, Y. D. Suh, *Nat. Mater*. 2010, 9, 60

22. H. Wang, C. S. Levin, N. J. Halas, *J. Am. Chem. Soc*. 2005, 127, 14992

23. H. W. Ting, Y. Lin, Y. Wu, Li. Chou, C. Tsai, L. Chen, *J. Mater. Chem. C*. 2013, 1, 3593

24. J. B. Jackson, N. J. Halas, *Proc. of the Natl. Acad. Of Sci. of the U. S. A*. 2004, 101, 17930

25. C. Levin, J. Kundu, B. Janesko, G. Scuseria, R. Raphael, N. J. Halas, *J. Phys. Chem. B.* 2008, 112, 14168

26. A. Barhoumi, D. Zhang, F. Tam, N. J. Halas, *J. Am. Chem. Soc.* 2008, 130, 5523

27. F. Wei, D. M. Zhang, N. J. Halas, J. D. J. Hartgerink, *J. Phys. Chem. B*. 2008, 112, 9158

28. X. Y. Zhang, M. A. Young, O. Lyandres, R. P. VanDuyne, *J. Am. Chem. Soc*. 2005, 127, 4484

29. K. C. Bantz, C. L. Haynes, *Vib. Spectrosc*. 2009, 50, 29

30. L. A. Dick, A. D. McFarland, C. L. Haynes, R. P. VanDuyne, *J. Phys. Chem. B*. 2002, 106, 853

31. J. Stropp, G. Trachta, G. Brehm, S. Schneider, *J. Raman. Spectrosc*. 2003, 34, 26

32. L. Gunnarsson, E. J. Bjerneld, H. Xu, S. Petronis, B. Kasemo, M. Kall, *Appl. Phys. Lett*. 2001, 78, 802

33. H. Im, K. C. Bantz, N. C. Lindquist, C. L. Haynes, S. H. Oh, *Nano Lett*. 2010, 10, 2231

34. A. Tao, F. Kim, C. Hess, J. Goldgerger, R. R. He, Y. G. Sun, Y. N. Xia, P. D. Yang, *Nano Lett*. 2003, 3, 1229

35. J. L. Yao, J. Tang, D. Y. Wu, D. M. Sum, K. H. Xue, B. Renm B. W. Mao, Z. Q. Tian, *Surface Science*, 2002, 514, 108

36. Q. M. Yu, P. Guan, D. Qin, G. Golden, P. M. Wallace, *Nano Lett*. 2008, 8, 1923

37. T. H. Reilly, S. H. Chang, J. D. Corbman, G. C. Schatz, K. L. Rowlen, *J. Phys. Chem. C*. 2007, 111, 1689

38. P. E. Batson, *Ultramicroscopy*, 1982, 9, 3, 277

39. A. I. Dragan, C. D. Geddes, J. Appl. Phys. 2010, 108, 9, 094701

40. G. H. Chan, J. Zhao, E. M. Hicks, G. C. Schatz, R. P. VanDuyne, Nano Lett. 2007, 7, 7, 1947

41. P. C. Wu, C. G. Khoury, T. Kim, Y. Yang, M. Losurdo, G. V. Bianco, T. Vo-Dinh, A. S. Brown, H. O. Everitt, *J. Am. Chem. Soc*. 2009, 131 (34), 12032

42. D. Sarid, W. Challener, *Modern introduction to surface plasmons*; Cambridge univ. press, 2010

43. K. Tanaka, H. Waki, Y. Ido, S. Akita, Y. Yoshida, T. Yoshida, *Rapid Commun. Mass Spectrom*. 1988, 2, 151

44. M. Karas, F. Hillenkamp, *Anal. Chem*. 1988, 60, 2299

45. J. Wei, J. M. Buriak, G. Siuzdak, *Nature*. 1999, Vol. 399

46. H. Kawasaki, T. Akira, T. Watanabe, K. Nozaki, T. Yonezawa, R. Arakawa, *Anal Bioanal Chem*. 2009, Vol. 395, 5, 1423

47. H. Sato, T. Seino, A. Yamamoto, M. Torimura, H. Tao, *Chem. Lett*. 2005, 34, 1178

48. K. Shibamoto, K. Sakata, K. Nagoshi, T. Korenaga, *J.Phys. Chem.C*. 2009, 113, 17774

49. T. Ohno, K. Sarukawa, K. Tokieda, M. Matsumura, *J. Catal.* 2001, 203, 82-86

50. M. I. Litter, *Applied Catalysis B: Environmetal*, 1999, 23, 89

51. G. Mie, Physik. Z. 1908, 8, 769

52. G. Mie, Greifswald. Ber, physic. Ges. 1908, 5, 492-500

53. X. Zhang, C. R. Yonzon, R. P. VanDuyne, *J. Mater. Res.* 2006, 21, 1083

54. K. A. Willets, R. P. VanDuyne, *Annal Review of Physical Chemistry*. 2007, 58, 267

55. D. Pines, D. Bohm, *Phys. Rev*. 1952, 85, 2

56. P. K. Jain, K. S. Lee, I. H. El-Sayed, M. A. El-Sayed, J. Phys. Chem. B. 2006, 110, 7238

57. P. K. Jain, M. A. El-Sayed, J. Phys. Chem. C. 2007, 111, 17451

58. P. B. Johnson, R. W. Christy, *Phys. Rev. B*, 1970, 6, 4370

59. I. Thormahlen, J. Staub, U. Grigull, *J. Phys. Chem. Ref. Date*, 1985, 14, 933

60. M. Meier, A. Wokaun, *Opt. Lett*. 1983, 8, 581

61. P. N. Njoki, I. S. Lim, D. Mott, H. Y. Park, B. Khan, S. Mishra, R. Sujakumar, J. Luo, C. J. Zhong. *J. Phys. Chem. C*. 2007, 111, 14664-14669

62. M. K. Hossain, K. Shibamoto, K. Ishioka, M. Kitajima, T. Mitani, S. Nakashima,

Journal of Luminescence, 2007, 122, 792

63. W. Rechberger, A. Hohenau, A. Leitner, J. R. Krenn, B. Lamprecht, F. R. Auseenegg, *Opt. Commun*. 2003, 220, 137

64. K. H. Su, Q. H. Wei, X. Zhang, J. J. Mock, D. R. Smith and S. Schultz. Nano lett. 3. (2003) 1087

65. T. Okamoto, K. Kajikawa, *plasmonics*, Kodansya scientific 2010

66. M. Hentschel, M. Saliba, R. Vogelgesang, H. Giessen, A. P. Alivisatos, N. Liu, Nano lett. 2010, 10, 2723

67. R. D. Deegan, O. Bakajin, T. F. Dupont, G. Huber, S. R. Nagel, T. A. Witten, *Nature*, 1997, 389, 827

68. N. D. Denkov, O. D. Velev, P. A. Kralchevsky, I. B. Ivanov, H. Yoshimura, K. Nagayama, Langmuir, 1992, 8, 3183

69. C. D. Dushkin, H. Yoshimura, K. Nagayama, *Chem. Phys. Lett*. 1993, 204, 455

70. B. Kim, S. L. Tripp, A. Wei, *J. Am. Chem. Soc*. 2001, 123, 7955

71. A. Wei, B. Kim, B. Sadtler, S. T. Tripp, *Chem. Phys. Chem*. 2001, 2, 12, 743

72. S. K. Eah, *J. Mater. Chem*. 2011, 21, 16866

73. Y. L. Gang, L. Liu, L. P. Lee, *Nano Lett*. 2005,5, 5

74. H. Wang, C. S. Levin, N. J. Halas, *J. Am. Chem. Soc*, 2005, 127, 14992

75. M. Suzuki, Y. Niidome, N. Terasaki, K. Inoue, Y. Kuwahara, S. Yamada, *Jpn. J. Appl. Phys*. 2004, 43, 4B, 554-556

76. Y. Park, S. Yoo, S. Park, Langmuir, 2007, 23, 21

77. T. Vo-Dinh, *Trac-Trends in Anal. Chem*. 1998, 17, 557

78. M. T. Marshall, M. L. Mcdonald, X. Tong, M. Yeadon, J. M. Gibson, *Rev. Sci. Instrum*. 1998, 69, 440

79. W. Rechberger, A. Hohenau, A. Leiner, J. R. Krenn, B. Lamprecht, F. R. Aussenegg, *Opt. Commun*. 2003, 220, 137

80. K. Ueno, V. Mizeikis, S. Juodkazis, K. Sasaki, H. Misawa, *Opt. Lett*. 2005, 30, 2158

81. A. G. Brolo, E. Arctander, R. Gordon, B. Leathem, K. L. Kavanagh, *Nano Lett*. 2004, 4, 2015

82. J. R. Anema, A. G. Brolo, P. Marthandam, R. J. Gordon, *J. Phys. Chem. C*. 2008, 112, 17051

83. J. C. Hulteen, R. P. Van Duyne, *J. Vac. Sci. Technol. A.* 1995, 13, 1553

84. C. L. Haynes, R. P. Van Duyne, *J. Phys. Chem. B*. 2001, 105, 5599

85. A. J. Haes, C. L. Haynes, A. D. McFarland, G. C. Schatz, R. P. Van Duyne, S. Zou, *MRS. BULLETIN*. 2005, 30

86. E. J. W. Verwey, J. TH. G. Overbeek, *Theory of the Stability of Lyophobic colloids*; Dover: Mineola, New York, 2000.

87. T. Wang, D. Zhang, W. Xu, S. Li, D. Zhu, *Langmuir,* 2002, 18, 8655

88. J. A. Israelachvili, *Intermolecular and Surface Force*, 2nd Ed. Amsterdam: Academic Press; 1991. 246

89. K. Lee, A. N. Sathyagal, A. V. Mc Cormick, *Colloids Surf*. 1998, 144, 115

90. T. G. Lee, K. Kim, M. S. Kim, *J. Raman Spectrosc*. 1991, 22, 339

91. H. Kwok, *Electronic Materials*; PWS publishing Co. New York, 1997

92. M. K. Chow, C. F. Zukoski, *J. Colloid Interface Sci*. 1994, 165, 97

93. T. Kim, K. Lee, M. Gong, S. W. Joo, *Langmuir*, 2005, 21, 9524

94. P. A. Kralchevsky, K. Nagayama, *Langmuir*, 1994, 10, 23

95. E. Adachi, K. Nagayama, *Langmuir*, 1996, 12, 1836

96. K. Shibamoto, M. Kitajima , M. K. Hossain, K. Ishioka, *Japan Patent*. 2012, Jan. 13, 4900550

97. T. J. Norman Jr, C. D. Grant, D. Magana, J. Z. Zhang, J. Liu, D. Cao, F. Bridges, A. Van Buuren, *J. Phys. Chem. B*, 2002, 106, 7005

98. J. R. Lombardi, R. L. Birke, *J. Phys. Chem. C*, 2008, 112, 5605

99. Y. Tanaka, H. Yoshikawa, T. Itoh, M. Ishikawa, *Optics Express*, 2009, 17, 18760

List of Publications

1. “Suppression of matrix-related ions using cyclodextrin in MALDI mass spectrometry”, *Analytical Sciences*, 24 (11), 1497, **2008**, S. Yamaguchi, T. Fujita, T. Fujino, T. Korenaga

2. “MALDI mass spectrometry using 2, 4, 6-trihydroxyacetophenone with cyclodextrins: Suppression of matrix-related ions in low-molecular-weight region”, *Analytical Sciences*, 26 (7), 743, **2010**, T. Fujita, T. Fujino, K. Hirabayashi, T. Korenaga

3. “Settlement of the sweet-spot problem of MALDI crystals using cyclodextrin-supported matrix”, *Chemistry Letters*, 42 (4), 350, **2013**, T. Fujita, T. Fujino

4. “Titania surface assisted laser desorption/ionization mass spectrometry of oligosaccharides”, *Chemistry Letters*, 42 (8), 852, **2013**, T. Fujita, K. Shibamoto

5. “Study of two-dimensional highly-ordering of gold nanoparticles for an optical sensor by using surface plasmon excitation as an assistance effect”, *Bunseki Kagaku*, accepted, K. Shibamoto, Y. Yasumuro, K. Horiuchi, T. Teraoka, T. Fujita

6. “Two dimensional close-packed array of bare gold nanoparticles with inter-particle gap”, *Materials Letters*, under review, T. Fujita, K. Shibamoto

7. “High reproducible surface-enhanced Raman scattering detection with highly-ordered gold nanoparticle array”, *Chemical Physics Letters*, submitted, T. Fujita, K. Shibamoto

Acknowledgments

Many people contributed to the completion of this thesis. I would like to thank my supervisor, Prof. Dr. Mitsuru Ebihara. He gives me warm encouragement and great help. I would like to thank Prof. Dr. Masatake Haruta, Prof. Dr. Tadashi Kato and Prof. Dr. Kouichi Kikuchi of Tokyo Metropolitan University for discussion of various aspects of this study.

My deepest appreciation goes to Assistant Prof. Dr. Kohei Shibamoto. He encouraged me to not only glow as an experimentalist but also as an independent thinker. Without his guidance and persistent help this thesis would not have been possible.

I would also like to thank Associate Prof. Dr. Yasuji Oura and Assistant Prof. Naoki Shirai. I have had their support and encouragement.

Finally I would like to thank to my parents, two elder brothers. They were always supporting me and encouraging me with their best wishes.